Study of Gas Turbine Ingress using Computational Fluid Dynamics

Wang, Le

Award date:
2013

Awarding institution:
University of Bath

Study of Gas Turbine Ingress using Computational Fluid Dynamics

Le Wang

A thesis submitted for the degree of Doctor of Philosophy

University of Bath

Department of Mechanical Engineering

May 2013

Abstract

The ingestion of hot mainstream gas into the wheel-space between the rotor and stator discs is one of the most important internal cooling problems for gas turbine designers. To solve this problem, engineers design a rim seal at the periphery of wheel-space and direct a sealing flow from the internal cooling system to prevent ingress. The main aim of this thesis is to build a simple computational model to predict the sealing effectiveness of externally-induced ingress for engine designers. The axisymmetric model represents a gas turbine wheel-space and provides useful information related to the fluid dynamics and heat transfer in the wheel-space. At the same time, this model saves much computation time and cost for engine designers who currently use complex and time-consuming 3D models.

The computational model in this thesis is called the prescribed ingestion model. Steady simulations are carried out using the commercial CFD code, ANSYS CFX with meshes built using ICEM CFD. Boundary conditions are applied at the ingress inlet of the model using experimental measurements and a mass-based averaging procedure. Computational parameters such as rotational Reynolds number, non-dimensional sealing flow rate and thermal conditions on the rotor are selected to investigate the fluid dynamics and heat transfer at typical experimental rig operating conditions. Different rim seal geometries are investigated and results are compared with experimental data.

In addition to the prescribed ingestion model, two typical axisymmetric rotor-stator system models without ingress are established. The aim of these rotor-stator models is to investigate the fluid dynamics and heat transfer of the wheel-space in the situation without ingress. The effects of geometry and turbulence model also are studied in these simulations. Most results from these simulations are in good agreement with experimental data from the literature, which enhances confidence in the prescribed ingestion model.

For the prescribed ingestion model, the axial-clearance seal (the simplest rim-seal geometry) is first simulated for externally-induced ingress. The sealing effectiveness (on both the stator and rotor), fluid dynamics (in terms of swirl ratio and velocity profiles) and heat transfer (in terms of Nusselt number) are investigated and are shown to be in reasonable agreement with the experimental results from a rig at the University of Bath. In these computations, the mass-weighted average boundary condition is tested with the momentum-weighted average boundary conditions. Different layouts of ingress inlet and egress outlet are also tested and the optimal one is applied to other seal geometries. For heat transfer simulations, different thermal wall boundary conditions are investigated to understand the effect of these conditions on the distribution of Nusselt number on the rotor.

In addition to the axial-clearance seal, three other seals are presented in this thesis: a radial-clearance seal, a double axial-clearance seal, and a radial-axial-clearance combination seal. In accordance with the axial-clearance seal, the sealing effectiveness and fluid dynamics in the wheel-space are investigated for these seals and compared with experimental data. The performance of these four seal geometries is ranked.

It is suggested that the prescribed ingestion model is a compact, relatively straight-forward tool for engine designers. It allows the designer insight into the fluid dynamics and heat transfer of rim seals, and supports the experimental data collected at the University of Bath.

Acknowledgements

I would like to thank my supervisors, Prof. G.D. Lock and Dr. M. Wilson, for their continued suggestion and guidance. Prof. J.M. Owen is also thanked for his advice. Dr. C.M. Sangan and Dr. O.J. Pountney are acknowledged for their eagerness to offer experimental results. Finally, Dr. K. Zhou is thanked for his assistance at the preliminary stage of my study.

Contents

Abstract 1
Acknowledgements 3
Contents 4
List of Figures 6
List of Tables 12
Nomenclature 13
1. Introduction 16
    1.1. A brief history of the jet engine 16
    1.2. Gas turbine 18
    1.3. Internal cooling 20
    1.4. Ingress 22
    1.5. Thesis aim and objectives 23
    1.6. Thesis overview 24
    1.7. Publications 25
2. Literature review 26
    2.1. Rotor-stator systems 26
    2.2. Ingress 34
    2.3. Previous research at University of Bath 46
    2.4. Chapter summary 49
3. Computational method and 3D Computations 50
    3.1. Turbulence model 50
    3.2. Heat transfer 53
    3.3. Other computational settings and parameters 55
    3.4. 3D Computations for the ‘thin seal’ model 56
    3.5. Chapter summary 61
4. Axisymmetric rotor-stator models 62

4.1. Fluid dynamics for the axisymmetric rotor-stator model 63
4.2. Heat transfer for the axisymmetric rotor-stator model 69
4.3. Chapter summary..... 78
5. Prescribed ingestion model: Axial-clearance seal..... 79
5.1. Mass-weighted average assumption for ingestion..... 80
5.2. The effect of layout of ingress inlet and egress outlet..... 87
5.3. Fluid dynamics in the wheel-space..... 91
5.4. Distribution of sealing effectiveness in the wheel-space..... 96
5.5. Heat transfer in the wheel-space.....100
5.6. Chapter summary.....105
6. Prescribed ingestion model: other seal geometries 106
6.1. Radial-clearance seal 108
6.2. Double axial-clearance seal.....115
6.3. Radial-axial-clearance seal.....123
6.4. Sealing performance of all rim seal geometries 127
6.5. Chapter summary.....128
7. Conclusions and future work 129
7.1. The axisymmetric rotor-stator models.....129
7.2. The prescribed ingestion models.....130
7.3. Future work.....132
References.....133
Appendix.....139

List of Figures

Figure 1-1 A simple model of Hero's engine [1]..... 16

Figure 1-2 Ohain's hydrogen-fuelled turbojet engine [3]..... 17

Figure 1-3 Frank Whittle's patent [1]..... 17

Figure 1-4 Simple gas turbine system [4]..... 18

Figure 1-5 Variation of pressure, temperature and velocity in a turbojet [2]..... 19

Figure 1-6 Internal cooling system, including cooling paths [2] 20

Figure 1-7 Film cooling for turbine blades [2]..... 21

Figure 1-8 Generic rotor-stator turbine stage and double clearance-seal inset [6-7] 22

Figure 2-1 Generic rotor-stator configuration [8] 26

Figure 2-2 Batchelor-type flow in a rotor-stator system [9] 27

Figure 2-3 Flow regimes for a closed rotor-stator system [11]..... 28

Figure 2-4 Radial and tangential velocity profiles in a rotor-stator wheel-space [8] 29

Figure 2-5 Measured and computed Nusselt numbers, $\mathrm{Re}_\phi = 1.25\times10^6$ [8].... 29

Figure 2-6 Computational (right) and experimental (left) Nusselt number contours, $\mathrm{Re}_\phi = 0.8\times10^6$ [17]..... 31

Figure 2-7 Computed streamlines superimposed onto experimental heat transfer results, $\mathrm{Re}_\phi = 0.8\times10^6$, $\lambda_\mathrm{T} = 0.38$ [17]..... 31

Figure 2-8 Effect of stator heat transfer on the distribution of $Nu\,\mathrm{Re}_\phi^{-0.8}$ [19].. 33

Figure 2-9 Variation of $C_{w,\min}$ with Re_w [25-27]..... 36

Figure 2-10 Variation of $C_{w,\min}$ with $2\pi G_c P_{\max}^{1/2}$ [25-27]..... 36

Figure 2-11 Variations of $C_{w,\min}$ with $C_{p,\max}$ [30]..... 37

Figure 2-12 Instantaneous velocity contours in the disk cavity [32] 39
Figure 2-13 CFD velocity vectors in axial-radial plane of seal region [32] 40
Figure 2-14 Comparison of local sealing effectiveness at the stator [33] 41
Figure 2-15 Ingestion Mixing Efficiency [37] 43
Figure 2-16 Steady state and time-averaged unsteady buffer cavity effectiveness [44] 45
Figure 2-17 Velocity vectors in the gap [45] 45
Figure 2-18 Orifice ring [49-52] 47
Figure 2-19 Comparison between theoretical effectiveness curves and experimental data for axial-clearance seal with EI ingress (the solid lines are theoretical curves) [51] 48
Figure 3-1 (a) Schematic diagram of 3D thin-seal model (b) Computational mesh [49] 57
Figure 3-2 Computed circumferential distributions of C_p 59
Figure 3-3 Streamlines with effectiveness in the $r-\theta$ plane at $z/s=0.5$ 60
Figure 3-4 Variation of computed effectiveness with Φ_o 61
Figure 4-1 The Bath Rig Model 62
Figure 4-2 The Chen Rig Model 63
Figure 4-3 Computed velocity profiles from Chen and Bath Rig Model compared with measured data, $\lambda_T=0.081$ 65
Figure 4-4 Computed and measured velocity profiles for the Bath Rig Model, $\lambda_T=0.081$ 67
Figure 4-5 Computed velocity profiles with different λ_T for the Bath Rig Model 68
Figure 4-6 The streamlines in whole cavity for two high sealing flow rate cases 69
Figure 4-7 Comparison between definitions for Nu, $\lambda_T=0.081$ 70
Figure 4-8 The swirl ratio at middle plane between the rotor and the stator,

$\lambda_T = 0.081$ 71

Figure 4-9 Radial distribution of $Nu\,\mathrm{Re}_\phi^{-0.8}$ for different λ_T 72

Figure 4-10 Radial distribution of temperature on the rotor surface for the Bath Rig Model..... 73

Figure 4-11 The effect of thermal condition at rotor surface on the radial distribution of $Nu\,\mathrm{Re}_\phi^{-0.8}$ 74

Figure 4-12 Radial distribution of temperature on the rotor surface for the Chen Rig Model..... 75

Figure 4-13 The effect of geometry on the radial distribution of $Nu\,\mathrm{Re}_\phi^{-0.8}$ 76

Figure 4-14 The effect of turbulence model on the radial distribution of $Nu\,\mathrm{Re}_\phi^{-0.8}$ 77

Figure 5-1 (a) The experimental rig in University of Bath [51] (b) The prescribed ingestion model with axial-clearance seal and mesh grid..... 80

Figure 5-2 Experimental data for axial-clearance seal with EI ingress [51]..... 81

Figure 5-3 Swirl ratio distribution for axial-clearance seal with Mass-weighted and Momentum-weighted average assumptions, z/s =0.25 (symbols denote the experimental data [60]) 83

Figure 5-4 Secondary flow streamlines for Momentum-weighted and Mass-weighted average at $\lambda_T = 0.114$ 84

Figure 5-5 The effect of β_o on swirl ratio distribution, z/s =0.25 (symbols denote the experimental data [60]) 86

Figure 5-6 Different layouts of ingress inlet and egress outlet 87

Figure 5-7 The effect of layout on swirl ratio distribution, z/s =0.25 (closed symbols denote the experimental data [60] and open symbols denote the experimental data [8]) 89

Figure 5-8 The swirl contours for three layouts at $\lambda_T = 0.242$ 90

Figure 5-9 Comparison of swirl distributions for the prescribed ingestion model

and the Bath rig rotor-stator model with no ingestion, z/s =0.25 91
Figure 5-10 Comparison of swirl ratio for the prescribed ingestion model and Chen *et al.* [8] at r/b =0.7 92
Figure 5-11 Comparison of swirl distribution for different rotational speed for the prescribed ingestion model at similar λ_T 93
Figure 5-12 Secondary flow streamlines and swirl contours for the prescribed ingestion model with axial-clearance seal..... 93
Figure 5-13 Velocity distributions for the prescribed ingestion model with axial-clearance seal 95
Figure 5-14 Computed variation of effectiveness with $C_{w,o}$ for axial-clearance seal 96
Figure 5-15 The computed variation of effectiveness with Φ_o for axial-clearance seal compared with experimental data [51] 97
Figure 5-16 Radial distribution of effectiveness on the stator for the axial-clearance seal compared with experimental data [60] 98
Figure 5-17 Radial distribution of effectiveness on the rotor for the axial-clearance seal compared with experimental data [61] 99
Figure 5-18 Comparison of radial distribution of ε_c and ε_{ad} on the rotor (symbols denote the experimental data [61]) 100
Figure 5-19 The computed T_{ad} compared with experimental data [61].....102
Figure 5-20 The radial variation of $Nu\,\mathrm{Re}_\phi^{-0.8}$ compared with experimental data [55].....102
Figure 5-21 The radial variation of non-dimensional core temperature compared with experimental data [55].....103
Figure 5-22 The computed radial variation of $Nu\,\mathrm{Re}_\phi^{-0.8}$ including stator heat transfer 104
Figure 6-1 The experimental rigs [60] and computational models for (a)

Radial-clearance seal (b) Double axial-clearance seal (c) Radial-axial-clearance seal.....107
Figure 6-2 Experimental data for radial-clearance seal with EI ingress [54] 108
Figure 6-3 Swirl ratio distribution for radial-clearance seal, z/s =0.25 (symbols denote the experimental data [60]) 109
Figure 6-4 Swirl ratio distribution for radial-clearance and axial-clearance seal, z/s =0.25 110
Figure 6-5 Comparison of swirl distribution for different rotational speed for the radial-clearance seal at similar λ_T 111
Figure 6-6 The computed variation of effectiveness with Φ_o for radial-clearance seal compare with axial-clearance seal (open symbols denote the experimental data [54]) 112
Figure 6-7 The computed streamlines for both seal geometries, $\lambda_T = 0.073$ 113
Figure 6-8 The radial distribution of effectiveness on the stator for the radial-clearance and axial-clearance seals (symbols denote the experimental data [60]) 113
Figure 6-9 The radial distribution of effectiveness on the rotor surface for the radial-clearance and axial-clearance seals.....114
Figure 6-10 (a) Typical high-pressure gas turbine stage of a Rolls-Royce jet engine; (b) detail of rim seal [6] 115
Figure 6-11 Experimental data for double axial-clearance seal with EI ingress [54] 116
Figure 6-12 Swirl ratio distribution for double axial-clearance seal, z/s =0.25 (symbols denote the experimental data [60]) 117
Figure 6-13 Swirl contour and flow streamlines in outer wheel-space for the double axial-clearance, $\lambda_T = 0.223$ 118
Figure 6-14 Swirl ratio distribution for double and single axial-clearance seal, z/s =0.25 118

Figure 6-15 The computed variation of effectiveness with Φ_o for the double axial-clearance seal for (a) the outer sampling point and (b) the inner sampling point (symbols denote the experimental data [54]) 120
Figure 6-16 Velocity vectors and sealing effectiveness around the inner seal region for the double axial-clearance seal, $\lambda_T = 0.019$ 121
Figure 6-17 The radial distribution of effectiveness on stator for the double axial-clearance and single axial-clearance seals (symbols denote the experimental data [60]) 122
Figure 6-18 Experimental data for double radial-axial-clearance seal with EI ingress [60] 123
Figure 6-19 Swirl ratio distribution for the radial-axial-clearance seal, z/s =0.25 (symbols denote the experimental data [60]) 124
Figure 6-20 The computed variation of effectiveness with Φ_o for the radial-axial-clearance seal for outer sampling point (symbols denote the experimental data [60]) 125
Figure 6-21 The radial distribution of effectiveness on stator for the radial-axial-clearance seal and the single radial-clearance seal (symbols denote the experimental data [60]) 126
Figure 6-22 The computed variation of effectiveness with Φ_o for all rim seal geometries (The open symbols denote the experimental data [60], the closed symbols denote the computed effectiveness and the line is theoretical curves [60]).....127

List of Tables

Table 3-1 The Wilcox $k-\omega$ model constants 52

Table 3-2 Computational parameters for 3D computations 57

Table 5-1 Computational parameters for Mass-weighted and Momentum-weighted average assumptions 82

Table 6-1 Computational parameters for the radial-clearance seal 109

Table 6-2 Computational parameters for the double axial-clearance seal 116

Table 6-3 Computational parameters for the radial-axial-clearance seal 124

Nomenclature

A Area

a Radius of sealing flow or superposed flow inlet

b Radius of seal

c Concentration

c_p Specific heat capacity

C_p Pressure coefficient $(= (p - \bar{p})/(1/2\rho\Omega^2 b^2))$

C_w Non-dimensional flow rate $(= \dot{m}/\mu b)$

$C_{w,i}$ Values of C_w for ingress

$C_{w,o}$ Non-dimensional sealing flow rate $(= \dot{m}_o/\mu b)$

$C_{w,\min}$ Minimum value of $C_{w,o}$ to prevent ingress

G Gap ratio $(= s/b)$

G_c Seal-clearance ratio $(= s_c/b)$

h Local convective heat transfer coefficient

k Thermal conductivity

$\dot{m}$ Mass flow rate

Nu Nusselt number

p Static pressure

$\bar{p}$ Average static pressure along one vane pitch

Pr Prandtl number

q Rotor wall heat flux

r, ϕ, z Radial, circumferential and axial coordinates

R Recovery factor

Re_ϕ Rotational Reynolds number $(= \rho \Omega b^2 / \mu)$

Re_w Mainstream flow axial Reynolds number $(= \rho W b / \mu)$

s Axial space between rotor and stator

s_c Seal clearance

T Static temperature

T_1 Static temperature at sealing flow inlet

$T_{o,1}$ Total temperature at sealing flow inlet

T_{ref} Reference temperature

T_{rotor} Fixed temperature on rotor

T_w Static temperature on rotor

$T_{w,ad}$ Adiabatic disc temperature on rotor

V_r, V_ϕ, V_z Radial, tangential and axial components of velocity

W Axial velocity in annulus

x Non-dimensional radial location $(= r / b)$

β Swirl ratio $(= V_\phi / \Omega r)$

$\overline{\beta_{in}}$ Average swirl ratio at sealing flow inlet

ε Sealing effectiveness

ε_c Concentration effectiveness

ε_c Adiabatic effectiveness for rotor

μ Dynamic viscosity

λ_T Turbulent flow parameter $(= C_{w,o}\, \mathrm{Re}_\phi^{-0.8})$

θ_∞ Non-dimensional core temperature

ρ Density

Φ Non-dimensional sealing parameter $(= C_w / 2\pi G_c \operatorname{Re}_\phi)$

Φ_i Value of Φ when $C_w = C_{w,i}$

Φ_o Value of Φ when $C_w = C_{w,o}$

$\Phi_{\min}$ Value of Φ when $C_w = C_{w,\min}$

Ω Angular velocity of rotating disc

Turbulence Model Constants

C_μ, $C_{\varepsilon 1}$, $C_{\varepsilon 2}$, σ_k, σ_ε $k-\varepsilon$ model constants

α, β, β^*, σ_k, σ_ω $k-\omega$ model constants

Subscripts

a Annulus

e Egress

EI Externally-induced ingress

i Ingress

in Initial

o Superposed flow or sealing flow

1,2 Locations in wheel-space and annulus, respectively

∞ Value in core at $z/s = 0.5$

1. Introduction

1.1. A brief history of the jet engine

According to Newton's third law of motion, the jet engine, one kind of reaction engine, forces a fluid in a certain direction in order to produce a reaction that drives the engine in the opposite direction. In modern industry, the jet engine plays a vital role in many engineering fields. Lock [1] and Rolls-Royce [2] provide an overview of the development of the jet engine.

Around the first century AD a simple practical example of jet engine, Hero's engine (Figure 1-1), was invented in Greece. Although it perhaps was used as a toy, it still was an important milestone for the birth of jet engine. With the development of human civilization, important progress for the jet engine happened in the early 20th century. In 1922, Maxime Gillaume put forward his idea of an axial jet engine in his patent [2]. In the 1930's Hans von Ohain, in Germany, and Sir Frank Whittle, in England, independently brought the idea to practice with the birth of turbojet.

Figure 1-1 A simple model of Hero's engine [1]

Hans von Ohain patented his turbojet with both axial and centrifugal compression when he studied for his doctorate at the University of Gottingen in 1934 [3]. His

design attracted the interest of an aircraft manufacturer, Heinkel. In 1937 their first joint engine used hydrogen as the fuel and consisted of a radial compressor and radial turbine (Figure 1-2). Two years later, Hans von Ohain designed his HeS3 engine, which powered the He 178 just before the Second World War. The He 178 conducted the first turbojet flight in the world. After the war, Hans von Ohain immigrated to America and worked for Wright-Patterson Air Force Base. For the next 30 years he contributed to the development of jet-powered aircraft in the US [1].

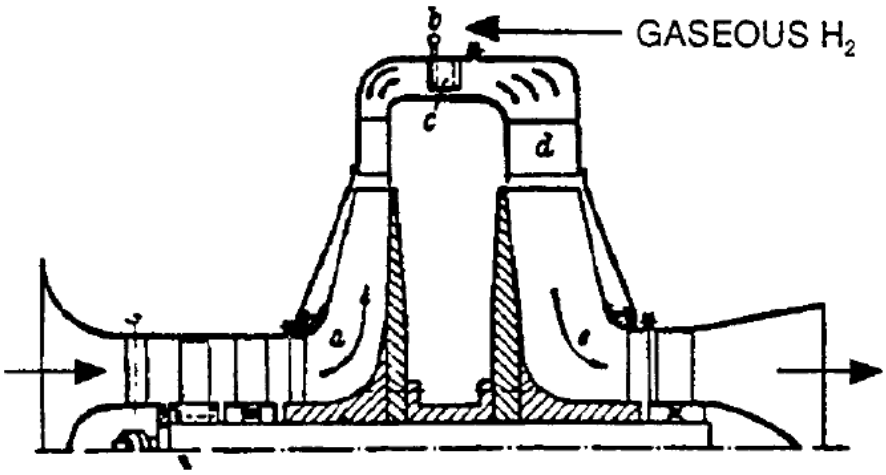

Figure 1-2 Ohain's hydrogen-fuelled turbojet engine [3]

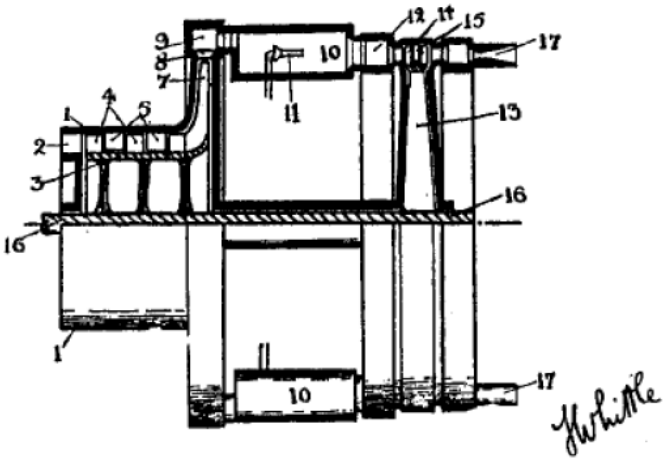

Figure 1-3 Frank Whittle's patent [1]

In England Frank Whittle patented the first practical proposal for the jet engine which he called "Improvements relating to the propulsion of aircraft and other vehicles" [1].

This patent presented a turbojet engine with an axial compressor, powered by an axial turbine (Figure 1-3). In 1935 Whittle began to build the first prototype engine with this concept. One year later he ran the world's first bench test using a jet engine with liquid fuel. After the fully successful experiments finished in 1940, the government took note on Whittle's research and the Whittle engine was used to power a Gloster E28/39 experimental aircraft. In 1944, Rolls-Royce produced an improved Whittle engine to power the Gloster Meteor 1 twin-engined fighter [1]. After the Second World War, Whittle was proclaimed the "father of the jet engine".

Hans von Ohain and Frank Whittle were not the only people who promoted the research of the jet engine. At the same time, many other pioneers also made great efforts for the development of this engine. For example Rene Lorn, a French engineer, patented a ramjet in 1913 [1] and A.A. Griffth published an analysis of an axial turbine in 1926 [2]. Owing to the effort of these pioneers, the jet engine has played a vital role in modern industry. Many kinds of jet engine have applied to power civil and military aircraft, ship, electricity generator and oil pumping.

1.2. Gas turbine

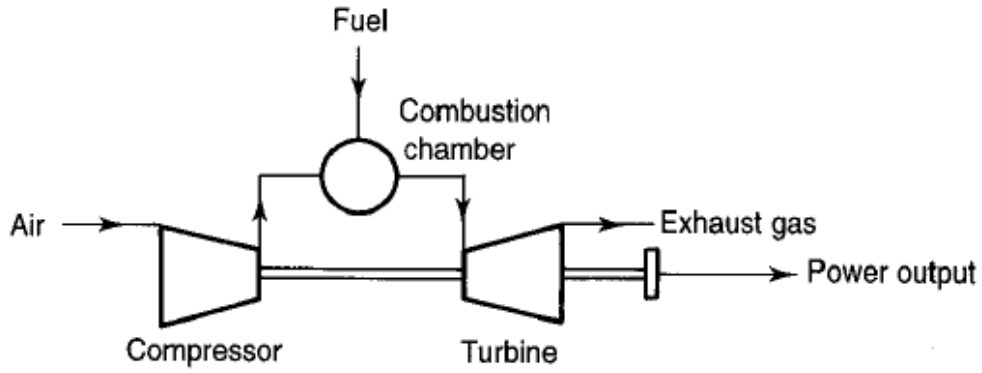

Figure 1-4 Simple gas turbine system [4]

In modern industry most jet engines are gas turbines, extracting energy from

combustion gases. The three main parts of a gas turbine are an upstream compressor, a downstream turbine and a combustion chamber in the middle (Figure 1-4). The inflow air is pressurised in the compressor and is heated with injected fuel in the combustion chamber. After the combustion process, the mixed gas is expanded through the turbine and finally exits from a nozzle to produce thrust. The compressor is driven by the turbine through a connecting shaft. The working cycle of gas turbine is called Brayton cycle. The ideal cycle is described as three processes: isentropic compression, constant pressure combustion and isentropic expansion. A typical working cycle of a turbojet engine is shown in Figure 1-5. According to the figure, pressure significantly increases in the compressor with a small drop in the combustion chamber (in the ideal situation, pressure stays constant). Finally, the pressure reduces in the turbine as the gas expands. Normally the pressure rise in the compressor is larger than the pressure drop in the turbine. Therefore, at the end of working cycle, there is surplus pressure to produce the thrust of engine.

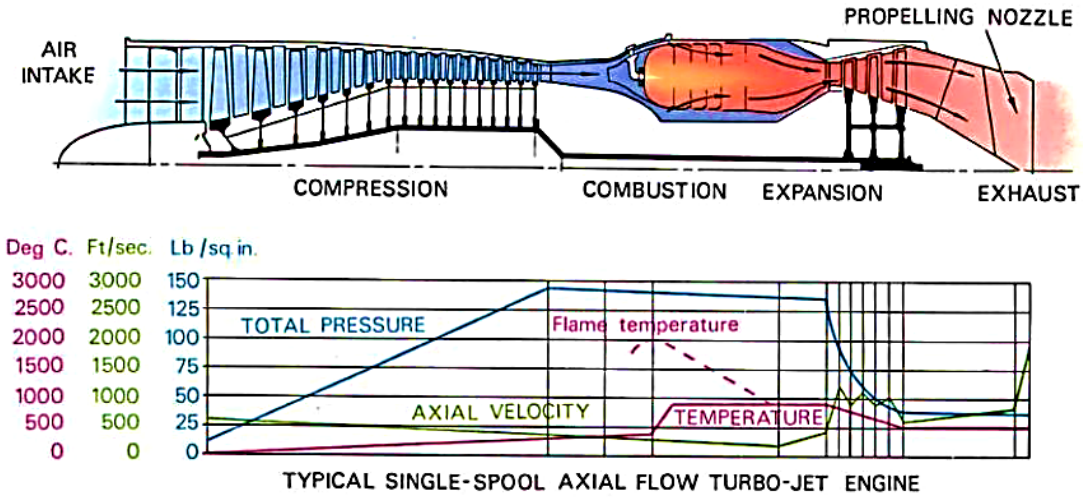

Figure 1-5 Variation of pressure, temperature and velocity in a turbojet [2]

Using a non-isentropic Brayton cycle, Saravanamuttoo *et al.* [5] show that the specific work output of the gas turbine engine is dependent on both pressure ratio of compressor (PR) and turbine entry temperature (TET). Hence, engine designers aim to maximise these two parameters to gain the most powerful gas turbine. In the 1940s

the pressure ratio was about 5 and the turbine entry temperature was just 1050 K. Nowadays the Rolls-Royce Trent 900 has a pressure ratio of 42 and the TET rises to around 1800 K at take-off [2]. The high TET gives rise to a cooling problem for the engine designer. Although metallurgical technology has developed substantially, it cannot fully satisfy the requirements and demands for TET. The melting point of cast alloys used for turbine blades is around 1550 K, which is much lower than the modern TET. Therefore most engine designers require internal cooling technology to protect turbine components in the high-temperature working environment.

1.3. **Internal cooling**

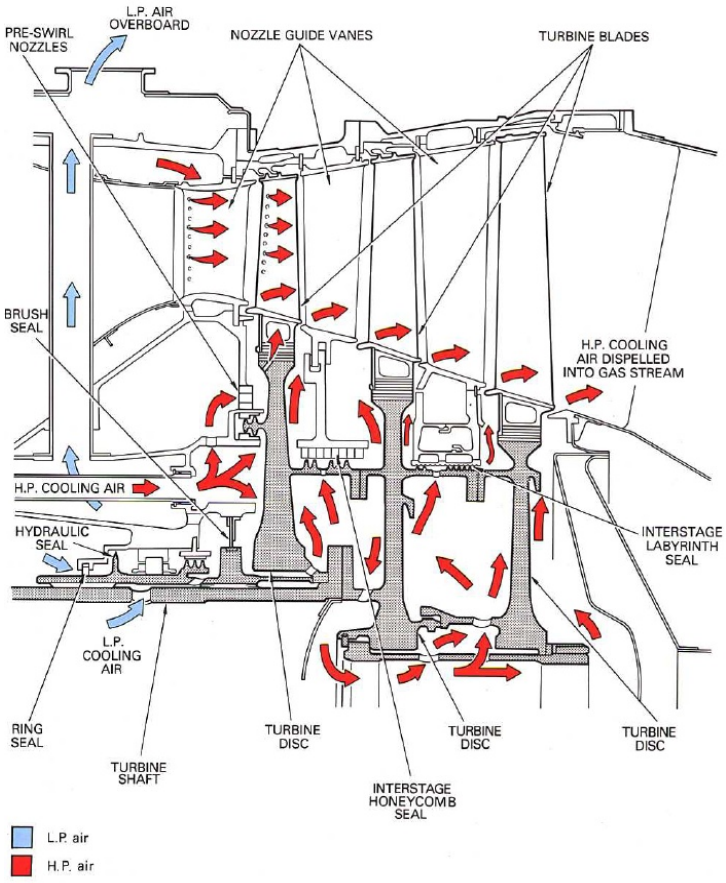

Figure 1-6 Internal cooling system, including cooling paths [2]

In the gas turbine, some of the compressed air does not enter the combustion chamber

instead it is used for cooling turbine components and sealing. The pressure drop in the combustion chamber creates a pressure difference between the compressor and turbine which drives the cool air flow into the turbine. In modern gas turbine engine about 20% of the compressed air is applied to internal cooling system. However, surplus compressed air used as coolant would lead to lower engine efficiency. For this reason, an effective cooling system is vital for keeping a high efficiency in the gas turbine engine.

In the internal cooling system, coolant flow is directed not only to the turbine nozzle guide vanes and blades, but also to the turbine cavities between the stator and rotor. A typical internal cooling system is shown in Figure 1-6. In the modern engine multiple-feed, multiple-pass and extensive film cooling (Figure 1-7) is applied to the first-stage vanes and blades which are exposed to the highest working temperature. The coolant flow passes through internal passages and cools the blades from inside. The flow exits from the blades through many tiny surface holes, creating a protective film to cool the exterior of blades.

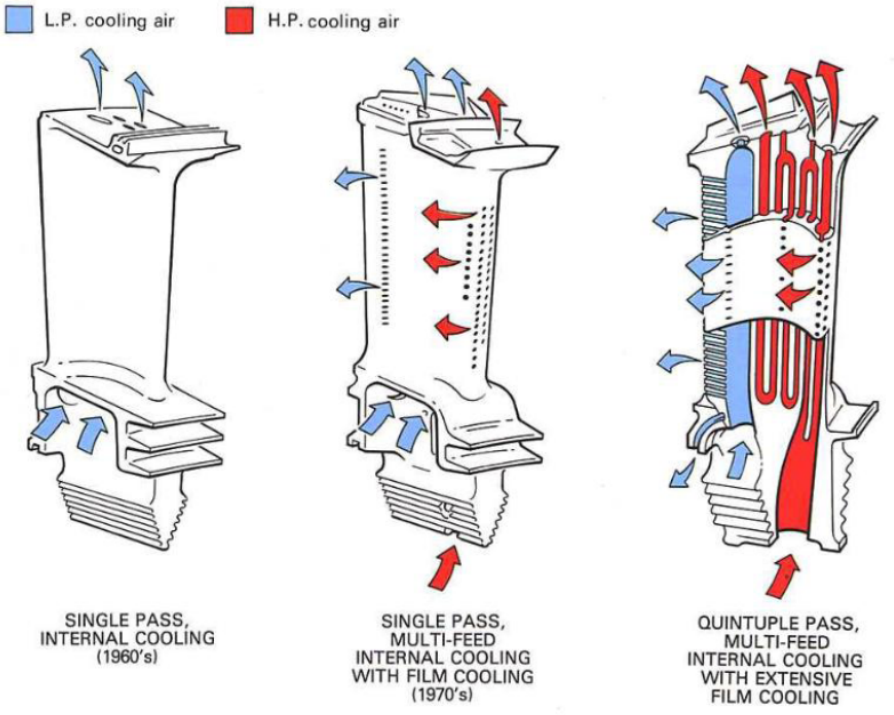

Figure 1-7 Film cooling for turbine blades [2]

1.4. **Ingress**

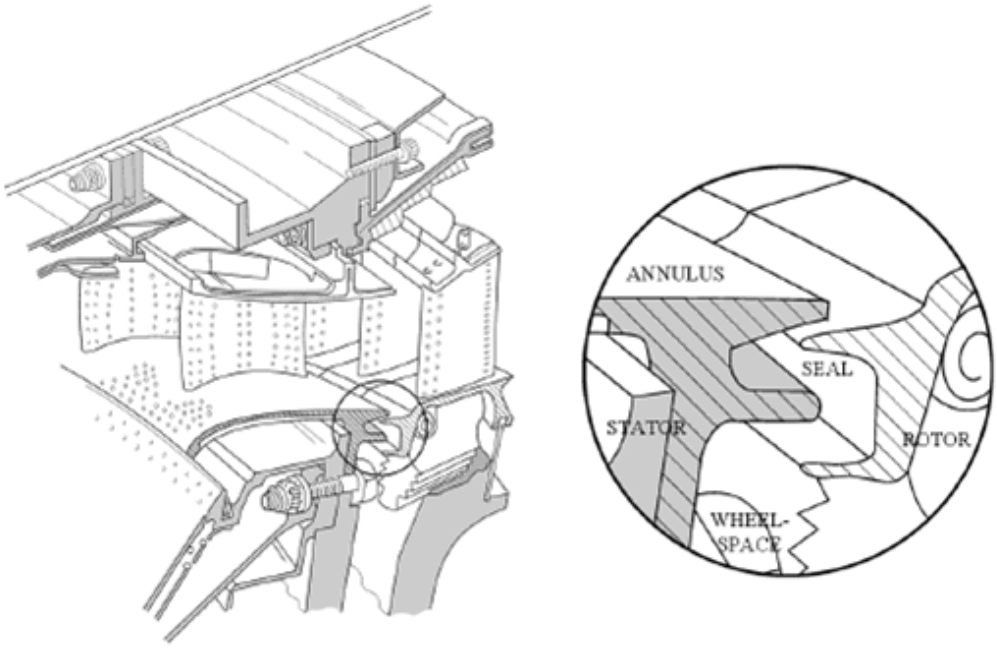

Figure 1-8 Generic rotor-stator turbine stage and double clearance-seal inset [6-7]

Figure 1-8 shows a typical high-pressure gas turbine rim seal, which is used to prevent or reduce the amount of hot mainstream gas from the annulus that is ingested into the wheel-space between the rotor and the stator. Sealing air, supplied from the compressor, is fed into the wheel-space and the air can be used to control the amount of ingested gas (referred as ingress). Too little sealing air can cause overheating and fatigue and reduce operating life of the discs, however too much can reduce the engine efficiency.

According to theoretical studies [6-7], there are two kinds of ingress; externally-induced (EI) and rotationally-induced (RI) ingress. Externally-induced (EI) ingress occurs when the external pressure distribution is non-axisymmetric, which is created by the flow past the stationary vanes and rotating blades in the turbine annulus. Ingress and egress occur through some parts of the seal clearance where the external pressure in the mainstream is higher and lower respectively than that in the

wheel-space. On the other hand, even when the external distribution of pressure is axisymmetric, rotationally-induced (RI) ingress can still occur. The rotating fluid in the wheel-space creates a radial gradient of pressure, so that the pressure inside the wheel-space can drop below that outside, which leads to ingress of external fluid through the rim seal into the wheel-space along the stator surface. Meanwhile, the 'disc-pumping effect' causes egress near the rotor.

At the University of Bath, experiments, theoretical models and Computational Fluid Dynamics (CFD) jointly contribute to the understanding of the fluid dynamics and heat transfer associated with ingress and optimal seal performance.

1.5. **Thesis aim and objectives**

The main aim of this PhD thesis is to establish a simple computational model to predict the sealing effectiveness of externally-induced ingress for engine designers. This model also provides useful information about the fluid dynamics and heat transfer in the wheel-space. The 2D model is a great simplification to the complex, and costly, 3D unsteady CFD codes run by gas-turbine companies such as Siemens. The engine designers need a simple and cost-effective design tool to rapidly attest engine seal components.

To accomplish this aim, three key objectives were completed in this thesis:

1. Two typical axisymmetric rotor-stator system models without ingress were established, in order to understand the fluid dynamics and heat transfer of the wheel-space in the situation without ingress. The effects of geometry and turbulence model were also studied. The axisymmetric rotor-stator model was validated against experimental data from the literature.
2. The axial-clearance seal is firstly considered for a prescribed ingestion model. A mass-weighted average boundary condition is applied to this model and the

optimal layout of ingress inlet and egress outlet was selected through computations. The sealing effectiveness (on the stator and rotor), fluid dynamics and heat transfer were investigated and were shown to be in reasonable agreement with the experimental results from the test rig at the University of Bath.

3. Three other seals are also presented in this thesis: the radial-clearance seal, double axial-clearance seal and radial-axial-clearance combination seal. In accordance with the axial-clearance seal, the sealing effectiveness and fluid dynamics in the wheel-space were investigated for these seals and compared with experimental data. Finally, the performances of these four sealing geometries were ranked.

1.6. **Thesis overview**

Chapter 1 gives an introduction to the historical development of jet engine and gas turbine and discusses the internal cooling problem in the gas turbine engine. A simple introduction to ingress, the main issue in this thesis, is presented.

Chapter 2 presents a literature review, discussing the previous and current research on rotor-stator systems and ingress.

Chapter 3 presents the computational method used in this thesis and introduces the turbulence model and energy equation selected in the CFD code. Some results from 3D steady simulation are also shown in this chapter.

Chapter 4 presents the simulation for two typical axisymmetric rotor-stator system models without ingress. The fluid dynamics and heat transfer of the wheel-space without ingress as well as the effects of geometry and turbulence model are discussed in these computations. Most results show good agreement with experimental data from the literature.

Chapter 5 presents the prescribed ingestion model applied to the axial-clearance seal.

The mass-weighted average boundary condition and the layout of ingress inlet and egress outlet are considered in this chapter. The sealing effectiveness (on the stator and rotor) as well as the fluid dynamics in the wheel-space and heat transfer is investigated. Reasonable agreement with the experimental results from the rig in the University of Bath is demonstrated.

Chapter 6 presents results associated with three other seal geometries (radial-clearance seal, double axial-clearance seal and radial-axial-clearance combination seal). The sealing effectiveness and fluid dynamics within the wheel-space are investigated and the four seal geometries are ranked in terms of performance.

Chapter 7 presents the main conclusions of this thesis and some possible future work.

1.7. **Publications**

Wang, L. and Wilson, M., 2012, Computations of Flow and Heat Transfer in a Rotor-Stator System with Externally-Induced Ingestion. *International Journal of Gas Turbine, Propulsion and Power Systems*, 4 (1), pp. 10-18.

This is included as Appendix.

2. Literature review

This chapter firstly provides an introduction to the fundamental fluid dynamics and heat transfer for rotor-stator systems. After that, previous studies for ingress through gas turbine rim seals are presented. The literature review includes experimental and computational studies for understanding the ingress phenomenon. Lastly, theoretical research (the orifice model) and experiments carried out on the University of Bath gas turbine test rig are introduced.

2.1. Rotor-stator systems

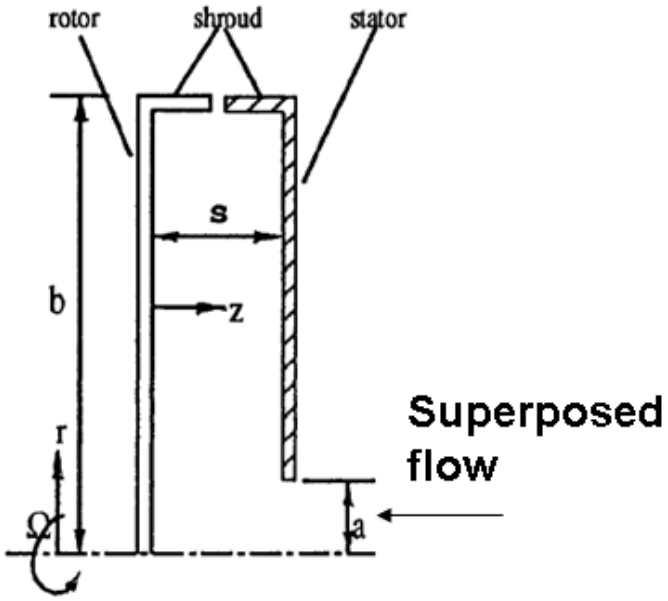

Figure 2-1 Generic rotor-stator configuration [8]

As described in Chapter 1, a rotor-stator system in a gas turbine involves a disc rotating next to a stationary casing, termed the rotor and stator, forming a cavity known as a wheel-space. The system is defined as the rotor of diameter, b, rotating at an axial distance s from the stator, as shown as Figure 2-1. This figure also shows

a superposed flow in entry near the axis of the system; in an engine, this is the cooling air used to remove heat from the turbine rotor disc. Batchelor [9] proposed an initial model for the flow between rotating and stationary discs (Figure 2-2). The model suggested that there is a rotating fluid core between the two discs with an angular velocity of magnitude between zero and Ω (the angular velocity of rotor). The model also implied that two separate boundary layers would exist in the system. The boundary layer on the rotor is similar to that on a free rotating disc; the stator boundary involves radial inflow of fluid and an efflux from the boundary layer to the core. In this type of flow, Owen and Rogers [10] showed that two non-dimensional parameters, core swirl ratio and the turbulent flow parameter, are important to the flow structure in the wheel-space. The core swirl ratio is defined as the ratio of the tangential velocity component ($V_\phi / \Omega r$) inside the rotating core to the angular velocity of the rotor at same radius. The turbulent flow parameter, λ_T, combines the rotational Reynolds number ($\mathrm{Re}_\phi = \Omega b^2 / \nu$) and the non-dimensional superposed flow rate ($C_w = \dot{m} / \mu b$).

$$\lambda_T = C_w \, \mathrm{Re}_\phi^{-0.8} \tag{2-1}$$

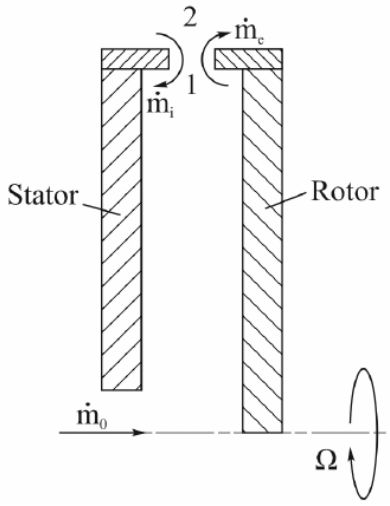

Figure 2-2 Batchelor-type flow in a rotor-stator system [9]

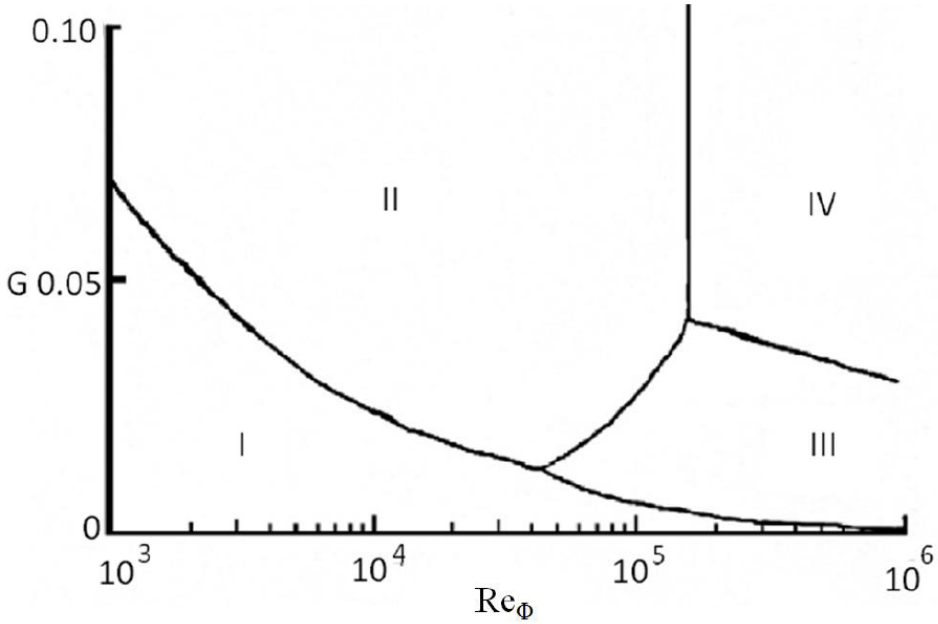

Figure 2-3 Flow regimes for a closed rotor-stator system [11]

In 1960, Daily and Nece [11] carried out experiments for a closed rotor-stator system ($\dot{m} = 0$) and proposed flow regimes in the wheel-space dependent on the rotational Reynolds number and the axial gap ratio, $G = s/b$, as shown in Figure 2-3:

Regime I: Laminar flow, small clearance with merged rotor-stator boundary layers

Regime II: Laminar flow, large clearance with separate rotor-stator boundary layers

Regime III: Turbulent flow, small clearance with merged rotor-stator boundary layers

Regime IV: Turbulent flow, large clearance with separate rotor-stator boundary layers

Chen *et al.* [8] carried out experiments for a rotor-stator system and presented measurements of velocity and Nusselt number. In the experiments, LDA measurements were made for radial and tangential velocities, and fluxmeters were used to measure the heat transfer on the heated rotor. The velocity profiles for no superposed flow, shown in Figure 2-4, illustrated that the flow structure was in accordance with Batchelor flow, with a radial outflow on the rotor ($z/s = 0$), a radial inflow on the stator ($z/s = 1$) and with an inviscid rotating core between the two boundary layers. The experiments with superposed flow found that the (un-swirled)

superposed flow reduces the core swirl ratio and also reduces the radially inward flow on the stator. Computations carried out by Wilson *et al.* [12] gave similar results for flow structure and velocity.

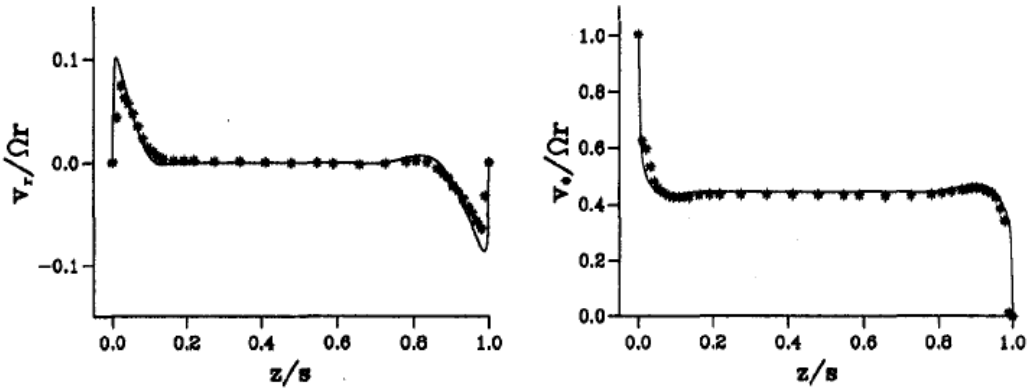

Figure 2-4 Radial and tangential velocity profiles in a rotor-stator wheel-space [8]

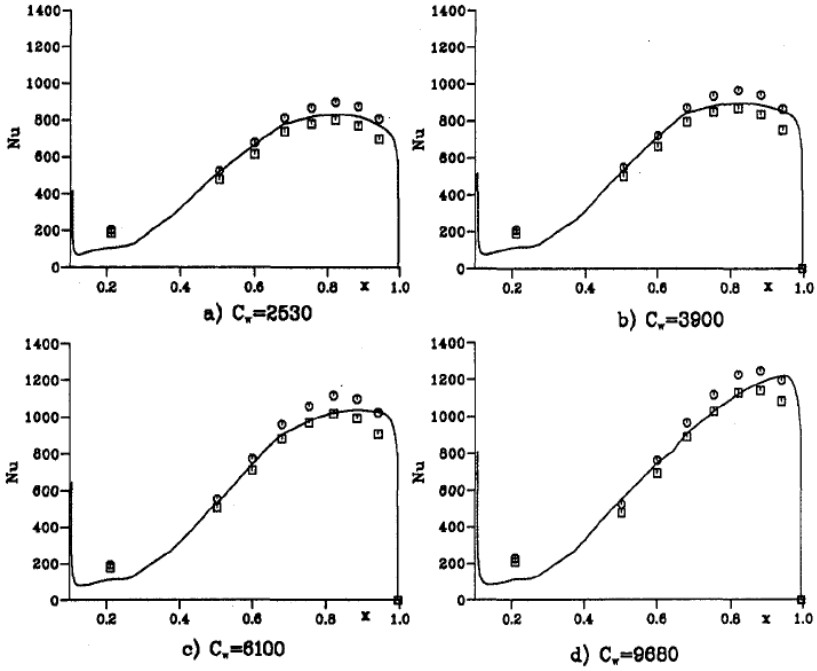

Figure 2-5 Measured and computed Nusselt numbers, $\mathrm{Re}_\phi = 1.25 \times 10^6$ [8]

○ uncorrected measurements; □corrected measurements; — computations

Furthermore, the results shown in Figure 2-5 demonstrated that Nusselt numbers increase with increasing flow rate ($C_w = 2530 \sim 9680$, $\lambda_T = 0.034 \sim 0.128$) at a given rotational speed. The corresponding computations agreed best with

measurements corrected to take heat transfer due to radiation into consideration, as shown in Figure 2-5.

Do Soghe *et al.* [13-14] developed improved correlations for the core swirl ratio and improved a correlation for the rotor disc pumped mass flow rate in order to improve a one-dimensional rotor-stator modelling approach.

Pelle and Harmand [15-16] made a series of heat transfer experiments for a rotor-stator system with an opened air-gap. They found that heat transfer depends on the rotational Reynolds number ($\mathrm{Re}_\phi = 1.29\times10^5 \sim 6.45\times10^5$) and the dimensionless spacing between the rotor and the stator [15]. They also added a central jet flow inlet to the experimental system in order to investigate the effect of the jet on heat transfer [16]. In the region of the inlet, the influence of the jet was significant and hence the local heat transfer rate increased considerably. At high radius, the heat transfer distribution was similar to the result without a jet.

Lewis *et al.* [17] carried out CFD simulations for a rotor-stator system with pre-swirl nozzles. They computed the radial and circumferential variation of Nusselt number and compared with experimental results. Based on the radial distributions of Nu on the rotor, the computed results illustrated viscous and inertial regimes for different values of turbulent flow parameter λ_T. It was suggested that the parameter $Nu\,\mathrm{Re}_\phi^{-0.8}$ was a satisfactory correlating parameter for heat transfer in the viscous regime. For the inertial regime, this parameter did not collapse either the computed or measured results. The computed circumferential variation of Nu, which was consistent with the experiments, revealed high heat transfer rates around the receiver holes, as shown in Figure 2-6. The computed streamlines are shown in Figure 2-7. Combined with measured heat transfer results, these illustrate that the flow from the nozzle can either exit through the receiver hole or continue to a higher radius and recirculate into the system and mix with the core flow.

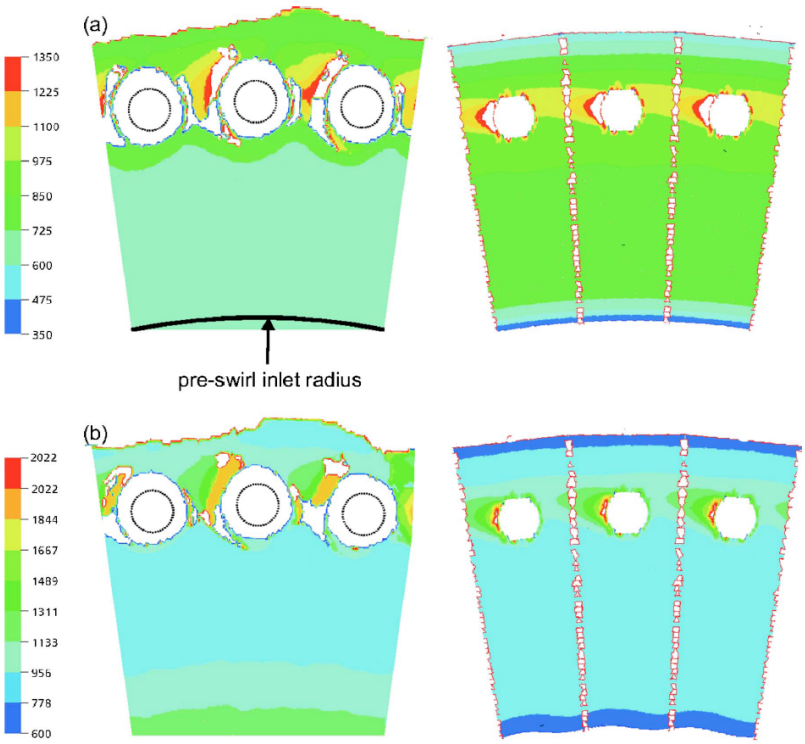

Figure 2-6 Computational (right) and experimental (left) Nusselt number contours,

$\mathrm{Re}_\phi = 0.8\times10^6$ [17]

(a) viscous regime $\lambda_T = 0.13$ (b) inertial regime $\lambda_T = 0.24$

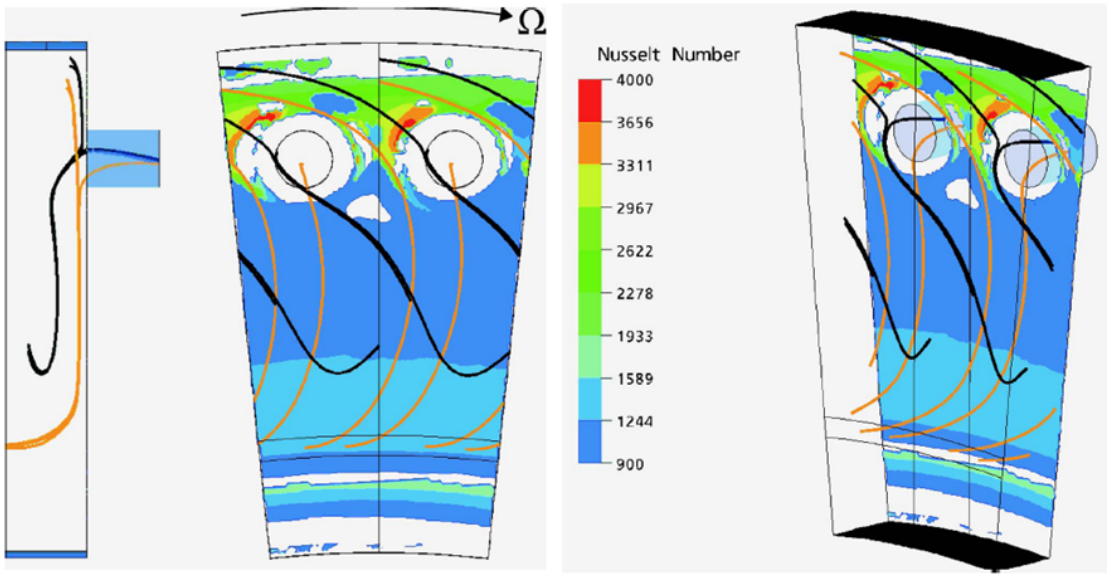

Figure 2-7 Computed streamlines superimposed onto experimental heat transfer results,

$\mathrm{Re}_\phi = 0.8\times10^6$, $\lambda_T = 0.38$ [17]

Poncet and Schiestel [18] presented two different rotor-stator systems in their computational study of heat transfer. The geometry of these two systems was the same as for published experiments. The first rotor-stator system was enclosed by a heated shroud, and an axial inlet flow was applied. The numerical results agreed with the experimental data and the authors found that a recirculation zone controlled the heat transfer ($\mathrm{Re}_\phi = 1.56 \times 10^5$, $\lambda_T = 0.19 \sim 0.61$). The second rotor-stator system consisted of a heated stator and a radially inward flow. The results from this model also had good agreement with the published experimental data, and the agreement was better than in the former case. The authors suggested that the inward radial flow in the second system, which did not impinge on any wall, might be the cause for this better agreement.

Javiya *et al.* [19] carried out CFD simulations for the pre-swirl rotor-stator system as studied by Lewis *et al.* [17] in order to test the effects of turbulence model, near wall modelling and the CFD code used on computed flow structures and heat transfer. Although most turbulence models showed reasonably good agreement with experiment, none of the models produced full details of the flow structure near the pre-swirl jets, due to the limitation of the models in complex flows. The computations gave good predictions of the heat transfer on the rotating disc at high pre-swirl flow rates. At the lowest flow rate, the heat transfer was over-predicted. The authors believed that sensitivity to heat transfer on the stator was one factor causing this over-prediction. In order to study the issue of stator heat transfer, the authors carried out computations with the stator at the same temperature as the unheated rotor rather than using an adiabatic boundary condition. The results, shown in Figure 2-8, showed that the magnitude of Nu reduced slightly when the stator heat transfer taken into account, though the effect was small. The arrows in figure show the radial locations of the pre-swirl inlets on the stator and the outlet holes on the rotor.

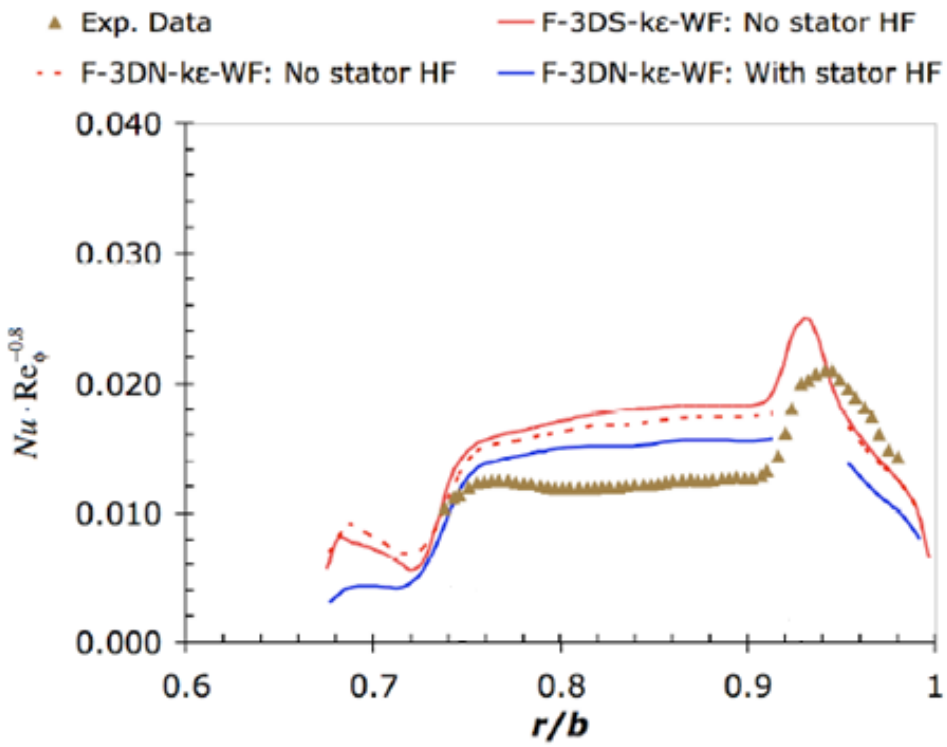

Figure 2-8 Effect of stator heat transfer on the distribution of $Nu\,\mathrm{Re}_\phi^{-0.8}$ [19]

Evans *et al.* [20] compared computational results with published experiments for a rotor-stator system using Fluent, in order to test the effects of turbulence model and mesh density on the heat transfer results. The authors applied three turbulence models, $k-\varepsilon$, $k-\omega$ and $k-\omega$ SST, and used two different mesh densities for different flow conditions. The $k-\omega$ SST model with a fine mesh agreed best with the experimental data for both the swirl velocity and the heat transfer coefficients. However, regardless of the turbulence model, poor agreement with experiments for heat transfer coefficients was obtained at low cooling flow rates and high rotational speed ($\mathrm{Re}_\phi \approx 1.0\times10^6$). The authors gave a possible explanation that relatively large ingestion at low flow rates could influence the heat transfer in the rotor-stator system. The authors recommended that future CFD simulations should apply the $k-\omega$ SST model, and that Fluent could be used with confidence when the rotational Reynolds number is below 8×10^5.

2.2. **Ingress**

Due to the importance of ingress, there are a large number of investigations about this problem, including both experimental and computational studies. Among many experimental techniques, concentration measurements are widely used in ingress studies. These use a convenient tracer gas, such as CO_2, to characterize the sealing effectiveness (ε). Solid surfaces become impermeable barriers and the boundary conditions are known. Theoretical models often neglect the effect of diffusion. In practice, diffusion can lead to non-zero ingress, which means the tracer gas used for concentration measurements can pass through the rim seal by diffusion. Therefore, at large values of sealing effectiveness, where ingress is relatively small, a theoretical model, compared with concentration measurements, may underestimate the ingress and consequently overestimate the effectiveness [6]. Computational studies have also become an indispensable component of ingress research. Over the past decade, computational fluid dynamics (CFD) has been used to compute pressure distributions, sealing effectiveness and other important ingress parameters.

Bayley and Owen [21] used a simple rotor-stator rig with an axial-clearance rim seal and without an external annulus to carry out ingress experiments. From the results, they showed that increasing the sealing flow rate can increase the relative pressure in the wheel-space, subsequently, reducing the ingested flow. They found that the minimum value of non-dimensional sealing flow rate needed to prevent ingress, $C_{w,\min}$ depends strongly on the seal clearance ratio, G_c, and the rotational Reynolds number, Re_ϕ, but is little affected by the rotor-stator clearance s. The following empirical relationship was established:

$$C_{w,\min} = 0.61 G_c \mathrm{Re}_\phi \qquad (2\text{-}2)$$

As their experiments were carried out without external flow, this empirical equation applies only for rotationally-induced (RI) ingress according to the definition above. In the following years, Phadke and Owen [22] applied flow visualization, pressure and concentration measurements to determine $C_{w,\min}$ in a rig without external flow for different seal geometries. They found that radial-clearance seals were more effective than axial-clearance ones.

Graber *et al.* [23] used concentration measurement for several rim seal geometries with no circumferential variation of the external pressure. They plotted the measured values of sealing effectiveness versus η_t, where $\eta_t = \lambda_T / 4\pi$. Through the experiments, Graber *et al.* obtained the effects of seal-clearance ratio (G_c) and Re_ϕ on variation of ε with η_t, and found no effects of external swirl on ε.

Abe *et al.* [24] used a turbine rig in experiments with vanes in the external annulus upstream of the rim seal in order to show that external flows in the annulus can also ingress. After tests of several rim-seal geometries, the authors identified three factors that affected ingress: the ratio of the velocities of the sealing air and the flow in the annulus; the rim-seal clearance; the shape of the rim-seal.

In 1988, Phadke and Owen [25-27], through many experiments using an experimental rig with an external annulus, measured the variation of $C_{w,\min}$ with the axial Reynolds number in annulus ($\mathrm{Re}_w = \rho W b / \mu$) as shown in Figure 2-9. According to the figure, when $\mathrm{Re}_w = 0$, $C_{w,\min}$ is proportional to Re_ϕ; when the value of Re_w is large, $C_{w,\min}$ is hardly affected by Re_ϕ and increases with the increasing Re_w. Phadke and Owen correlated results for different seal geometries with the following empirical relationship for externally-induced (EI) ingress.

$$C_{w,\min} = 2\pi K G_c P_{\max}^{1/2} \tag{2-3}$$

where

$$P_{\max} = \frac{1}{2} C_{p,\max} \mathrm{Re}_w^2 \tag{2-4}$$

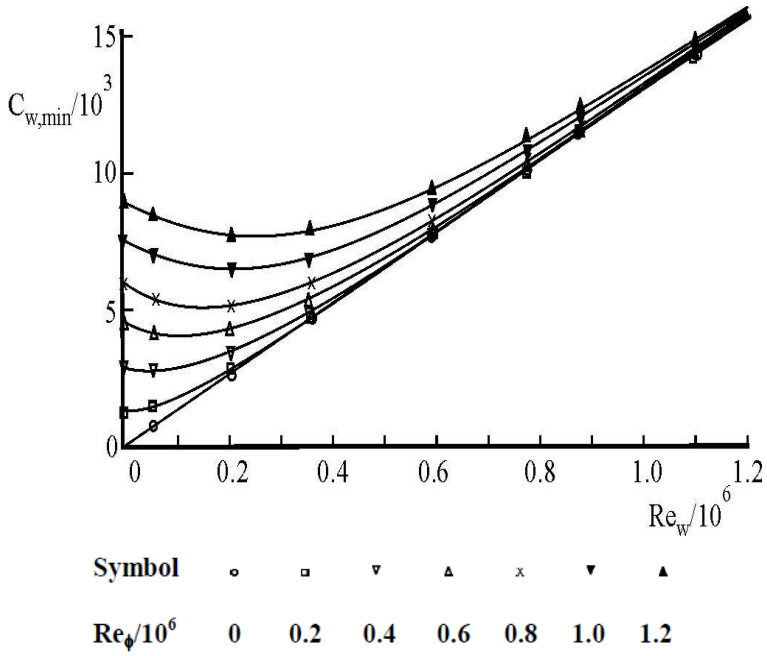

Figure 2-9 Variation of $C_{w,\min}$ with Re_w [25-27]

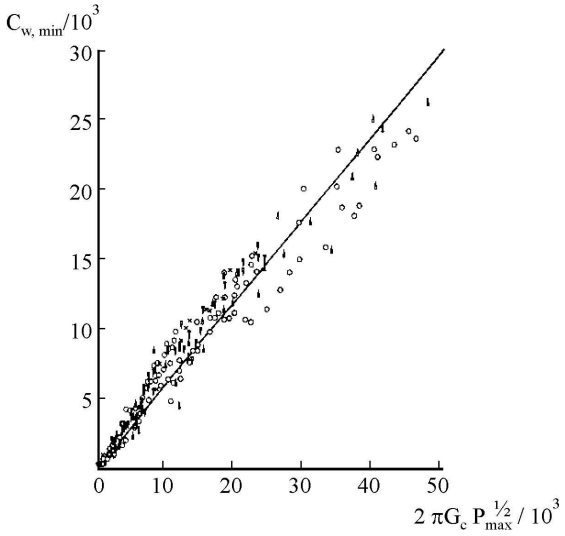

Figure 2-10 Variation of $C_{w,\min}$ with $2\pi G_c P_{\max}^{1/2}$ [25-27]

$C_{p,\max}$ is a non-dimensional pressure difference in the external annulus. K is an empirical constant and the data as shown in Figure 2-10 were correlated with $K = 0.6$. Hamabe and Ishida [28] obtained a similar empirical relationship from measurements in a turbine rig fitted with upstream vanes but not downstream blades.

The first published experimental data for a turbine rig with both vanes and blades were presented by Green and Turner [29]. For low sealing flow rates, they obtained lower ingestion than the case when vanes only were used.

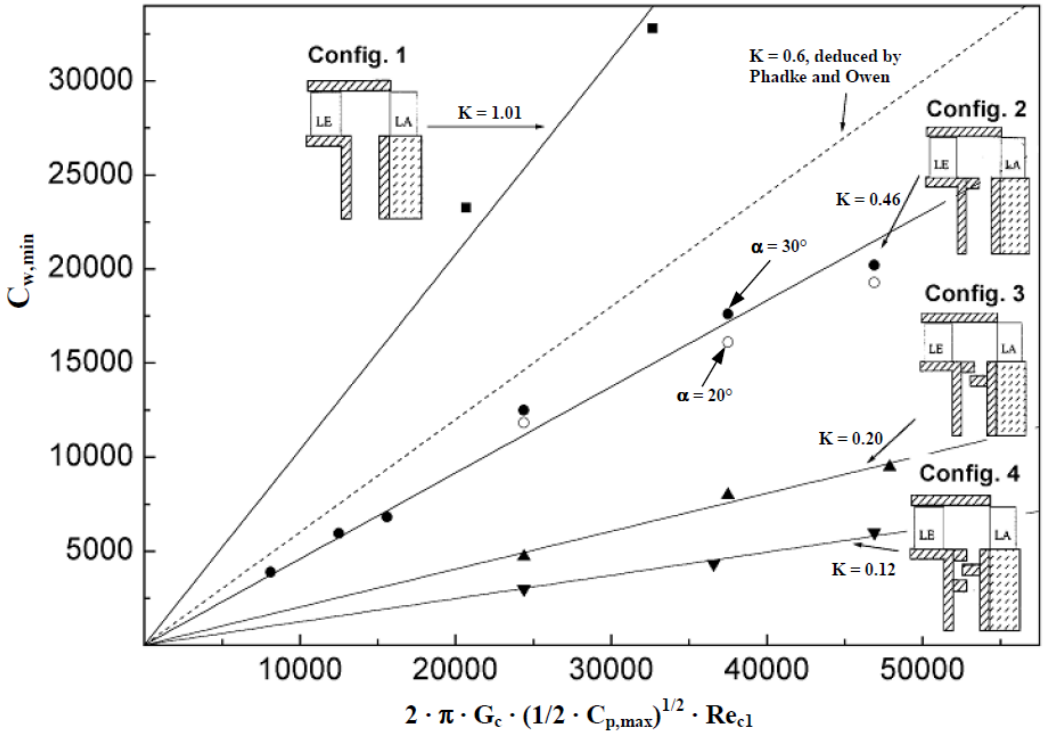

Figure 2-11 Variations of $C_{w,\min}$ with $C_{p,\max}$ [30]

Bohn and Wolff [30] also carried out experiments for a rig with both vanes and blades. They designed four different seal geometries to determine the value of $C_{w,\min}$. As shown in Figure 2-11, they also obtained a linear variation of $C_{w,\min}$ with $C_{p,\max}^{1/2}$, which is same result as Phadke and Owen [25-27]. However, they found a different

K value for different seal geometries, which is not consistent with $K = 0.6$ as observed by Phadke and Owen. Bohn and Wolff suggested that $K = 0.6$ provides a conservative estimation of $C_{w,\min}$.

The research group at Arizona State University and its cooperative research institutes [31-35] contributed greatly to the investigation of ingress. Roy *et al.* [31] described experimental measurements for a single stage axial-flow turbine with two vane-blade configurations. The main difference between the configurations was the inlet vane turning angle. The measurements suggested that the instantaneous pressure field is pivotal to ingestion. This 3D and unsteady field is influenced by the mainstream flow rate, rotor speed, and sealing flow rate.

Roy *et al.* [32] carried on the experiments for a turbine with an axially overlapping radial seal. Time-resolved velocity maps in the wheel-space were obtained by the PIV technique, as shown in Figure 2-12. According to the figure, when the sealing flow rate is low, the non-periodic red region with high tangential velocity represents the ingested air from the mainstream. The explanation for the non-periodic variation is that the relative positions of the blades and vanes do not remain the same azimuthally. On the other hand, the result for high sealing flow rate in Figure 2-12 (b) indicates that the tangential velocity is low throughout the wheel-space, which means that no ingress occurs in this case, and unsteady large-scale structures which lead to large velocity fluctuations have appeared. In short, this experimental measurement demonstrated that the ingestion flow carried high tangential velocity fluid from the mainstream to the wheel-space and the egress flow brought low tangential velocity fluid from the wheel-space to the mainstream.

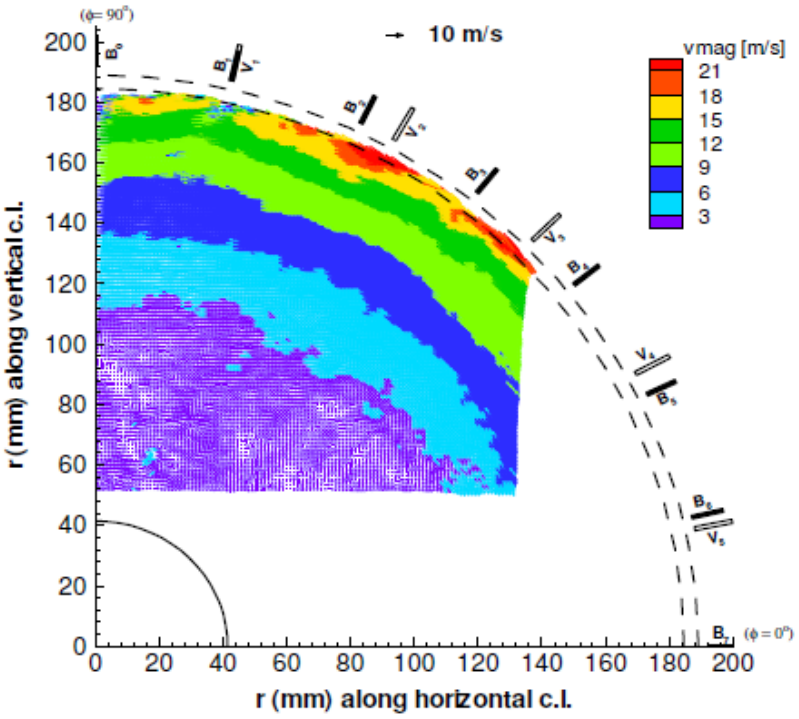

(a)

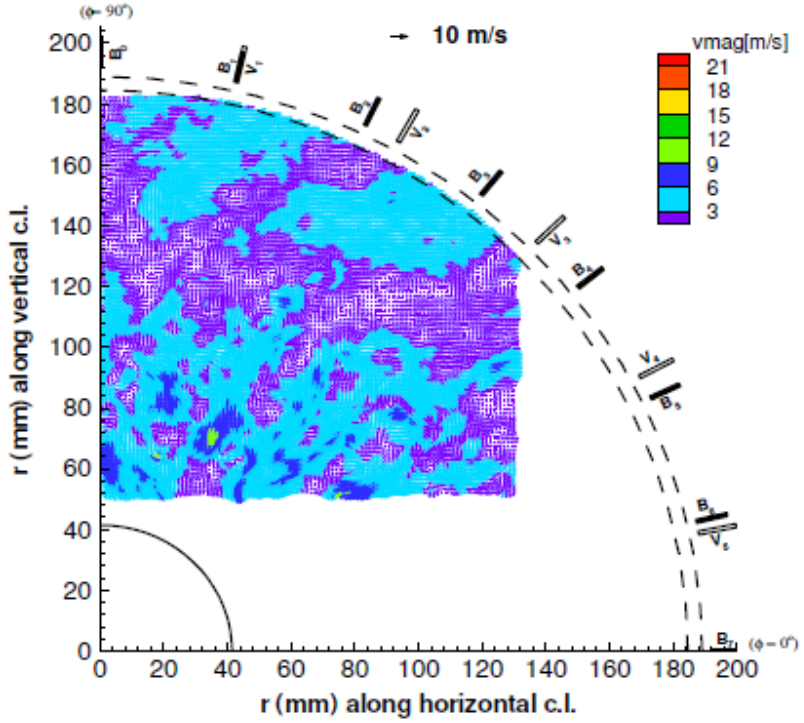

(b)

Figure 2-12 Instantaneous velocity contours in the disk cavity [32]

(a) $C_{w,o} = 1574$ (b) $C_{w,o} = 8656$

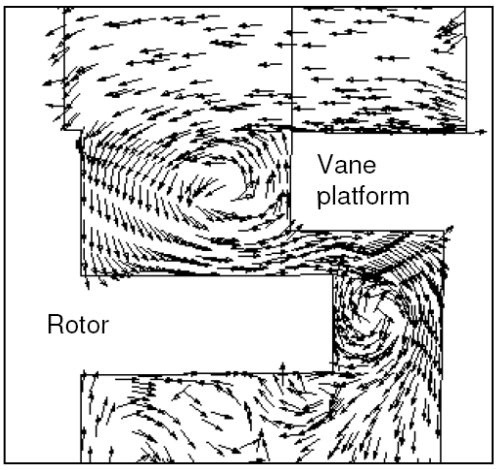

Figure 2-13 CFD velocity vectors in axial-radial plane of seal region [32]

Roy *et al.* [32] also described an unsteady, three-dimensional CFD model of a single-stage axial turbine having similar geometry with their experimental rig including vanes, blades and an axially overlapping radial clearance rim seal. The computational sector model had one blade and one vane along with the rim seal and wheel-space. The computations were carried out using Fluent Version 6.2. The velocity vectors in the axial-radial plane (Figure 2-13) indicated that a recirculation cell was formed downstream of the vane platform. A second recirculation cell exists simultaneously at the rotor side of the rim seal. Furthermore, the radial, axial, and tangential velocity contours revealed that some rapid changes in direction and magnitude occur in some gap regions. The velocity contours also demonstrated that when ingress occurs, both the axial velocity and tangential velocity are greater than when egress occurs, which is consistent with their measurements.

Zhou *et al.* [33] continued the experiments and computations for three wheel-space configurations with different aspect ratios (Config.1 having the maximum value and Config.3 is the minimum). At low sealing rate, they also identified the regions of ingress and egress around the rim seal through PIV images of instantaneous velocity. Another essential result shown in Figure 2-14 is that ingested air from the external annulus into the wheel-space decreased, and consequently the sealing effectiveness

increased, as the wheel-space aspect ratio became smaller. For computations, the simulation for a 14.4° sector model under-predicted ingested hot air into the wheel-space compared with measurements. One possible reason presented by authors is that the sector model can not predict the circumferentially rotating low-pressure regions which are able to augment ingestion.

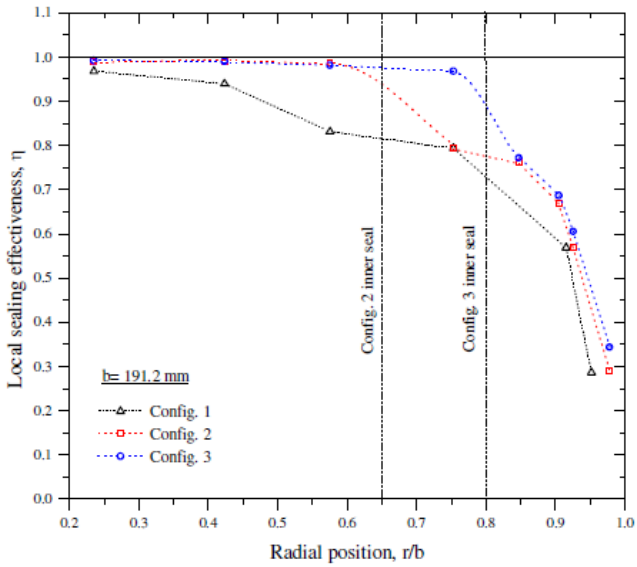

Figure 2-14 Comparison of local sealing effectiveness at the stator [33]

Recently, Dunn *et al.* [34] reported an intensive computational study for two meshes with different solver parameters. Although both solutions had strength and weakness, both showed generally good agreement with the experimental results.

Gentilhomme *et al.* [35] conducted both pressure and concentration measurements for a single stage turbine. The pressure measurements revealed that the ingested highly swirling mainstream gas can increase radial pressure gradients in the wheel-space at low sealing flow rate. The authors also carried out CFD studies for ingress and found that the asymmetrical pressure created by the Nozzle Guide Vanes (NGVs) was only slightly affected by the existence of rotor blades. However, the pressure asymmetry due to the rotation is very significantly influenced by the NGVs.

Lewis and Wilson [36] conducted a computational study in a simplified model of a gas-turbine rotor-stator wheel-space with an axial clearance rim seal, with non-axisymmetric flow conditions created by a stator vane in an external mainstream. They used the commercial code CFX Version 10 to investigate the effects of geometry (different axial space between the vane trailing edge and the seal) and boundary condition assumptions on results. The rotational Reynolds number used was 2.5×10^6, which is typical of values used in experiments. The other non-dimensional parameters used were of similar values to conditions in engines. Sensitivity to mesh size was tested over a wide range by using different grid sizes. Through this computational study, the fluid dynamics results illustrated that the circumferential variation of pressure coefficient, C_p, decreases with increasing distance downstream from the vane trailing edge. The sealing effectiveness was found to be approximately constant near the stator. Near the rotor, the effectiveness reduced slightly as radius increased. The dimensionless temperature on both the stator and the rotor showed that the fluid in the wheel-space was heated above the temperature of the external mainstream.

Mirzamoghadam *et al.* [37-38] reported 3D CFD computations for a full stage HP turbine disk cavity. Based on these computational results, they found that the asymmetrical annulus pressure can give rise to ingestion even at relatively high sealing flow rate. They also demonstrated that the stator wake influences ingress more than the rotor blade bow wave. In addition, Mirzamoghadam *et al.* [37] defined the ingestion mixing efficiency using temperature data. The definition is given by

$$\eta_{ing} = (T_r - T_c)/(T_h - T_c) \qquad (2\text{-}5)$$

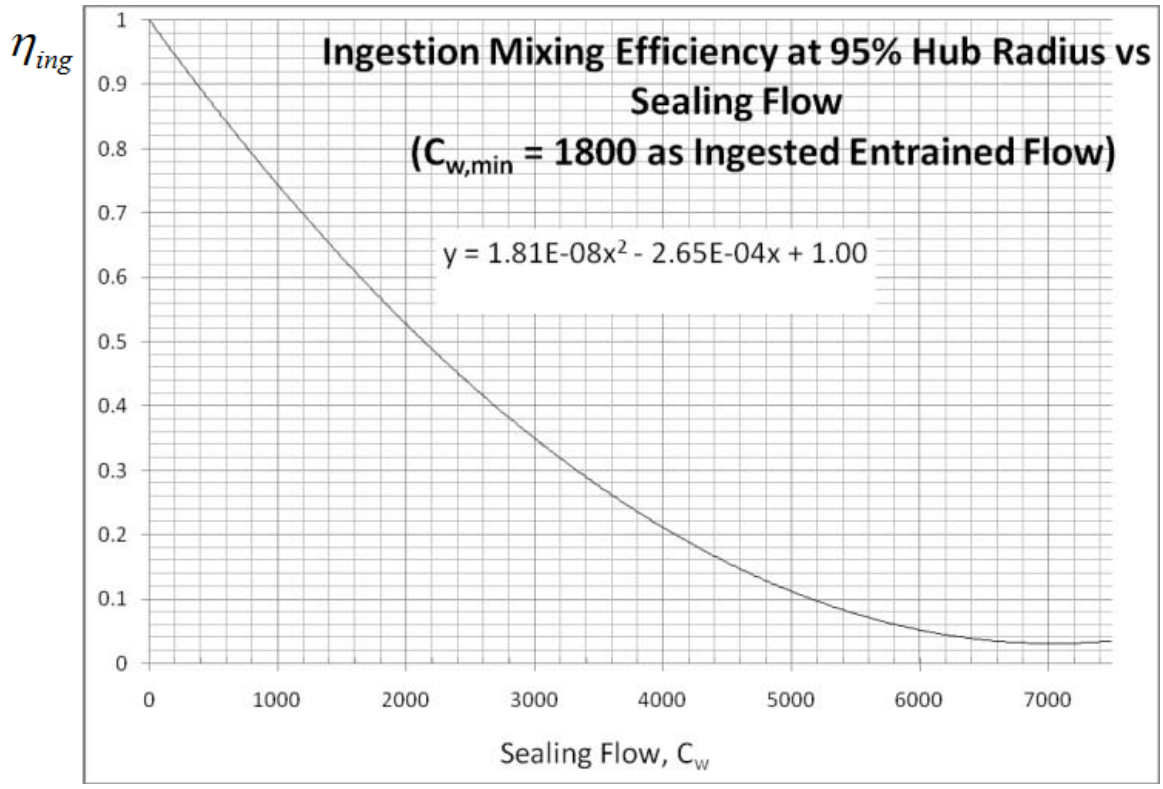

Figure 2-15 Ingestion Mixing Efficiency [37]

Here T_c, T_h and T_r are coolant inlet temperature, annulus temperature and local temperature at radius r respectively. With this definition, efficiency equal to zero at a given radius implies that no ingress occurs. As shown in Figure 2-15, the ingestion mixing efficiency reduces, which also means that the sealing effectiveness increases, as the sealing flow rate increases. A frictional heating correlation, which is essential for the calculation of heat transfer in the wheel-space, was developed by Mirzamoghadam and Xiao [39].

The combined experimental and computational study of Cao *et al.* [40] showed that ingress is an incompressible flow phenomenon and that ingress can make the rotating flow in the wheel-space unstable. Although the authors mentioned that a 'segmental domain' model used in CFD may be unable to capture these instabilities, their computations for a 90° segmental model still showed good agreement with those for a full 360° domain. Nevertheless, Jakoby *et al.* [41] pointed out that their steady calculation with a simplified sector model had less good agreement with

measurements than a 360° unsteady calculation at low sealing flow rate. Recently, Rabs *et al.* [42] indicated that a full 360° model provides almost no improvement when compared to sector models, if no large scale rotating structures occur. The use of sector models was recommended due to the huge savings in computational cost.

The numerical simulations of Wang *et al.* [43] focus on the effect of the rim seal region geometry on ingress. Close- and wide-spaced turbine stages with an axial-clearance seal were tested and it was noted that the peak-to-trough pressure variation, a driving factor for ingestion, for the wide-spaced stage is much less than that for the close-spaced stage. For time-averaged calculations, both close- and wide-spaced stages produce approximate ingestion characteristics, however, the characteristics for the close-spaced configuration were significantly changed with time, which is consistent with the high variation in the gas path pressure field.

Laskowski *et al.* [44] compared steady and unsteady simulations of ingress. According to contours of effectiveness in the wheel-space and rim seal region (Figure 2-16), the steady results show no ingestion for three different circumferential locations, however ingestion is present at all three locations in the time-averaged unsteady result. The authors also compared effectiveness based on concentration and temperature for the stationary blade and rotating blade cases. If the rotor blade was stationary, these two definitions of effectiveness give similar results. In the rotating blade case, the effectiveness based on temperature gave a lower value in the wheel-space than that based on concentration. The authors pointed out that windage (frictional heating), which increases the temperature in wheel-space and consequently reduces the effectiveness, is the main reason for the difference between the two kinds of effectiveness.

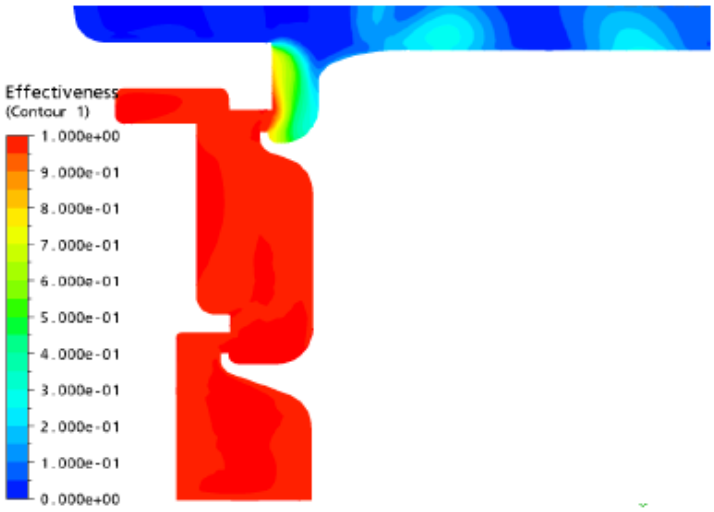

(a) Steady state CFD

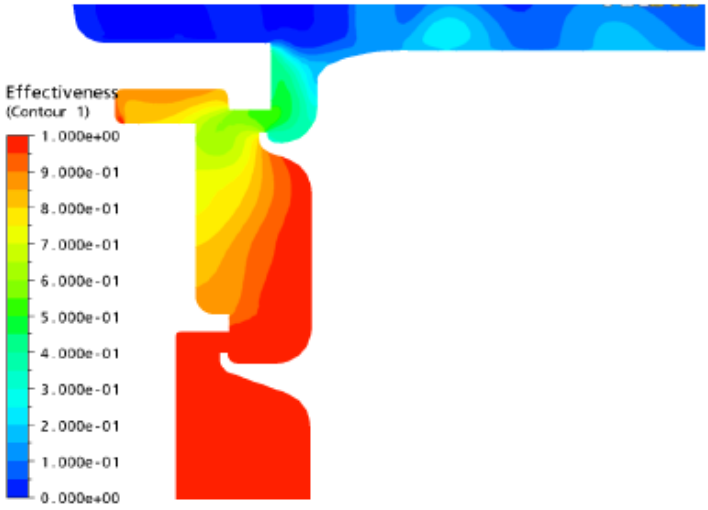

(b) Time-averaged Unsteady CFD

Figure 2-16 Steady state and time-averaged unsteady buffer cavity effectiveness [44]

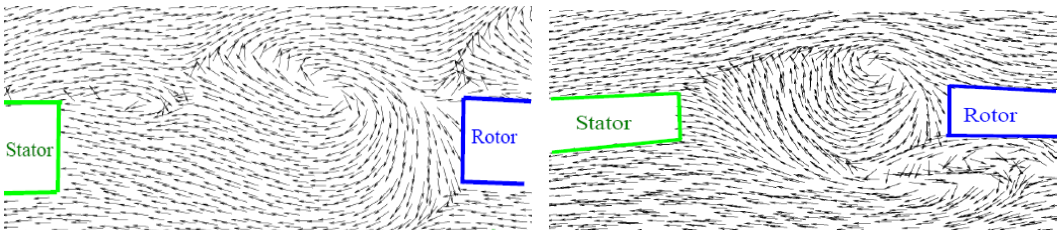

(a) simplified turbine rim seal model (b) full 1.5 stage turbine model

Figure 2-17 Velocity vectors in the gap [45]

Rabs *et al.* [45] carried out computations for a simplified turbine rim seal model without vanes or blades and a full 1.5 stage turbine model in order to verify that

Kelvin-Helmholtz vortices could occur in the rim seal region. Both models showed the existence of Kelvin-Helmholtz vortices and occurrence of ingress as shown in Figure 2-17. The authors indicated that the Kelvin-Helmholtz vortices obtained by the full 1.5 stage turbine model are weakened by the interaction of the vanes and the blades, which was not included in the simplified turbine seal model.

O'Mahoney *et al.* [46] presented steady Large-Eddy Simulations (LES) results for a turbine rim seal ingestion compared with published experimental data and an unsteady RANS simulation. The results demonstrated that LES predicts more ingestion through the rim seal than the unsteady RANS simulation, and accordingly gives a closer agreement with experimental measurements of sealing effectiveness. The CFD simulation of Julien *et al.* [49] produced large scale flow structures for no purge flow and low purge flow rates, and illustrated that increasing the sealing flow rate can reduce the circumferential pressure variations in the wheel-space hence improve the sealing effectiveness.

Teuber *et al.* [48] carried out URANS computations to investigate the fluid mechanics in a 3D model of a turbine stage. The computed swirl ratios in the wheel-space have good agreement with measured values. The authors indicted that the minimum sealing flow required preventing ingestion increases as the annulus Mach number increases.

2.3. **Previous research at University of Bath**

The research group at the University of Bath has devoted efforts to theoretical, experimental and computational studies on the subject of ingress.

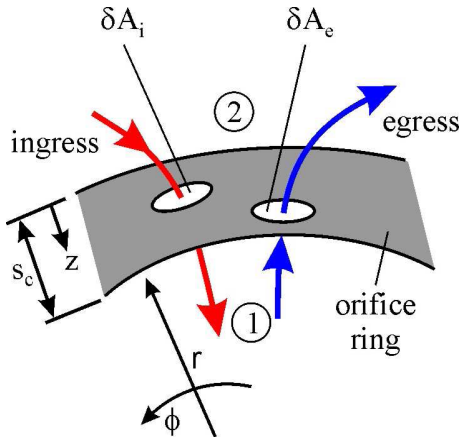

Figure 2-18 Orifice ring [49-52]

Owen *et al.* [6-7, 49-50] developed orifice models for the ingress problem. The orifice equations are based on an 'orifice ring', as shown in Figure 2-18. According to the orifice model, egress and ingress simultaneously cross different parts of the orifice ring through elemental areas, the sum of which is equal to the clearance area of the seal. Egress flows into the external annulus through a stream tube from the wheel-space. Conversely, ingress starts in the annulus and ends in the wheel-space. The main 'orifice assumptions' for inviscid flow are that rV_ϕ is constant and $(r_2 - r_1)/r_1 << 1$ (r_1 and r_2 are radius of locations in wheel-space and annulus, as shown in Figure 2-18). Meanwhile, it is assumed that the axial and tangential gradients of velocity are much smaller than the radial. Lastly, although the equations are derived for inviscid flow, discharge coefficients, C_d are introduced to account for losses. Through the theoretical model, the equations for effectiveness and for non-dimensional flow parameter for ingress Φ_i $(= C_{w,i} / 2\pi G_c \operatorname{Re}_\phi)$ are obtained.

For EI ingress:

$$\frac{\Phi_o}{\Phi_{\min,EI}} = \frac{\varepsilon}{[1+\Gamma_c^{-2/3}(1-\varepsilon)^{2/3}]^{3/2}} \tag{2-6}$$

$$\frac{\Phi_{i,EI}}{\Phi_{\min,EI}} = \frac{1-\varepsilon}{[1+\Gamma_c^{-2/3}(1-\varepsilon)^{2/3}]^{3/2}} \tag{2-7}$$

For RI ingress:

$$\frac{\Phi_o}{\Phi_{\min,RI}} = \frac{\varepsilon}{[1+(1-\varepsilon)^{1/2}][1+\Gamma_c^{-2}(1-\varepsilon)]^{1/2}} \tag{2-8}$$

$$\frac{\Phi_{i,RI}}{\Phi_{\min,RI}} = \frac{1-\varepsilon}{[1+(1-\varepsilon)^{1/2}][1+\Gamma_c^{-2}(1-\varepsilon)]^{1/2}} \tag{2-9}$$

Where Γ_c, the ratio of the discharge coefficients, is an empirical constant.

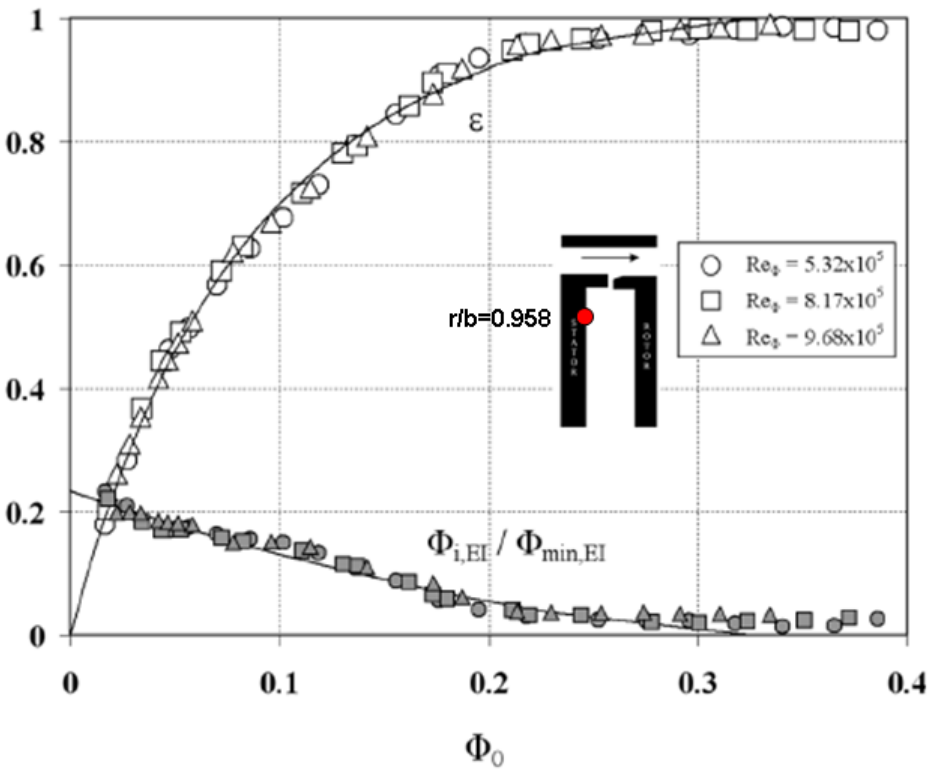

Figure 2-19 Comparison between theoretical effectiveness curves and experimental data for axial-clearance seal with EI ingress (the solid lines are theoretical curves) [51]

Sangan *et al.* [51-52] carried out experiments on rigs with axial and radial clearance

rim seals for both EI and RI ingress in order to measure the sealing effectiveness and hence deduce Φ_i. Figure 2-19 shows a comparison between the experimental data and the theoretical variation of effectiveness (at $r/b = 0.958$) according to the above equations (for EI ingress) for the axial-clearance seal. The fit between the equations and the measured variation of ε with Φ_o was optimized using a statistical model featuring the maximum likelihood estimates described by Zhou et al. [51]. The figure shows that the agreement between the optimum theoretical curves and the experimental data is very good. In 2012, Sangan *et al.* [54] extended experiments to double clearance seals and theoretical curves also agreed very well with the experimental data.

Pountney *et al.* [53] carried out heat transfer experiments on the test rig. Thermochromic Liquid Crystal (TLC) was used to measure the temperature on the rotor. Hence, the adiabatic effectiveness and the Nusselt number on rotor were obtained to determine the effect of ingestion on the rotor. CFD studies [54] have also been conducted at the University of Bath in order to compare results with the theoretical model.

2.4. **Chapter summary**

This literature review has identified past and current research relevant to ingress in rotor-stator systems; considerable experimental and theoretical research have been supported by computational fluid dynamics. However, 3D CFD models are complex, costly and not always suitable for the engine designer. The designer needs a simple, rapid computational tool to link the experimental data and theoretical models for design purposes. 2D simplified CFD model in this thesis satisfies this requirement.

3. Computational method and 3D Computations

The commercial code ANSYS-CFX Version 11.0 was used for the computations at the beginning of the study. This was upgraded to Version 13.0 after 18 months. This chapter gives a brief introduction for the turbulence model and heat transfer calculations in this code. This information is based on the release notes from the software provider. For all computations, if no other description is given, the normalized convergence residuals levels for mass, momentum and turbulence were 1×10^{-7} and 1×10^{-6} for heat transfer. All meshes were generated using ANSYS ICEM.

Some computed results from 3D steady computations are also presented in this chapter, as a preliminary study for ingress. These results include pressure in the annulus, secondary flow streamlines and sealing effectiveness.

3.1. Turbulence model

Due to the good compromise between numerical effort and computational accuracy, two-equation turbulence models are widely used in fundamental flow computations. For this kind of turbulence model, turbulent viscosity is modelled using turbulent velocity and turbulent length scale. Both the velocity and length scale are found by solving separate transport equations. The equations shown below are based on the help files from ANSYS-CFX Version 13.0.

In the k-epsilon ($k-\varepsilon$) two-equation turbulence model, the turbulent velocity is computed from the turbulent kinetic energy (k) and the turbulent length scale is estimated from the turbulent kinetic energy (k) and the turbulence eddy dissipation (ε). Hence, these two new variables are introduced into the system of equations. The continuity equation and the momentum equations are shown below:

$$\frac{\partial \rho}{\partial t} + \frac{\partial}{\partial x_j}(\rho U_j) = 0 \tag{3-1}$$

$$\frac{\partial \rho U_i}{\partial t} + \frac{\partial}{\partial x_j}(\rho U_i U_j) = -\frac{\partial p}{\partial x_i} + \frac{\partial}{\partial x_j}\left[\mu_{eff}\left(\frac{\partial U_i}{\partial x_j} + \frac{\partial U_j}{\partial x_i}\right)\right] + S_M \tag{3-2}$$

In these equations, μ_{eff} is the effective viscosity accounting for turbulence, so that:

$$\mu_{eff} = \mu + \mu_t \tag{3-3}$$

The term μ_t is the turbulent viscosity. In $k-\varepsilon$ model this is found from:

$$\mu_t = C_\mu \rho \frac{k^2}{\varepsilon} \tag{3-4}$$

In this equation, C_μ is a constant and the values of k and ε are obtained by differential transport equations for the turbulence kinetic energy and the turbulence eddy dissipation.

k-equation:

$$\frac{\partial(\rho k)}{\partial t} + \frac{\partial}{\partial x_j}(\rho U_j k) = \frac{\partial}{\partial x_j}\left[(\mu + \frac{\mu_t}{\sigma_k})\frac{\partial k}{\partial x_j}\right] + P_k - \rho\varepsilon + P_{kb} \tag{3-5}$$

ε -equation:

$$\frac{\partial(\rho \varepsilon)}{\partial t} + \frac{\partial}{\partial x_j}(\rho U_j \varepsilon) = \frac{\partial}{\partial x_j}\left[(\mu + \frac{\mu_t}{\sigma_\varepsilon})\frac{\partial \varepsilon}{\partial x_j}\right] + \frac{\varepsilon}{k}(C_{\varepsilon 1}P_k - C_{\varepsilon 2}\rho\varepsilon + C_{\varepsilon 1}P_{\varepsilon b}) \tag{3-6}$$

Here $C_{\varepsilon 1}$, $C_{\varepsilon 2}$, σ_k and σ_ε are constants. P_{kb} and $P_{\varepsilon b}$ represent the influence of the buoyancy forces. P_k is the turbulence production due to viscous forces.

The $k-\varepsilon$ model requires the complex non-linear damping functions. Therefore, the performance of the near wall treatment for low-Reynolds number computations is

unsatisfactory. In order to modify this disadvantage, Wilcox [57] developed the $k-\omega$ model which assumes that the turbulence viscosity is linked to the turbulence kinetic energy (k) and turbulent frequency (ω). The relationship is shown below:

$$\mu_t = \rho \frac{k}{\omega} \tag{3-7}$$

Similar to the $k-\varepsilon$ model, the $k-\omega$ model solves two transport equations for turbulent kinetic energy and turbulent frequency.

k-equation:

$$\frac{\partial(\rho k)}{\partial t} + \frac{\partial}{\partial x_j}(\rho U_j k) = \frac{\partial}{\partial x_j}\left[(\mu + \frac{\mu_t}{\sigma_k})\frac{\partial k}{\partial x_j}\right] + P_k - \beta' \rho k\omega + P_{kb} \tag{3-8}$$

ω -equation:

$$\frac{\partial(\rho\omega)}{\partial t} + \frac{\partial}{\partial x_j}(\rho U_j \omega) = \frac{\partial}{\partial x_j}\left[(\mu + \frac{\mu_t}{\sigma_\omega})\frac{\partial \omega}{\partial x_j}\right] + \alpha\frac{\omega}{k}P_k - \beta\rho\omega^2 + P_{\omega b} \tag{3-9}$$

In these equations, the model constants are shown in Table 3.1.

α	β	β'	σ_k	σ_ω
5/9	0.075	0.09	2	2

Table 3-1 The Wilcox $k-\omega$ model constants

The main disadvantage of the Wilcox $k-\omega$ model is it has strong sensitivity to free-stream conditions. For example, the different value of ω at the inlet can lead to great variation in the results. In order to solve this problem, a modified $k-\omega$ model was developed by Menter [58]. The new model blends the $k-\omega$ model near the wall region and the $k-\varepsilon$ model in the outer region. At the same time, the shear stress transport (SST) formulation combines two parts of the model and, hence, the new model is called the SST $k-\omega$ model. The SST $k-\omega$ model gives highly accurate predictions of the onset and the amount of flow separation under adverse pressure gradient. The turbulence viscosity in this model is modified by:

$$\mu_t = \rho \frac{\alpha_1 k}{\max(\alpha_1 \omega, SF_2)} \tag{3-10}$$

The two transport equations are transformed to:

k-equation:

$$\frac{\partial(\rho k)}{\partial t} + \frac{\partial}{\partial x_j}(\rho U_j k) = \frac{\partial}{\partial x_j}\left[(\mu + \frac{\mu_t}{\sigma_{k3}})\frac{\partial k}{\partial x_j}\right] + P_k - \beta' \rho k\omega + P_{kb} \tag{3-11}$$

ω -equation:

$$\frac{\partial(\rho\omega)}{\partial t} + \frac{\partial}{\partial x_j}(\rho U_j \omega) = \frac{\partial}{\partial x_j}\left[(\mu + \frac{\mu_t}{\sigma_{\omega 3}})\frac{\partial \omega}{\partial x_j}\right] + (1 - F_1)2\rho \frac{1}{\sigma_{\omega 2}\omega}\frac{\partial k}{\partial x_j}\frac{\partial \omega}{\partial x_j} + \alpha_3 \frac{\omega}{k} P_k - \beta_3 \rho \omega^2 + P_{\omega b} \tag{3-12}$$

Here F_1 and F_2 are blending functions. F_1 is a function of the wall distance, which is equal to one near the surface and zero outside the boundary layer. F_2 restricts the limiter to the wall boundary. These blending functions are critical to the SST $k-\omega$ model and their formulations are based on the distance to the nearest wall and on the flow variables. In equation (3-10), S is an invariant measure of the strain rate.

In short, the SST $k-\omega$ model is more suitable for high accuracy boundary layer simulations. If no other description is given, the SST $k-\omega$ model is adopted for all computations in this thesis.

3.2. **Heat transfer**

Heat transfer models are used to compute the temperature throughout the flow. The effects of conduction, convection, turbulent mixing and viscous work are considered in the heat transfer model. In this thesis, the total energy model in ANSYS-CFX is adopted for all computations. This model includes the transport of enthalpy and

kinetic energy effects. Therefore, the total energy model has better performance than other heat transfer models when kinetic energy effect is not neglected. The equations for this heat transfer model also come from the help files from ANSYS-CFX Version 13.0. The total energy equation is shown below:

$$\frac{\partial(\rho h_{tot})}{\partial t} - \frac{\partial p}{\partial t} + \nabla \cdot (\rho U h_{tot}) = \nabla \cdot (\lambda \nabla T) + \nabla \cdot (U \cdot \tau) + U \cdot S_M + S_E \qquad (3\text{-}13)$$

Here S_E is the energy source and h_{tot} is the total enthalpy, which linked to the static enthalpy $h(T, p)$ by:

$$h_{tot} = h + \frac{1}{2}U^2 \qquad (3\text{-}14)$$

The term $\nabla \cdot (U \cdot \tau)$ represents the work due to viscous stresses and is called the viscous work term. The term $U \cdot S_M$ represents the work due to external momentum sources and is neglected.

The heat flux at the wall can be modelled using the thermal law-of-the-wall function of Kader [59]. The wall heat flux is calculated using the relationship shown below:

$$q_w = \frac{\rho c_p u^*}{T^+}(T_w - T_f) \qquad (3\text{-}15)$$

Here T_w is the temperature at the wall, T_f is the near-wall fluid temperature and c_p is the fluid heat capacity. According to equation 3-15, if the wall temperature is given as boundary condition, then the wall heat flux can be computed. The non-dimensional temperature (T^+) is modelled by blending the viscous sub-layer and logarithmic law of the wall.

$$T^+ = \mathrm{Pr}\, y^* e^{(-\Gamma)} + [2.12 \ln(y^*) + (3.85\,\mathrm{Pr}^{1/3} - 1.3)^2 + 2.12 \ln(\mathrm{Pr})] e^{(-1/\Gamma)} \qquad (3\text{-}16)$$

Here Pr is the fluid Prandtl number and Γ is given by:

$$\Gamma = \frac{0.01(\mathrm{Pr}\, y^*)^4}{1+5\mathrm{Pr}^3\, y^*} \tag{3-17}$$

The Nusselt number (Nu) is the dimensionless heat transfer and the general definition is shown below. At a boundary within a fluid, this number represents the ratio of convective to conductive heat transfer across the boundary. The specific definition for Nusselt number in rotor-stator systems is discussed in the literatures. In the next chapter, two definitions are given and compared.

$$Nu = \frac{hr}{k} \tag{3-18}$$

3.3. **Other computational settings and parameters**

For all computations in this thesis, the ideal gas is used for fluid properties and consequently density is computed using the ideal gas law. A high resolution setting is applied for the advection scheme and an average ambient (atmospheric) pressure condition is applied at the outlet boundary. In order to compute the sealing effectiveness, the concentration is introduced into computations as an additional variable. This additional variable (φ) is solved by the transport equation in ANSYS-CFX Version 13.0:

$$\frac{\partial(\rho\varphi)}{\partial t} + \nabla\cdot(\rho U\varphi) = \nabla\cdot\left((\rho D_{\Phi} + \frac{\mu_t}{Sc_t})\nabla\varphi\right) + S_{\varphi} \tag{3-19}$$

Here, D_{Φ}, the kinematic diffusivity, is $1.6\times10^{-5}\,\mathrm{m}^2/s$ for this additional variable (concentration).

The definition of concentration effectiveness ε_c is used:

$$\varepsilon_c = \frac{c - c_a}{c_o - c_a} \tag{3-20}$$

Here the subscripts a and o refer to the air in the annulus and sealing flow at inlet to the system respectively.

In the computations, three computational parameters are used to present the sealing flow. The first parameter is the non-dimensional sealing flow rate $C_{w,o}(=\dot{m}_o/\mu b)$. The non-dimensional sealing parameter $\Phi_o(=C_{w,o}/2\pi G_c \mathrm{Re}_\phi)$ is the second parameter. These two parameters are mainly used for the computation of sealing effectiveness. The last parameter is the turbulent flow parameter: $\lambda_T(=C_{w,o}\,\mathrm{Re}_\phi^{-0.8})$, which governs the fluid structure and heat transfer in the wheel-space.

3.4. **3D Computations for the 'thin seal' model**

Early in this investigation 3D computations were carried out as a preliminary study for ingress problem. The 3D 'thin seal' model used here is a version of the model developed and tested by Owen *et al.* [49, 56]. A schematic diagram and computational mesh of the 3D model, illustrated in Figure 3-1, shows a rotor-stator wheel-space with an outer radius b = 0.195m, an axial-clearance rim seal and the generic vane used in the Bath experimental rig. The 'thin seal' means the radial dimension of the seal is made as thin as permitted by meshing consideration. This 'thin seal' approximation can help prevent the formation of a vortex inside the seal clearance, which would inhibit the ingested flow into the wheel-space. The 3D model is an 11.25° sector model with approximately 1.7 million cells, incorporating one vane pitch. The outer annulus represents the mainstream gas path through the turbine stage. The system has two inlets: the sealing air inlet at the inner radius of the wheel-space and the external mainstream inlet upstream of the vane.

The model has been run at a rotational Reynolds number $\mathrm{Re}_\phi = 7.8\times10^5$ and at

three non-dimensional sealing flow rates $C_{w,o}$. The detailed computational parameters are shown in Table 3-2. In addition to the momentum and energy equations, a further transport equation was solved for conservation of a non-interacting scalar, which allowed a tracer to be introduced at the mainstream inlet in order to calculate the amount of ingress and hence sealing effectiveness.

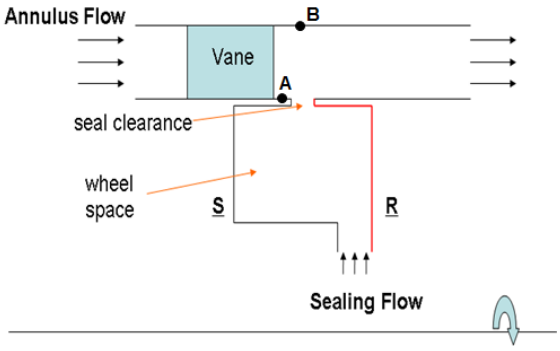

(a)

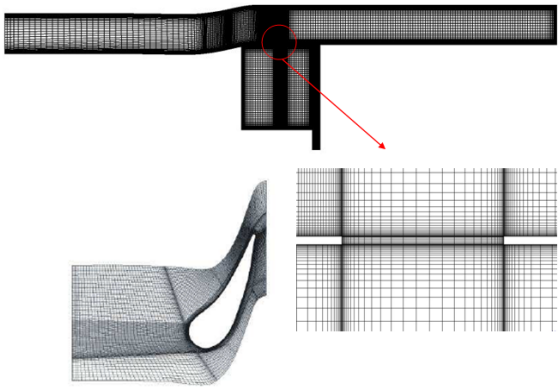

(b)

Figure 3-1 (a) Schematic diagram of 3D thin-seal model (b) Computational mesh [49]

Re_ϕ	Re_w	G_c
7.8×10^5	4.3×10^5	0.01

$\dot{m}_o/\dot{m}_a$	$C_{w,o}$	Φ_o
2%	2.8×10^3	0.061
4%	5.6×10^3	0.122
12%	16.8×10^3	0.366

Table 3-2 Computational parameters for 3D computations

The pressure difference in the annulus is the principal driving mechanism for externally-induced ingress. The pressure coefficients (C_p) in the annulus is computed at two locations: on the stator hub, half way between the vane trailing edge and the stator-side of the seal (location A); and on the annulus wall radially outward of the axial centre of the seal clearance (Location B). These two locations are illustrated in Fig 3-1 (a). The definition of C_p is shown here:

$$C_p = \frac{p - \bar{p}}{1/2\rho\Omega^2 b^2} \tag{3-21}$$

Here $\bar{p}$ is the average static pressure along one vane pitch. Figure 3-2 show the computed circumferential distribution of C_p at two locations for three different values of Φ_o. The figures display that the maximum value and the magnitude of the variation form peak to trough are reduced by increasing Φ_o, the sealing flow rate. The magnitude of the variation at Location B is smaller than that at Location A. However, the circumferential locations of the maximum and minimum values are almost the same at Location A and B. These results show that the two locations give a qualitatively similar pressure variation contributing to ingestion. The sealing flow can decrease the magnitude of the pressure variation and consequently reduce the ingress.

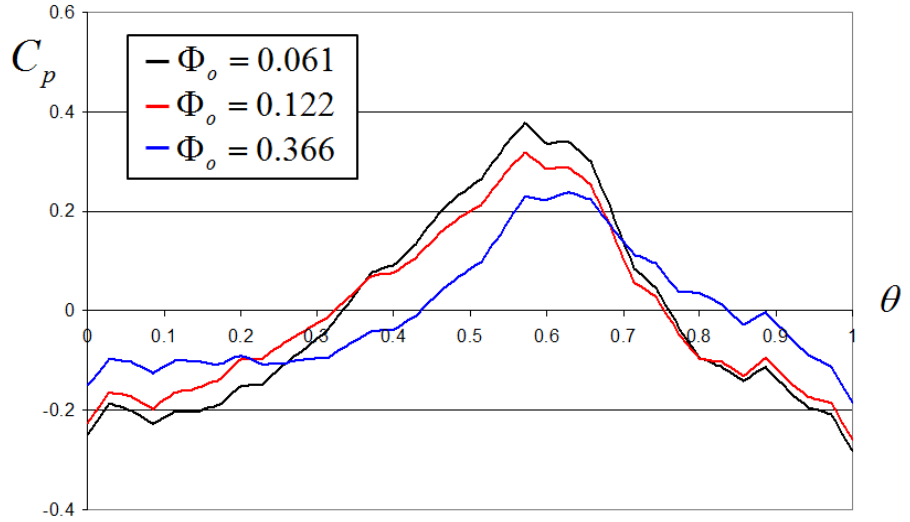

(a) Location A

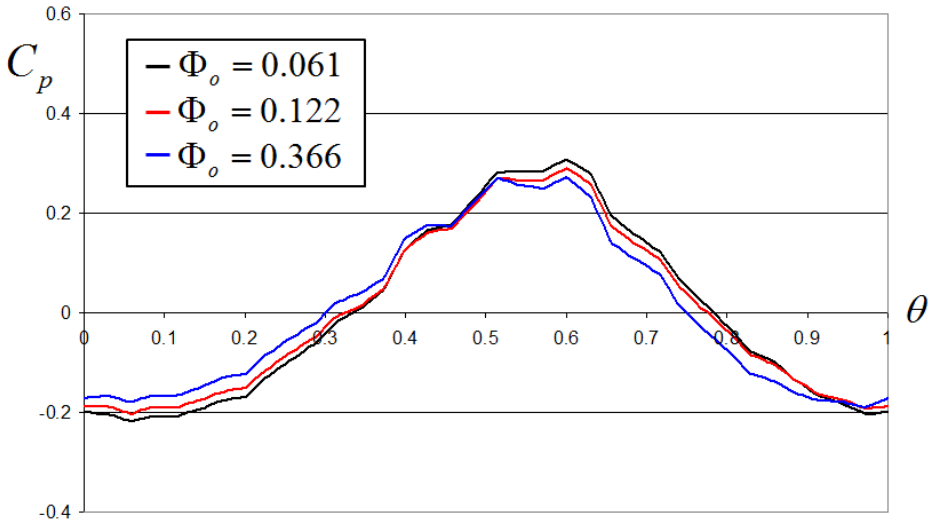

(b) Location B

Figure 3-2 Computed circumferential distributions of C_p

Figure 3-3 shows the streamlines with effectiveness in the $r-\theta$ plane at $z/s = 0.5$ (axial centre plane of the seal clearance). When Φ_o is small (0.061), the annulus flow is seen to enter the wheel-space through the seal clearance. Due to the mixing between the ingested flow and the sealing flow, the effectiveness in that ingested region is around 0.25. Increasing the sealing flow to Φ_o=0.122, the wheel-space is almost sealed.

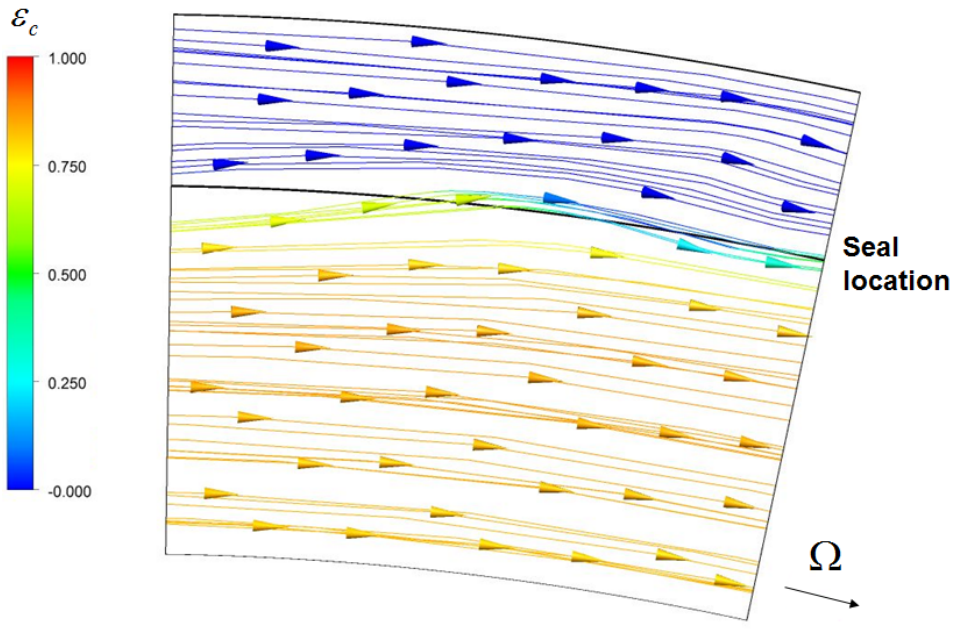

Φ_o =0.061

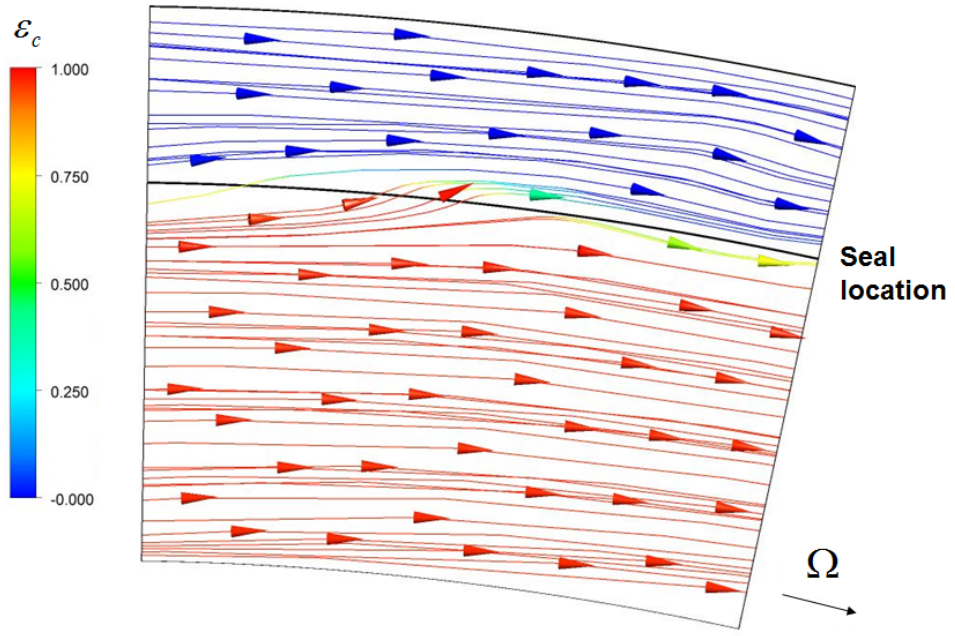

Φ_o =0.122

Figure 3-3 Streamlines with effectiveness in the $r-\theta$ plane at $z/s=0.5$

The computed variation of effectiveness in the wheel-space ($r/b=0.958$) with Φ_o is shown in Figure 3-4. In the figure, the theoretical curve [51] was fitted to the experimental data using the statistical technique of Zhou *et al.* [53]. The figure shows that although the computed effectiveness increases as Φ_o increases, the computed values over-predict the experimental data. This result indicates the 3D 'thin seal'

model would under-predict the ingress level. Some unsteady flow behaviours maybe contribute to this under-predict.

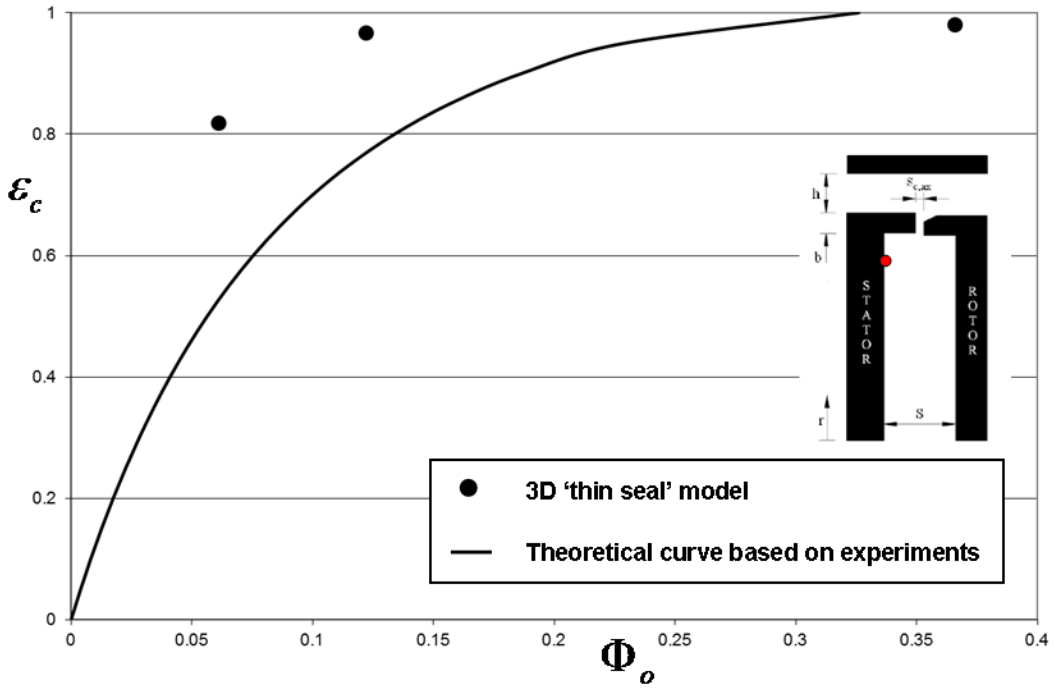

Figure 3-4 Variation of computed effectiveness with Φ_o

3.5. **Chapter summary**

In this chapter, a brief introduction to the turbulence model and methods of heat transfer calculation in ANSYS-CFX is given. Computational results from 3D steady computations are presented using a "thin seal" model. This model provided a qualitative description of ingress but under-predicted the levels. Moreover, this 3D thin-seal model was computational expensive with about 72 hours for each computation (using a single 2.8GHz processor). A simpler, more rapid model called "prescribed ingestion" will be presented in this thesis. Rotor-stator system models without ingress are studied in Chapter 4. Subsequently, Chapter 5 and 6 give detailed information from the prescribed ingestion model.

4. Axisymmetric rotor-stator models

The axisymmetric rotor-stator model represents the wheel-space between the rotor and stator discs. In this chapter, the computational results from 2D rotor-stator models with no ingress will be compared with the published experimental data in Chen *et al.* [8]. For fluid dynamics, the velocity profiles in the wheel-space are computed and the effects of boundary conditions are presented. For heat transfer, the Nusselt number on the rotor is calculated, and the influence of thermal boundary conditions and the turbulence model are investigated. Results for two different configurations are also compared in order to study the effect of wheel-space geometry on the fluid dynamics and heat transfer. Generally, the computational results show good agreement with experimental data, validating the axisymmetric CFX rotor-stator model for prediction of the fluid dynamic and heat transfer in the wheel-space.

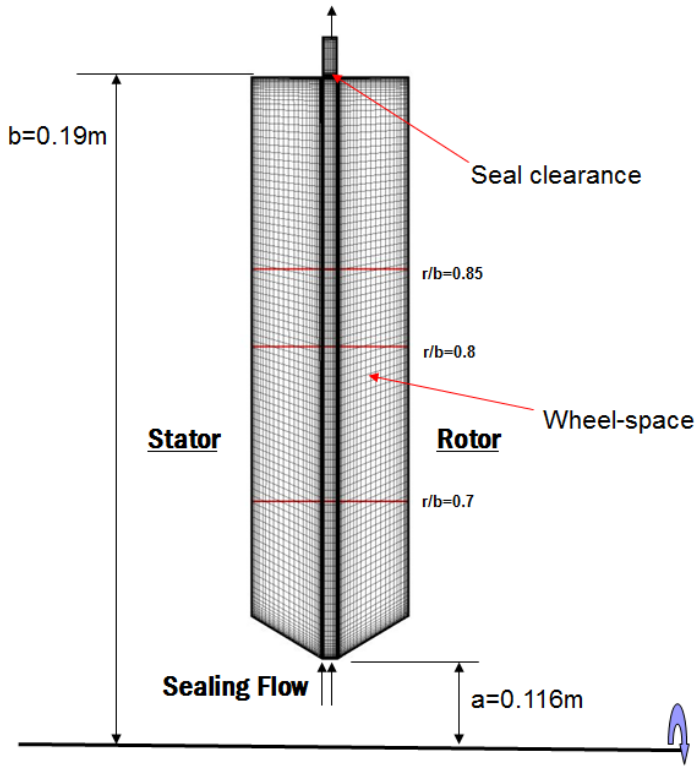

Figure 4-1 The Bath Rig Model

The geometries for the axisymmetric rotor-stator wheel-space models used in this chapter are shown in Figures 4-1 and 4-2. The first one, Figure 4-1, is called the Bath Rig Model, based on the experimental test rig used for ingress experiments at the

University of Bath. This model has a radial inlet for supposed (sealing) flow and sloping surfaces near the inlet at $a = r/b = 0.61$. The geometry of the second model, Figure 4-2, is identical to that of the experimental rotor-stator rig used by Chen *et al.* [8]. Hence, this model is called the Chen Rig Model. An axial sealing flow inlet is located at the axis of rotation. The Bath Rig Model contains around 16000 mesh cells and the Chen Rig Model around 77000 cells. All computations in this chapter are carried out at $\mathrm{Re}_\phi = 1.25\times10^6$ for four different values of sealing flow rate that are the same as those in Chen *et al.* [8].

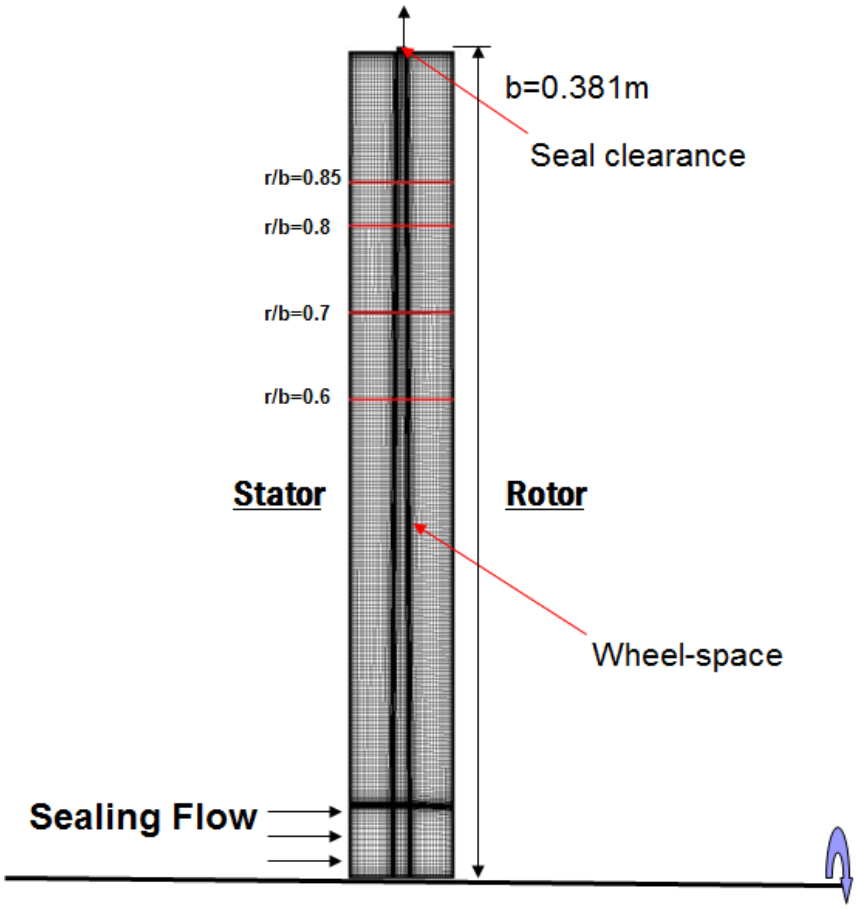

Figure 4-2 The Chen Rig Model

4.1. Fluid dynamics for the axisymmetric rotor-stator model

To understand the fluid dynamics in the wheel-space, velocity profiles are presented for the Bath Rig Model and Chen Rig Model. Figure 4-3 shows computed velocity

distributions for both the Chen Rig and the Bath Rig Models compared with the experimental data of Chen *et al.* [8] for λ_T = 0.081 (no results for the Bath Rig Model are shown at $x = 0.6$ as this is inward of the location of the inlet for the Bath testing rig geometry). The measured distributions of non-dimensional radial and circumferential velocities reported by Chen *et al.* [8] at the four radial locations, shown in Figure 4-2 $0.6 \leq x = r/b \leq 0.85$, are also presented. The abscissa in the figure represents the non-dimensional axial location, where the stator is at $z/s = 0$ and $z/s = 1$ is the rotor wall.

Generally, both sets computed results show reasonably good agreement with the experimental data and with each other, even though the geometry of the two wheel-spaces is different. The results for radial velocity show the typical rotor-stator flow behaviour, with flow radially outward on the rotor ($z/s = 1$), radially inward on the stator ($z/s = 0$) and almost no radial flow in the middle of wheel-space. For radial velocity distribution at $x = 0.7$, the computed result from Chen Rig Model has more similarity with the experimental data than Bath Rig Model. This illustrates that the flow at low radius in the Bath Rig Model is influenced by the details of the wheel-space geometry near the inlet. The difference between two models reduces with increasing non-dimensional radius x. At low radius ($x = 0.6$), the computed velocities tend to underestimate the inflow on the stator; consequently, the outflow on the rotor is overestimated. The difference also reduces with increasing x. These results illustrate that the flow in the source region is strongly influenced by inlet conditions. For the non-dimensional circumferential velocity (swirl ratio), there is very little effect of geometry and both models give good agreement with the experimental data. There is a core of nearly constant swirl ratio fluid between the separate boundary layer on the rotor and stator at each radial location and the core swirl ratio increases as x increases.

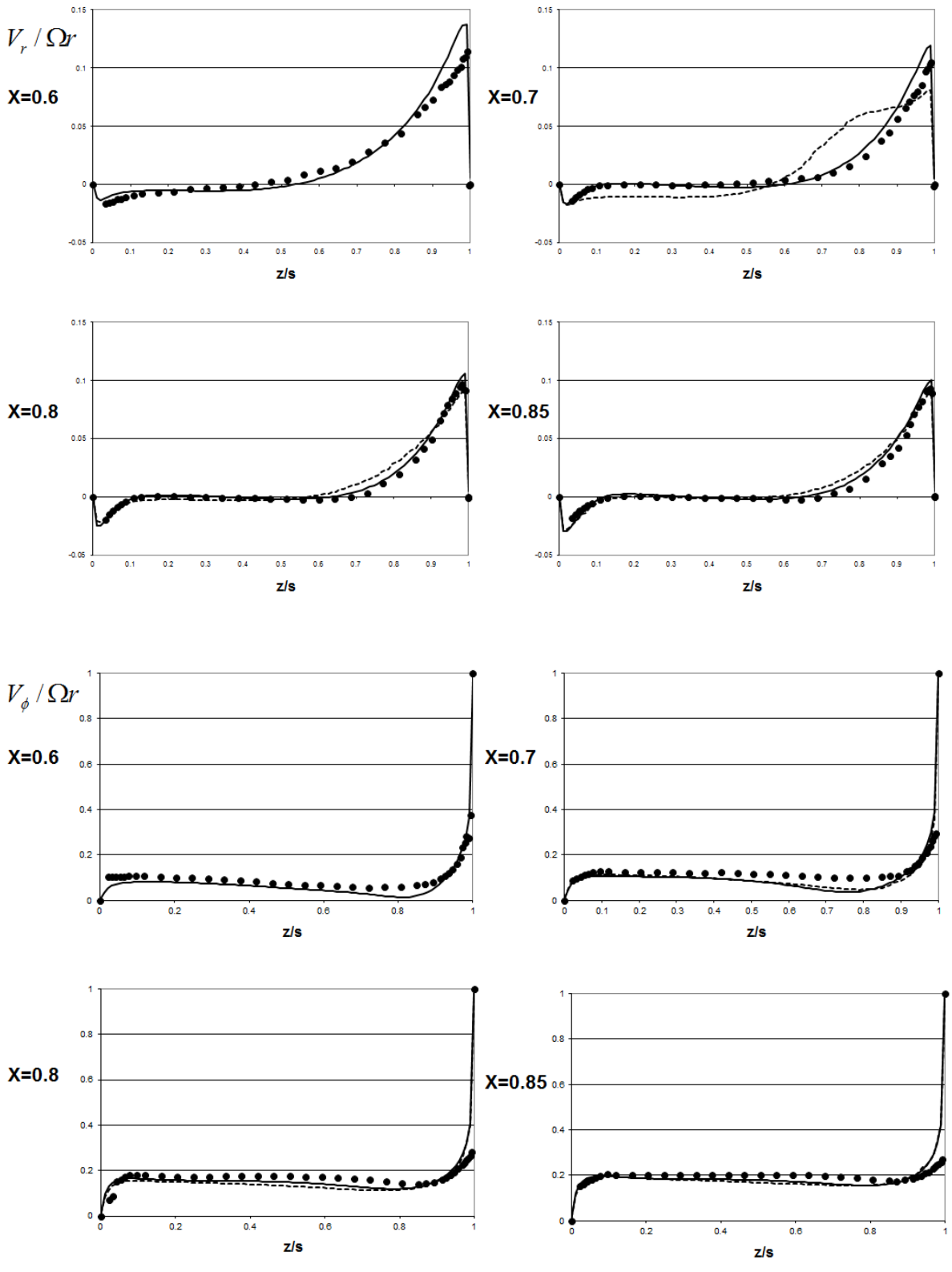

Figure 4-3 Computed velocity profiles from Chen and Bath Rig Model compared with measured data, $\lambda_T = 0.081$

The computations in Figure 4-3 use a zero-average inlet swirl ratio ($\overline{\beta}_{in} = 0$) and an adiabatic rotor wall as boundary conditions. Two further computations were carried out in order to investigate the influence of boundary conditions on the velocity profiles for the Bath Rig Model. The first computation uses a non-zero average inlet swirl ratio ($\overline{\beta}_{in} = 0.25$ from the literature [56]) and an adiabatic rotor wall. In the second computation, as the ideal gas law is used to compute density, a fixed rotor temperature equal to 355K ($T_{rotor} = 355K$) was used to study the influence of thermal condition on the fluid dynamics. A zero-average inlet swirl ratio was also applied in this computation.

The computed distributions for the radial and circumferential (tangential) components of velocity obtained for $C_{w,o} = 6100$ at the three different non-dimensional radial locations (x=0.7, 0.8 and 0.85) are shown in Figure 4-4. The experimental data of Chen *et al.* [8] are also included. For radial velocity, the differences between the computed and measured values mainly appear at low radius (x=0.7), which illustrates that the flow at low radius is influenced by the swirl ratio at inlet. Other than in the inlet region, there is not much difference between all three computed results, especially at high radial locations. For circumferential velocity, the computation with non-zero inlet swirl ratio gives a higher value for the core rotation than in the experiment (in the experiment of Chen *et al.* [8], there was no swirl at inlet), and the two zero-swirl cases give a closer result, though slightly under predicting the experimental data. This shows that the inlet swirl increases the swirl in the wheel-space. The thermal condition on the rotor surface has negligible effect on either radial or circumferential velocity distributions.

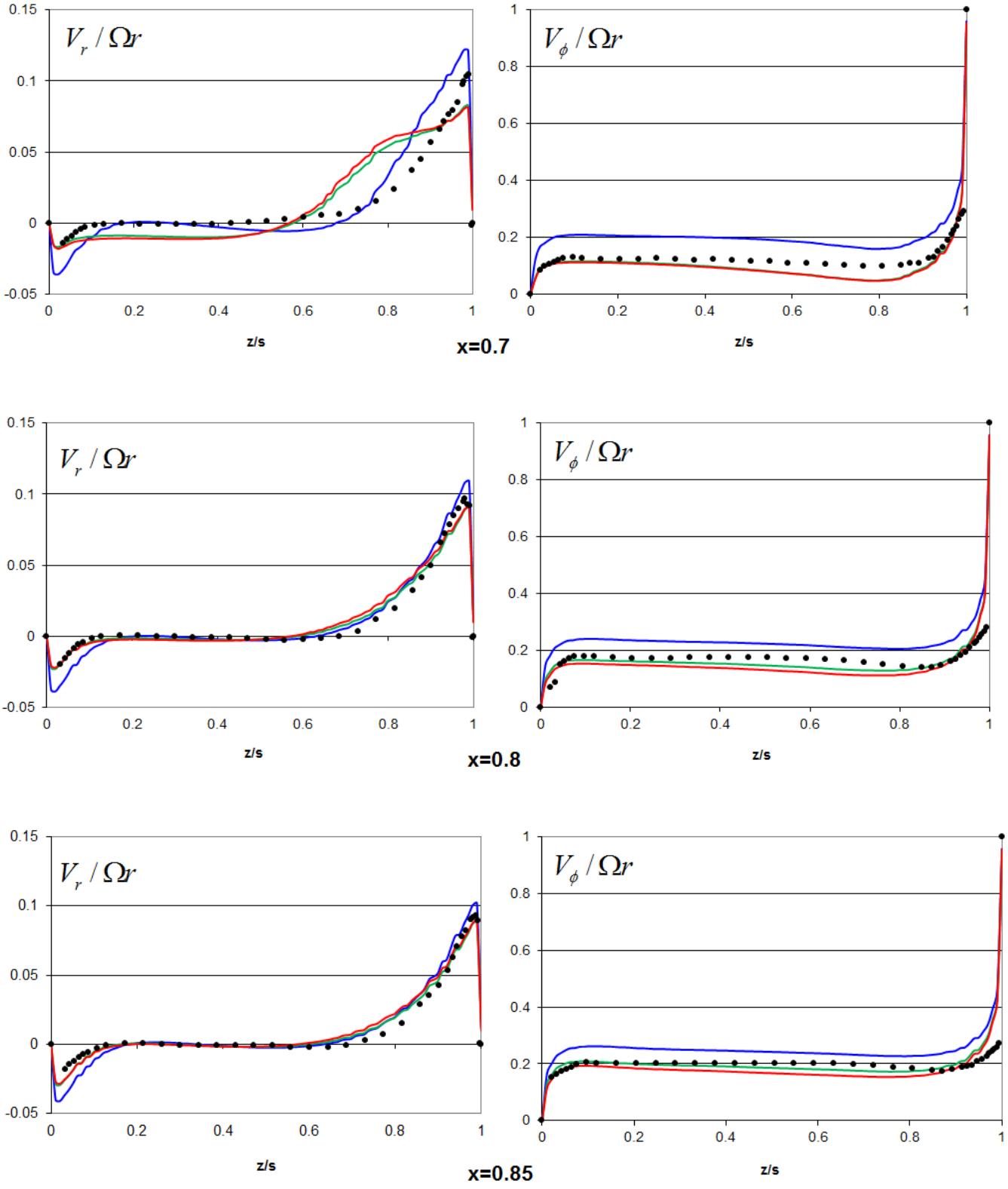

Figure 4-4 Computed and measured velocity profiles for the Bath Rig Model, $\lambda_T = 0.081$

For consistency with the experiment and for convenience for heat transfer computations, the third boundary condition ($\bar{\beta}_{in} = 0$, $T_{rotor} = 355K$) is used subsequently, and the effect of sealing flow rate on velocity distributions is investigated. The turbulent flow parameter, $\lambda_T = C_{w,o}\,\mathrm{Re}_\phi^{-0.8}$, is used to represent the sealing flow rate. Four sealing flow rates are selected with λ_T varying from 0.034 to 0.128. Figure 4-5 shows the computed radial and circumferential velocity distributions at x=0.8 for the four values of λ_T. The magnitude of the outward radial velocity near the rotor increases and the inward radial velocity near the stator decreases as λ_T increases. For non-dimensional circumferential velocity, the magnitude of $V_\phi / \Omega r$ in the core falls with increasing λ_T, illustrating that the higher flow rates of zero-swirl sealing flow reduces the core rotation.

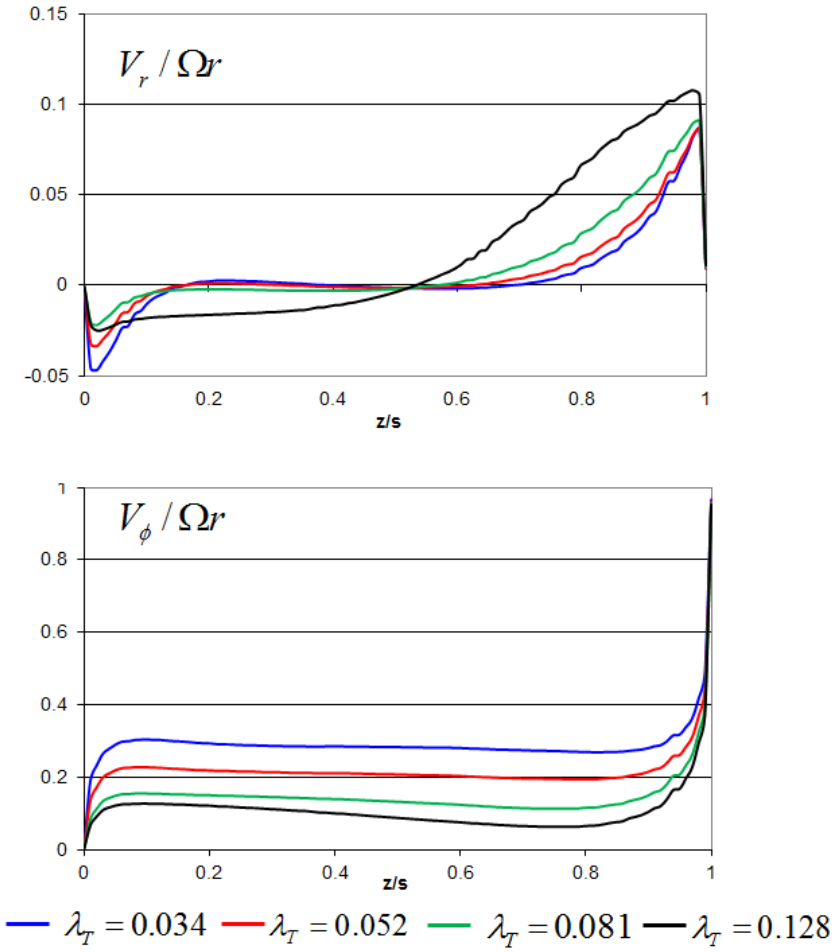

Figure 4-5 Computed velocity profiles with different λ_T for the Bath Rig Model

The computed secondary flow streamlines for the two highest λ_T cases, shown in Figure 4-6, further illustrate the typical rotor-stator flow behaviour as discussed for Figure 4-4 and 4-5. The streamlines contours illustrate that a secondary flow recirculation occurs at low radius near the rotor, due to the sloping geometry for the Bath Rig Model in that area, which further explains the differences between computed and measured radial velocity distribution at low radius in Figure 4-4. This recirculation region becomes larger with increasing λ_T .

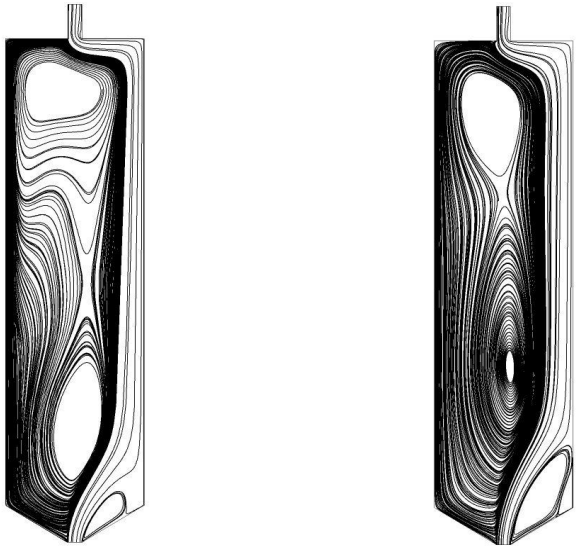

$\lambda_T = 0.081$ $\lambda_T = 0.128$

Figure 4-6 The streamlines in whole cavity for two high sealing flow rate cases

4.2. **Heat transfer for the axisymmetric rotor-stator model**

To investigate the heat transfer on the rotor, the Nusselt number, the ratio of convective to conductive heat transfer normal to the boundary, is calculated. Owen and Rogers [10] showed that Nu is proportional to $\mathrm{Re}_\phi^{0.8}$ for turbulent boundary-layer flow in rotor-stator systems; consequently the parameter $Nu\,\mathrm{Re}_\phi^{-0.8}$ is independent of Re_ϕ. Lewis *et al.* [17] also mention that $Nu\,\mathrm{Re}_\phi^{-0.8}$ is a correlating parameter in rotor-stator systems. Therefore, this parameter is adopted in this thesis.

The definition of Nusselt number in Lewis *et al.* was given by:

$$T_{w,ad} = T_{o,1} - \frac{V_{\phi,\infty}^2}{2c_p} + R\frac{\Omega^2 r^2}{2c_p}(1 - \frac{V_{\phi,\infty}}{\Omega r})^2 \quad \text{(eq.4-1)}$$

$$Nu = \frac{qr}{k(T_w - T_{w,ad})} \quad \text{(eq.4-2)}$$

Where $V_{\phi,\infty}$ is the circumferential velocity in the core, c_p is the specific heat at constant pressure and k is the thermal conductivity of air. Chen *et al.* [8] used a different definition for Nu, as shown below.

$$T_{ref} = T_1 + R\frac{\Omega^2 r^2}{2c_p} \quad (4\text{-}3)$$

$$Nu = \frac{qr}{k(T_w - T_{ref})} \quad (4\text{-}4)$$

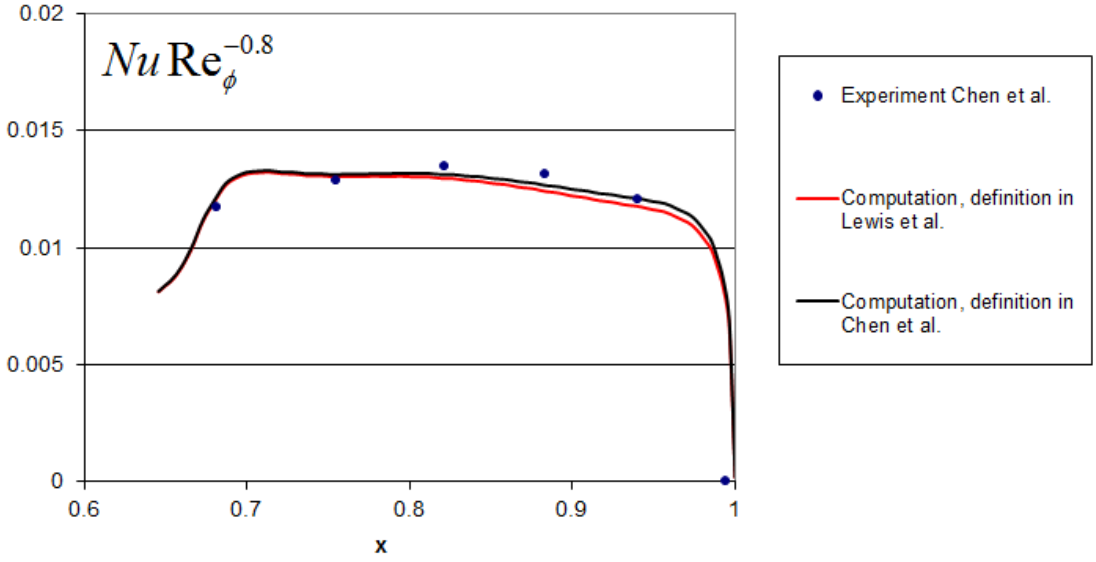

Figure 4-7 Comparison between definitions for Nu, $\lambda_T = 0.081$

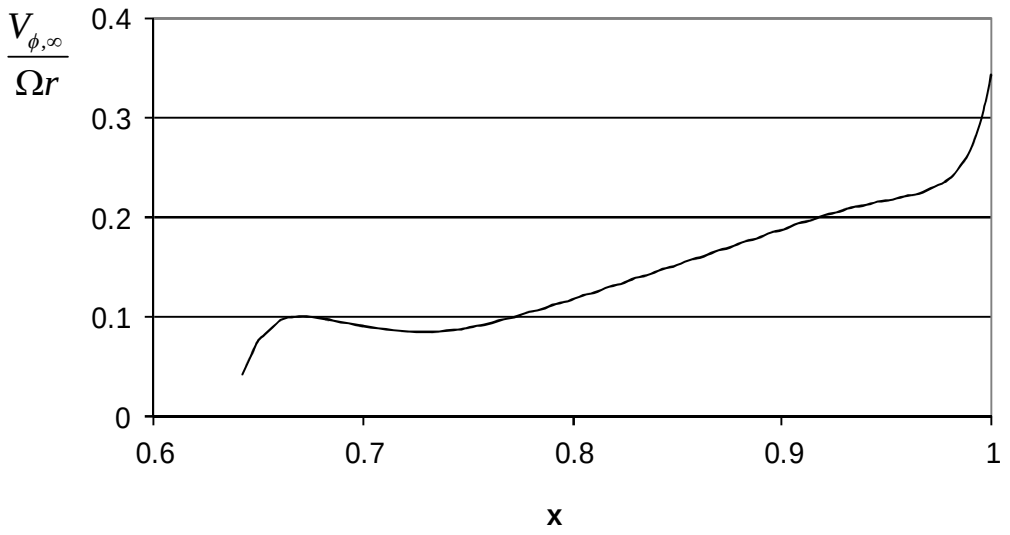

Figure 4-8 The swirl ratio at middle plane between the rotor and the stator, $\lambda_T = 0.081$

The main difference between the definitions is that Lewis *et al.* [17] introduces the effect of the core swirl ratio into the definition. Figure 4-7 shows the comparison between results using the two definitions of Nu for the radial variation of $Nu\,\mathrm{Re}_\phi^{-0.8}$ for the Bath Rig Model when the turbulent flow parameter is equal to 0.081. The two definitions give similar results and there is good agreement with the measurements of Chen *et al.*. At high radius, the definition used by Chen *et al.* gives a slightly higher value than that used by Lewis *et al*. The swirl ratio ($V_{\phi,\infty}/\Omega r$) at the mid-plane between the rotor and the stator ($z/s = 0.5$) is the determining factor for the difference. The computed variation of swirl ratio is shown in Figure 4-8. At low radius, the difference between the two definitions of Nu is small due to the relatively small value of $V_{\phi,\infty}/\Omega r$. As radius increases, $V_{\phi,\infty}/\Omega r$ increases and the difference is visible in Figure 4-7. The definition used by Chen *et al.* will be adopted here for consistency with the Chen *et al.* experimental data.

The effect of λ_T on the radial distribution of $Nu\,\mathrm{Re}_\phi^{-0.8}$ is shown in Figure 4-9. The measurements made by Chen *et al.* for x>0.6 in their rig are also shown. Both the experimental data and the computed results indicate that $Nu\,\mathrm{Re}_\phi^{-0.8}$ increases as λ_T increases. The agreement between computations and measurements is poor at low values of λ_T. This is mainly due to low levels of computed turbulence in the

computations using SST $k-\omega$ turbulence model at these conditions ($\mathrm{Re}_\phi = 1.25\times10^6$). However, the agreement at high λ_T is satisfactory. Some simulations are carried out for trying to improve the agreement at low λ_T condition in this and next sections.

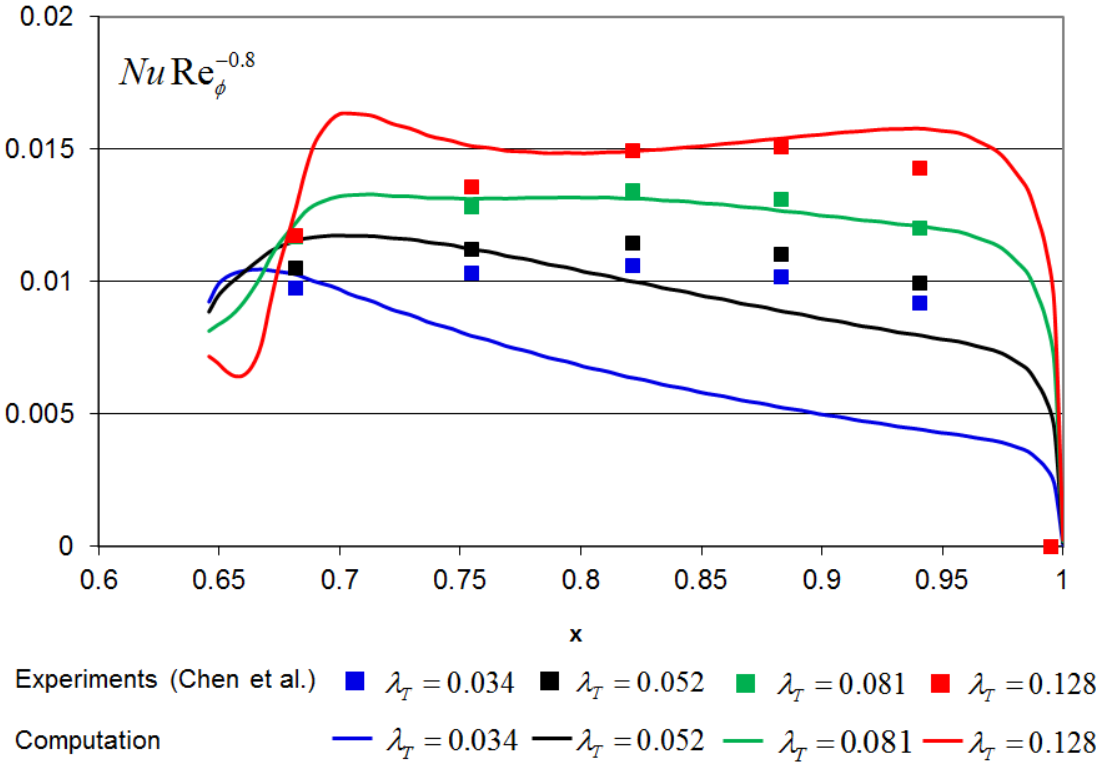

Figure 4-9 Radial distribution of $Nu\,\mathrm{Re}_\phi^{-0.8}$ for different λ_T

In the above computations, the rotor surface is set to a uniform constant temperature (355K), which is not the same as in the experiments. As shown in Figure 4-10, a part of measured temperatures from Chen *et al.* [8] were fitted using a 4th degree polynomial for the smallest and largest λ_T cases, and the effect of the using these fitted temperature conditions was investigated. Figure 4-11 illustrates the results for both cases. The results show almost no difference at high λ_T. There is a slight improvement at low λ_T, but the agreement with experiment remains poor. It is concluded from Figure 4-11 that the temperature at the rotor surface weakly affects the level of $Nu\,\mathrm{Re}_\phi^{-0.8}$, but that there is no significant effect on the distribution.

$(a)\lambda_T = 0.034$

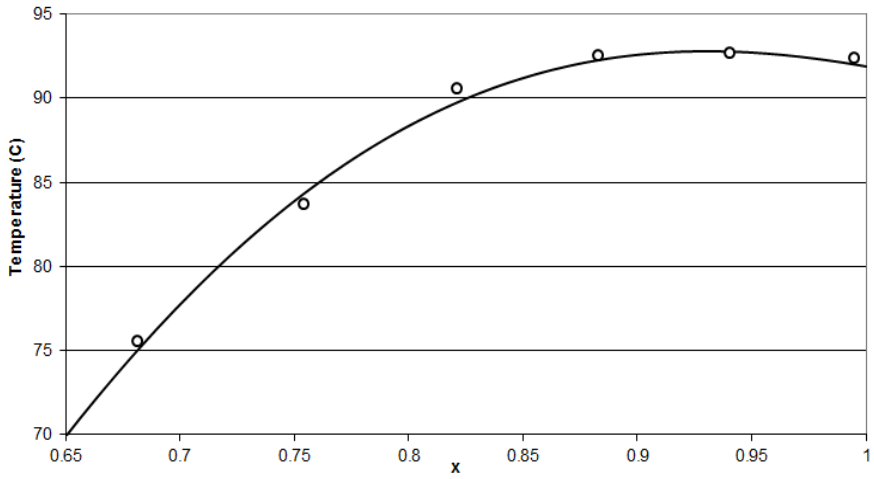

$(b)\lambda_T = 0.128$

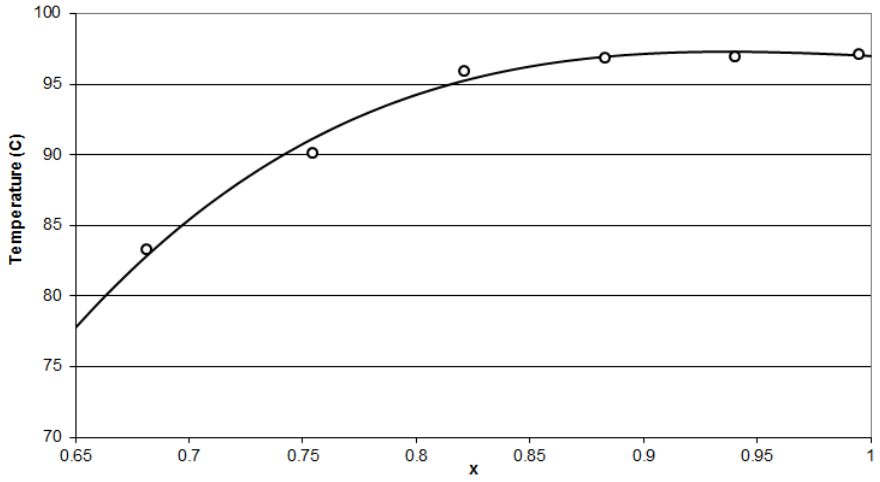

○ **Measured rotor temperature (Chen et al.)** — **Fitted rotor temperature**

Figure 4-10 Radial distribution of temperature on the rotor surface for the Bath Rig Model

$(a)\lambda_T = 0.034$

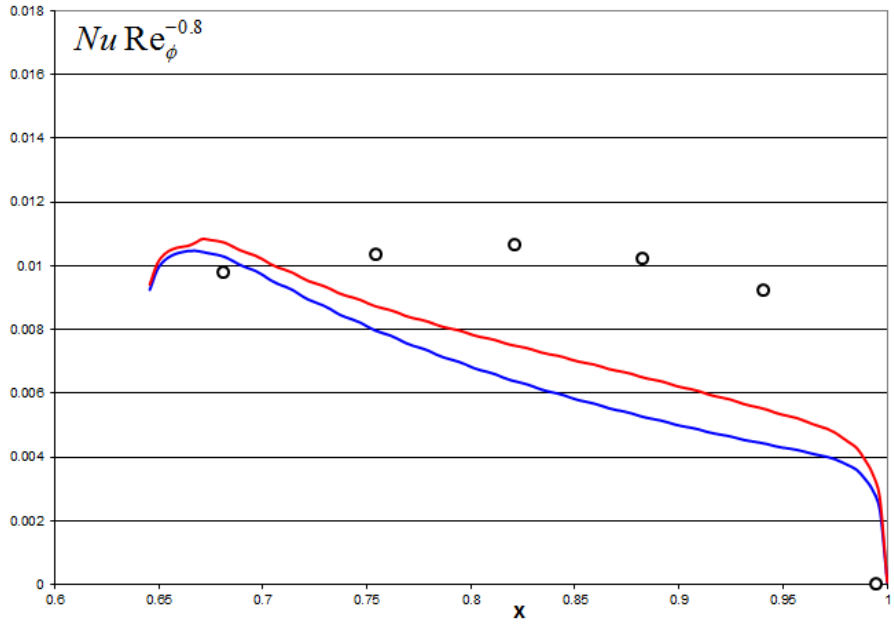

$(b)\lambda_T = 0.128$

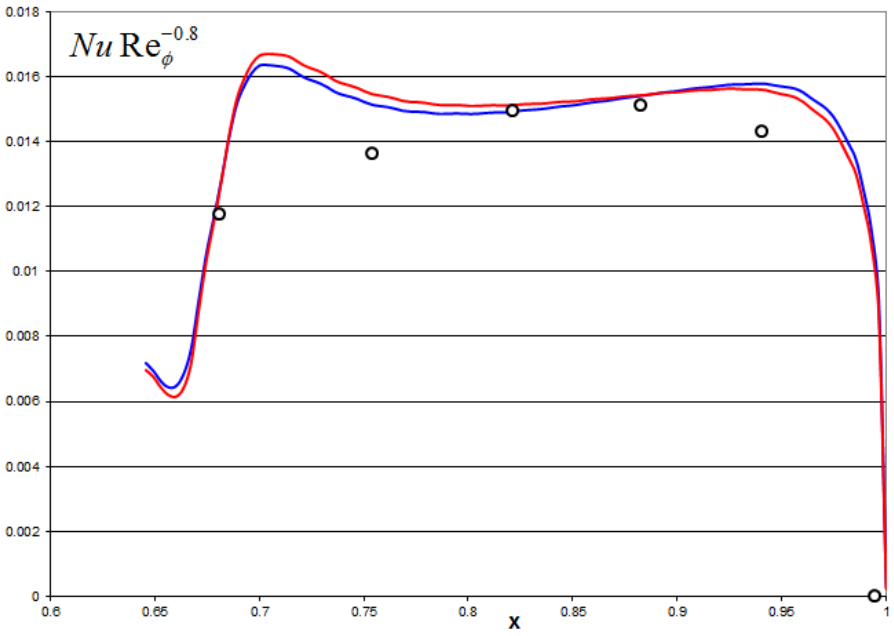

○ **Experiment Chen *et al.*** — **Computation, Fixed rotor temperature** — **Computation, Fitted rotor temperature**

Figure 4-11 The effect of thermal condition at rotor surface on the radial distribution of $Nu\,\mathrm{Re}_\phi^{-0.8}$

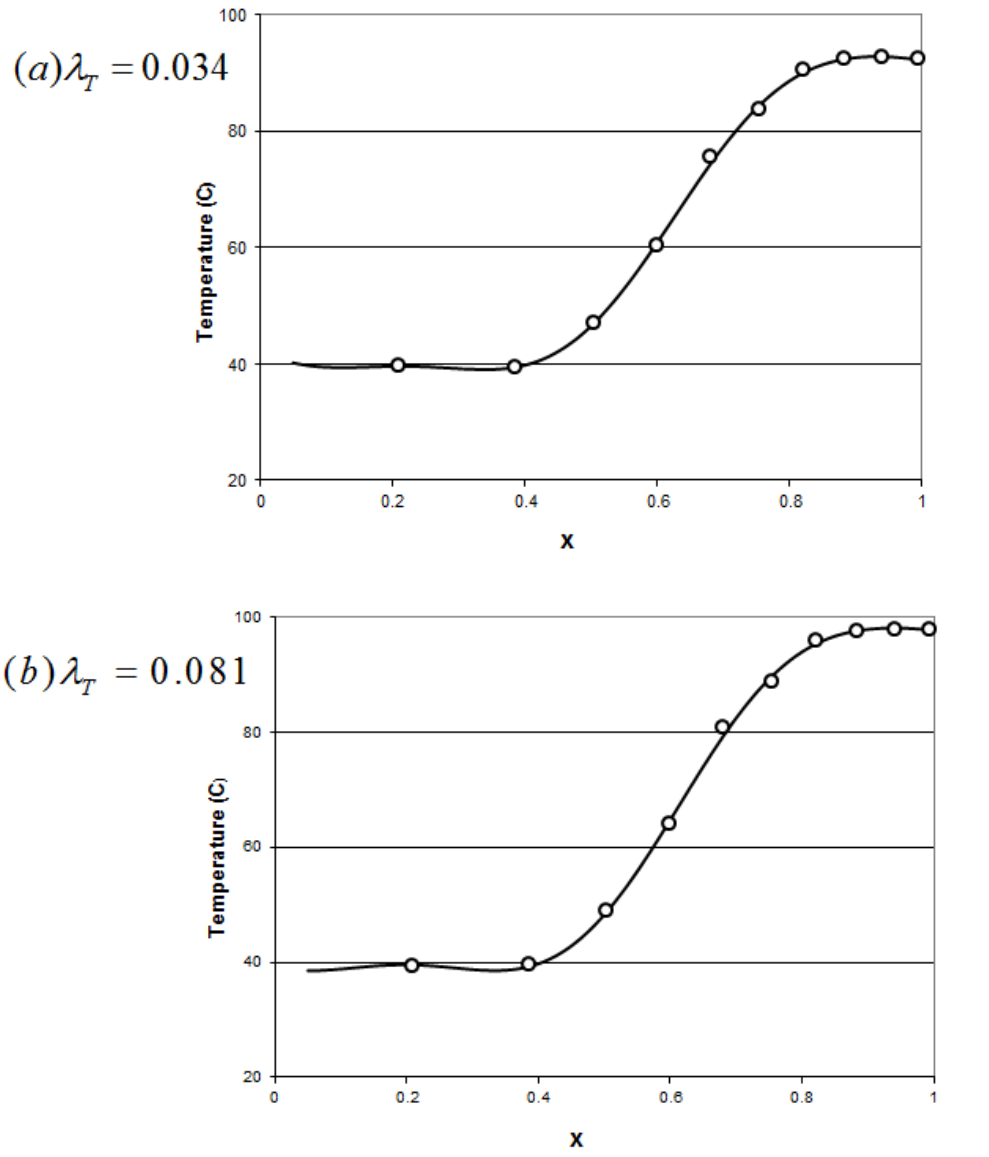

Figure 4-12 Radial distribution of temperature on the rotor surface for the Chen Rig Model

The effect of geometry on the heat transfer in the system was studied by compare previous results with the Chen Rig Model for λ_T = 0.034 and 0.081. The fit to the measured temperature distribution was applied for consistency with the experimental data. The wheel-space for the Chen Rig Model is large and hence the more measured temperature points are available and have been used. Therefore, a different function, sum of sine, is applied, as shown in Figure 4-12.

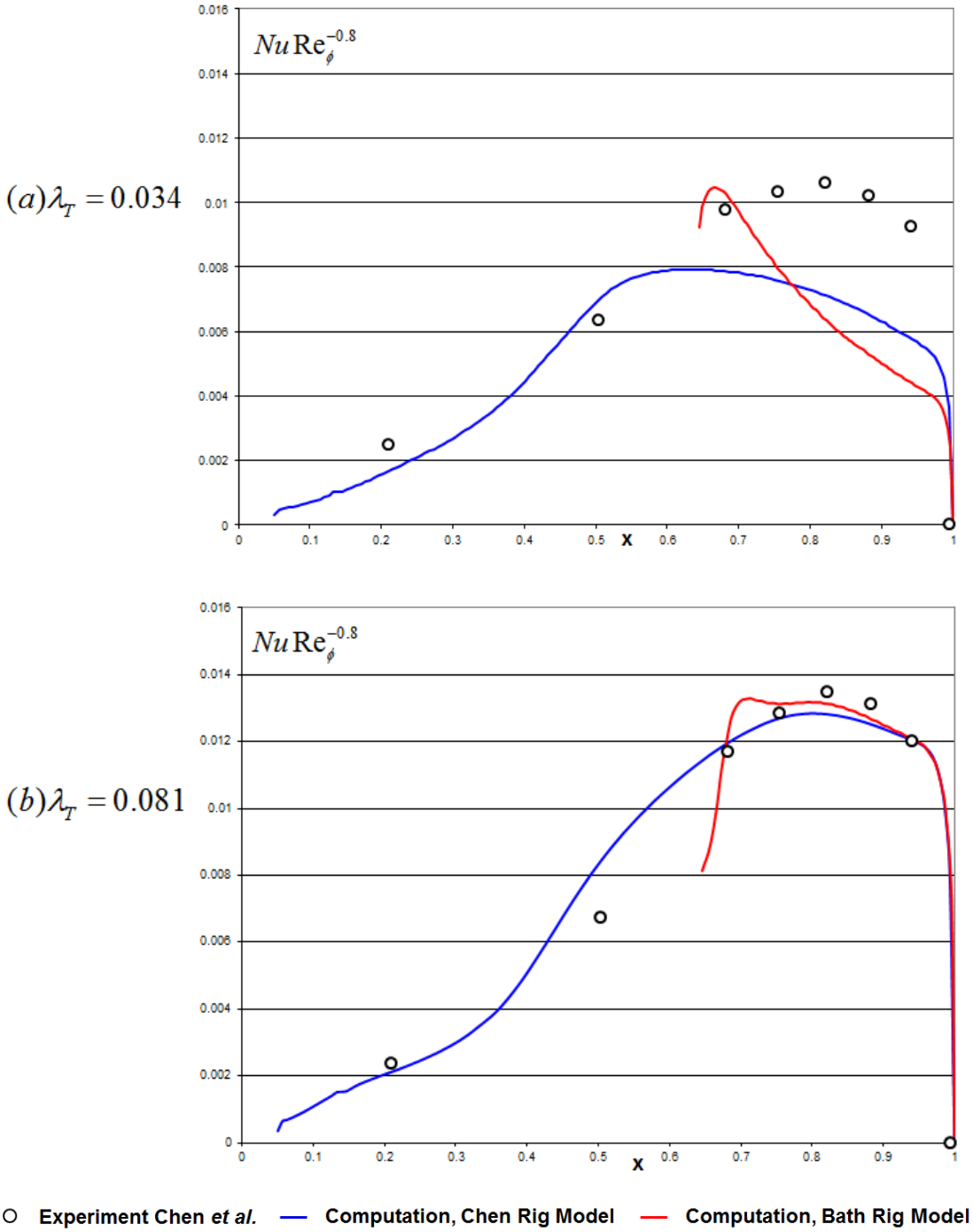

Figure 4-13 The effect of geometry on the radial distribution of $Nu\,\mathrm{Re}_{\phi}^{-0.8}$

Computed radial distributions of $Nu\,\mathrm{Re}_{\phi}^{-0.8}$ for the Chen and Bath Rig Models are shown in Figure 4-13. In general, the effect of geometry is small, especially for the high λ_T case. At high λ_T, the comparison is better between the Chen Rig Model result and the experimental data. The computed results for the Bath Rig Model show an effect at the inlet region. For lower λ_T case, there still is poor prediction of the

measurements at larger values of $x = r/b$ for the Chen Rig Model.

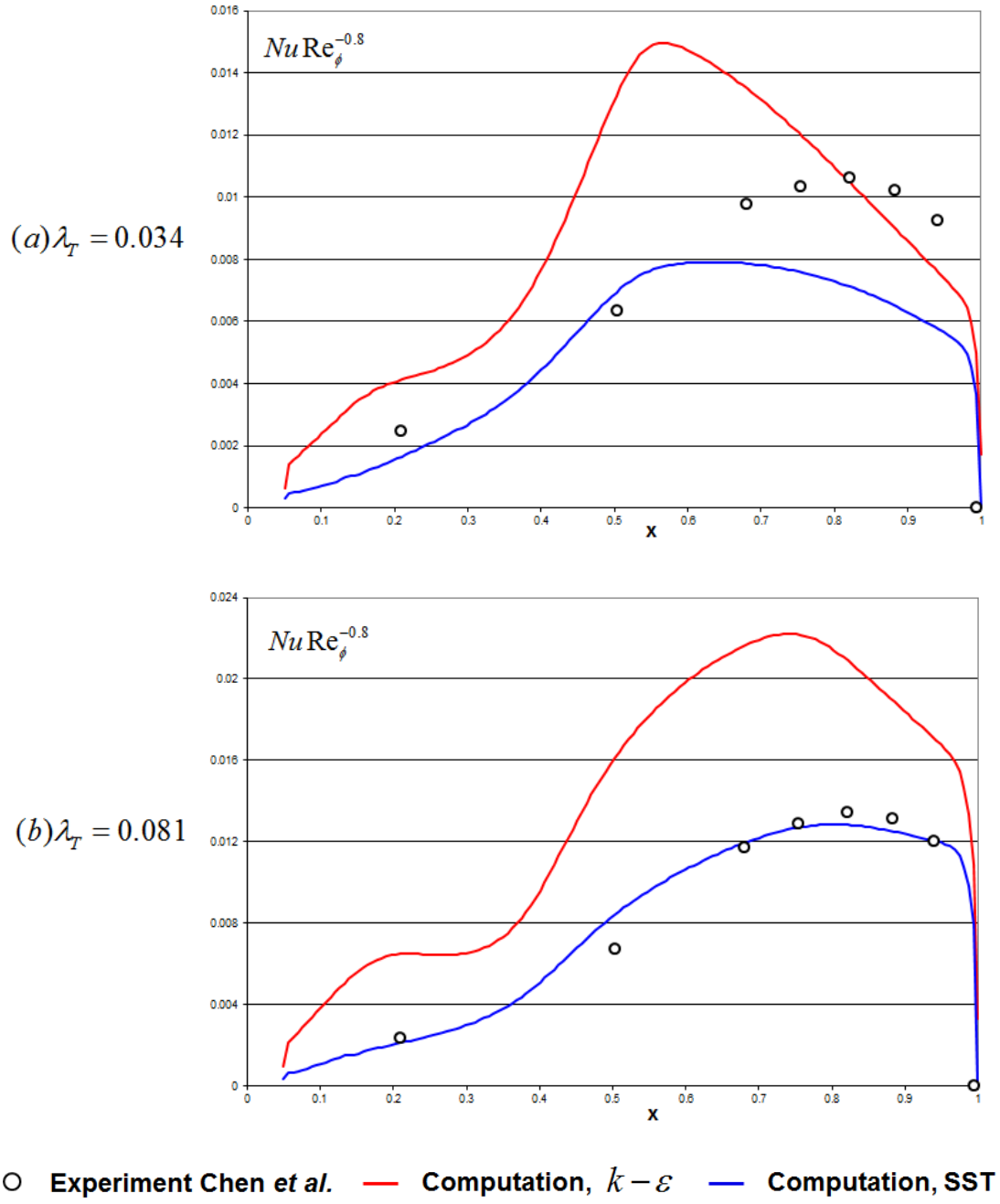

Figure 4-14 The effect of turbulence model on the radial distribution of $Nu\,\mathrm{Re}_\phi^{-0.8}$

As discussed previously, these poor results for low λ_T are likely to be due mainly to the turbulence model. Further computations using the Chen Rig Model with different turbulence models are shown in Figure 4-14. In these computations, results using the $k-\varepsilon$ turbulence model are compared with those of the SST $k-\omega$ turbulence

model. The $k-\varepsilon$ model produces much higher values of $Nu\,\mathrm{Re}_{\phi}^{-0.8}$, over predicting the experimental data at both low and high λ_T due to the wall function near-wall treatment. These results suggest that these two turbulence models cannot predict turbulence accurately for low value of λ_T, though the SST $k-\omega$ turbulence model shows relatively better performance due to the low Reynolds number resolved boundary layer near-wall treatment. The low Reynolds number treatment needs very fine meshes ($y^+ \sim 1$). The y^+ values for the models used in this thesis are typically 1 to 1.5 for the SST $k-\omega$ turbulence model while the value used by Chen *et al.* is less than 0.5. Therefore the computed results for low λ_T shown here are worse than that of Chen *et al.*, shown in Figure 2-5. Models with very fine mesh increases computation time, which may be not suitable for engine design.

4.3. **Chapter summary**

The geometry difference between the Bath and Chen Rig Model influences the axial distribution of radial velocity at low radius. No effect of geometry is found on the distribution of circumferential velocity. For heat transfer, the thermal condition on the rotor and the geometry has little influence on the radial distribution of Nusselt number. Furthermore, the SST $k-\omega$ turbulence model provides reasonable results for the heat transfer at high λ_T. However, the computational results are not good at low λ_T, which is mainly due to low levels of computed turbulence in the selected turbulence model and moderately fine mesh. Most results in this chapter show that the simple 2D axial-symmetry rotor-stator model is validated and can quantitatively predict most fluid dynamic and heat transfer features in the wheel-space. At the same time, the size of model reduces markedly compared with 3D models and, consequently, the computing time reduces to 12 hours for each computation.

5. Prescribed ingestion model: Axial-clearance seal

This chapter will present the prescribed ingestion model with the simplest seal geometry, the axial-clearance seal. The prescribed ingestion model geometry is based on the experimental rig at the University of Bath (Figure 5-1 (a)) and is shown in Figure 5-1 (b). The computational model includes the inner seal at low radius and the outer wheel-space from the experimental rig. Sealing flow enters the outer wheel-space through the inner seal. An ingress inlet and an egress outlet are located at the outer shroud of wheel-space as shown. This model contains around 45000 mesh cells and the SST $k-\omega$ turbulence model is used. In this chapter, different boundary assumptions for the ingress flow will be discussed. Figure 5-1 (b) shows the ingress inlet at the centre of the outer shroud with the outflow boundary is adjacent to the rotor. This arrangement was found to give the best performance. Detailed results of the computed fluid dynamics in the wheel-space are presented using this arrangement, and the computed sealing effectiveness compared with experimental results. Heat transfer computations have also been carried out using this prescribed ingestion model for the axial-clearance seal.

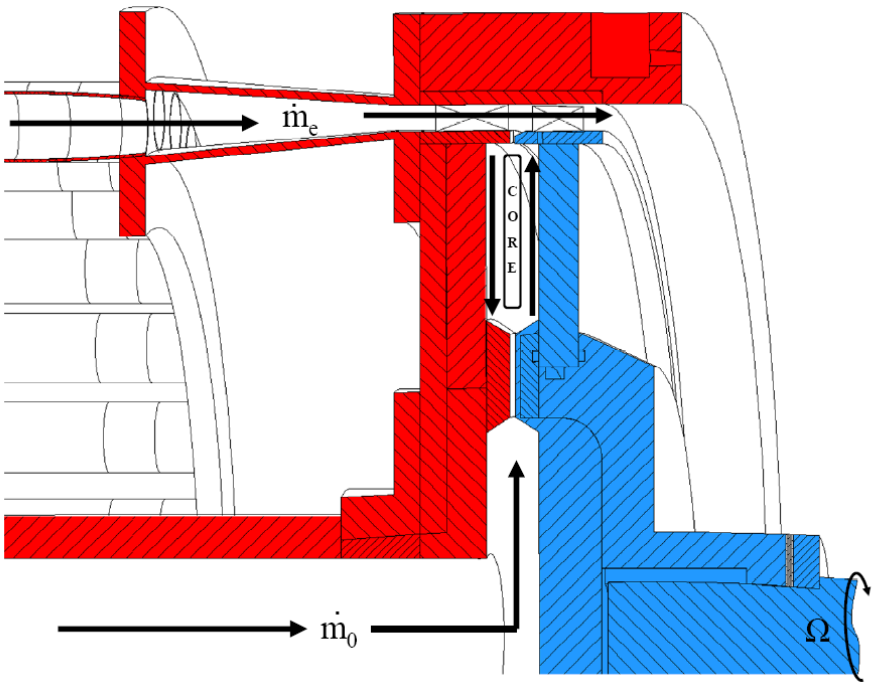

(a)

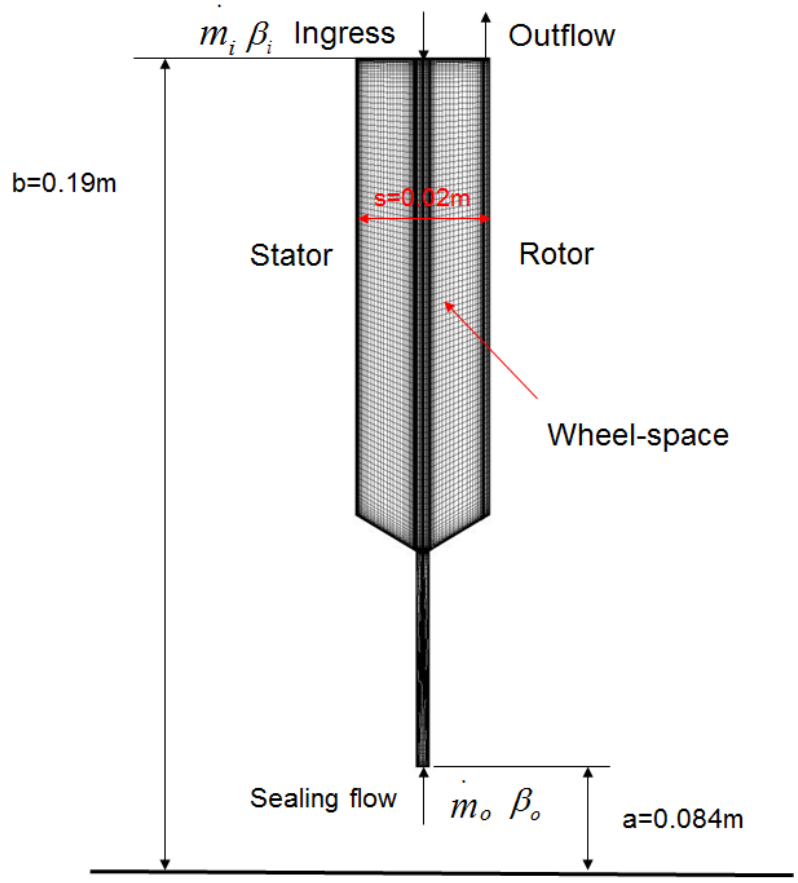

(b)

Figure 5-1 (a) The experimental rig in University of Bath [51] (b) The prescribed ingestion model with axial-clearance seal and mesh grid

5.1. **Mass-weighted average assumption for ingestion**

Figure 5-2 shows measurement for a 2-mm (s_c) axial-clearance seal with externally-induced (EI) ingress from experiments were carried out at the University of Bath. The experiments [55] reveal that the sealing effectiveness on the stator is virtually invariant with radius. The data in Figure 5-2 is based on the measurements collected at r/b=0.958. As the non-dimensional sealing flow is increased from 0 to $\Phi_{\min,EI}$, the sealing effectiveness increases from 0 to 1. Both sealing effectiveness (ε) and non-dimensional flow parameter for ingress ($\Phi_{i,EI}$) are displayed in this figure. The symbols denote experimental measurements and the lines are theoretical curves fitted to the experimental points using the statistical technique of Zhou *et al.* [53].

These experimental data are for the design condition. For consistency, most of the computations for the prescribed ingested model are also based on experiments at the design condition and are carried out for one of two rotational Reynolds numbers: $\mathrm{Re}_\phi = 5.32\times10^5$ and 8.17×10^5.

According to Figure 5-1 (b), the main requirement for the computational model is the ingested flow rate and its associated (inlet) boundary conditions. The value of the ingested flow rate can be deduced from the experimental data shown in Figure 5-2. For EI ingress, the flow ingested from the mainstream flow in the annulus would enter the wheel-space through the rim seal with a relatively high value of swirl ratio. The prescribed ingestion model boundary condition assumes some mixing of the ingested flow prior to entering the wheel-space. Two possible assumptions are discussed here. The first is a mass-weighted average assumption for which the swirl ratio of the ingested flow at the ingress inlet boundary is given by:

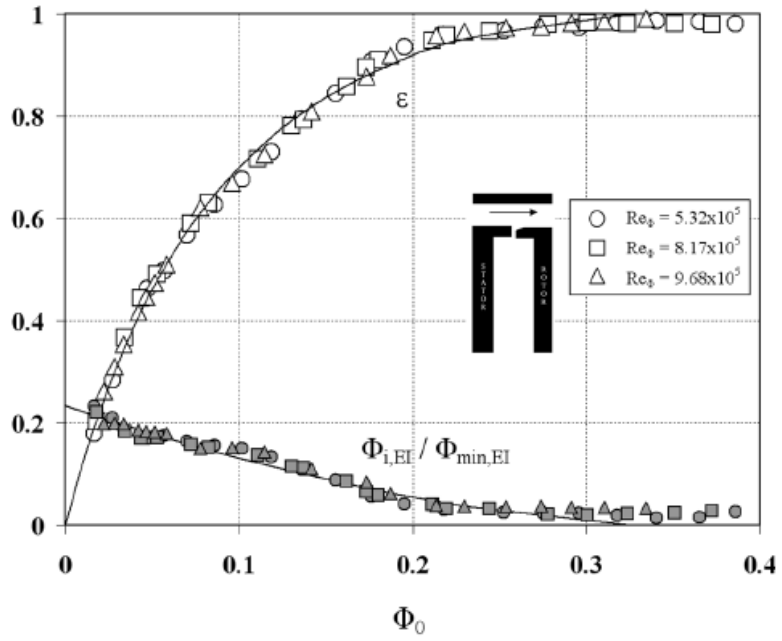

Figure 5-2 Experimental data for axial-clearance seal with EI ingress [51]

Mass-weighted average: $$\beta_{i,mass} = \frac{\dot{m}_i \beta_{ann} + \dot{m}_o \beta_o}{\dot{m}_i + \dot{m}_o} \qquad (5\text{-}1)$$

β_{ann} is the swirl ratio in the annulus and β_o is the swirl ratio of the sealing flow at the sealing flow inlet. An additional assumption is a momentum-weighted average.

Momentum-weighted average: $$\beta_{i,mom} = \frac{\dot{m}_i V_{r,i} \beta_{ann} + \dot{m}_o V_{r,o} \beta_o}{\dot{m}_i V_{r,i} + \dot{m}_o V_{r,o}} \quad (5\text{-}2)$$

Here $V_{r,i}$ is the radial velocity of is ingested flow at ingress inlet and $V_{r,o}$ is the radial velocity of sealing flow at sealing flow inlet. These two velocities are calculated as:

$$V_{r,i} = \frac{\dot{m}_i}{2\pi\rho b s_i}, \quad V_{r,o} = \frac{\dot{m}_o}{2\pi\rho r_o s_o} \quad (5\text{-}3)$$

Where s_i and s_o are the axial clearance of ingress inlet and sealing flow inlet respectively. r_o is the radius of the axial clearance at the sealing flow inlet.

The value used for β_{ann} is obtained from the 3D computations with annulus described in Chapter 3. As β_o is small in comparison with β_{ann}, β_o was assumed initially to be zero. After comparisons for two weighting assumptions, the effect of the value of β_o will be discussed.

Re_ϕ	λ_T	$\dot{m}_o$	$\dot{m}_i$	$\beta_{i,mass}$	$\beta_{i,mom}$
8.17×10^5	0.063	0.01176	0.00971	0.892	0.740
	0.114	0.02128	0.00669	0.470	0.158
	0.242	0.04516	0.00165	0.069	0.002

Table 5-1 Computational parameters for Mass-weighted and Momentum-weighted average assumptions

Three sealing flow rates were chosen to compare the mass-weighted and momentum-weighted averaging assumptions. The parameters used for the

computations are shown in Table 5-1. Note that the turbulent flow parameter λ_T is directly linked to Φ_o: $\lambda_T = 2\pi G_c \Phi_o \mathrm{Re}_\phi^{0.2}$.

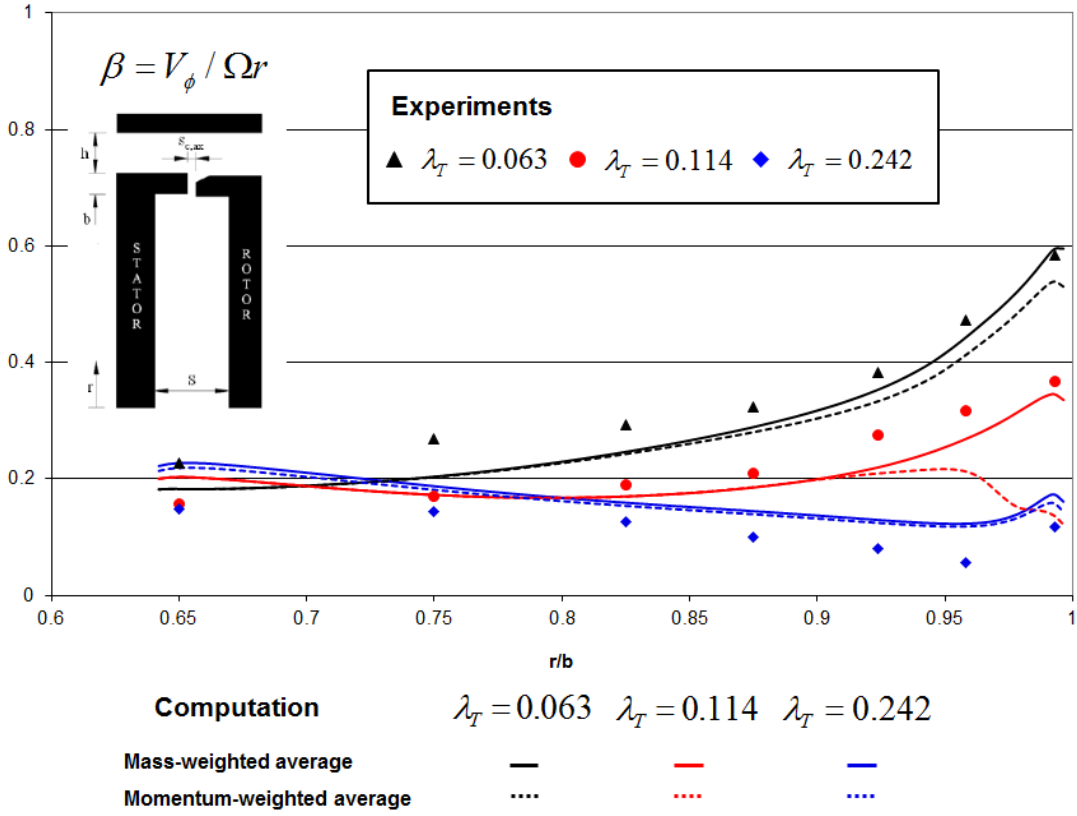

Figure 5-3 Swirl ratio distribution for axial-clearance seal with Mass-weighted and Momentum-weighted average assumptions, z/s =0.25 (symbols denote the experimental data [60])

Figure 5-3 shows computed swirl ratio distributions at z/s =0.25 using the mass-weighted and momentum-weighted average assumptions. Experimental measurements [60] also are shown in the figure. The figure shows that the swirl ratio in the wheel-space reduces as the sealing flow rate increases. In general, the computations have qualitatively captured the trends measured during the experiments. At both high and low sealing flow ($\lambda_T = 0.063$ and $\lambda_T = 0.242$), the computations agree well at all radii. Moreover, the mass-weighted average assumption gives results closer to the experimental data than the momentum-weighting assumption.

At $\lambda_T = 0.114$, the momentum-weighted assumption gives β_i =0.158, which is much smaller than the experimental data near r/b =1. The secondary flow

streamlines for this case are shown in Figure 5-4. Unusual circulations occur near the rim seal region for the Momentum-weighted assumption. These unwanted circulations give rise to a different trend of swirl ratio to experiment at high radius. In comparison, the mass-weighted assumption gives reasonable β_i when compared with the measurement and a reasonable flow structure.

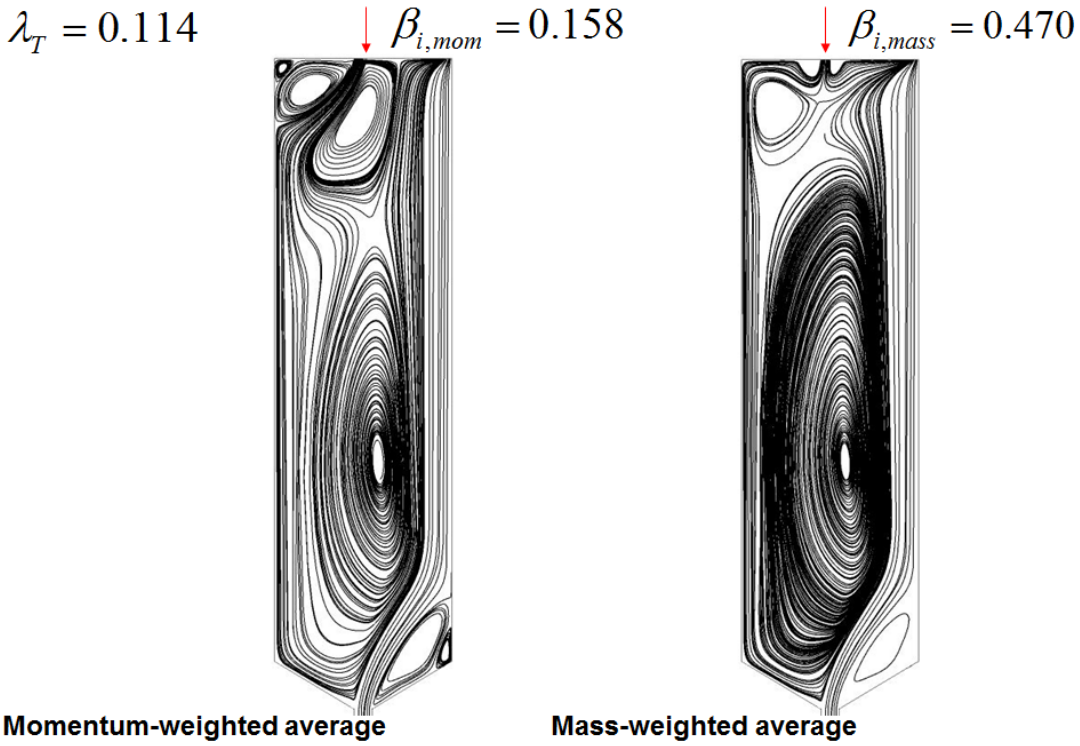

Figure 5-4 Secondary flow streamlines for Momentum-weighted and Mass-weighted average at $\lambda_T = 0.114$

At high sealing flow rate ($\lambda_T = 0.242$), the difference between the mass- or momentum-weighted average assumptions is very small and can be ignored. When the sealing flow is high and consequently the ingested flow is very small, the influence of ingress on the swirl ratio in wheel-space becomes negligible.

In short, according to the figure, the mass-weighted average assumption gives good agreement with experiment and provides a more realistic estimate for the inlet swirl ratio for the ingested flow than the momentum-weighted average assumption. Therefore, the mass-weighted average assumption will be adopted in the prescribed ingestion model in this thesis.

The effect of value of β_o on the swirl ratio distribution in wheel-space is shown in Figure 5-5. The value of β_o was obtained by computations involving the inner wheel-space inboard of the inner seal in the experimental rig, as shown in Figure 5-1 (a).

Figure 5-5 illustrates that there is little effect of β_o on the swirl ratio distribution in the wheel-space. Slight differences exit at low radius for the computations at each of the three sealing flow rates. Note that β_o is small in comparison with β_{ann} and has a minimum influence on the final value of β_i according to the definition of mass-weighted average assumption. For convenience, the remaining computations for the prescribed ingestion model adopt β_o equal to zero, which means that the sealing flow has no swirl at inlet.

The mass-weighted average assumption is applied not only to the swirl ratio of the ingested flow, but also to the mixed concentration of ingested flow. The mass-weighted average concentration is similar to that for the swirl ratio and given by:

$$c_{i,mass} = \frac{\dot{m}_i c_a + \dot{m}_o c_o}{\dot{m}_i + \dot{m}_o} \tag{5-4}$$

Here c_a and c_o are the concentration in the annulus and in the sealing flow at inlet respectively. The solution for the concentration as a passive scalar allows comparisons to be made with measurements of CO_2 tracer concentration made in experiments. For the computations, $c_a = 0$ and $c_o = 1$.

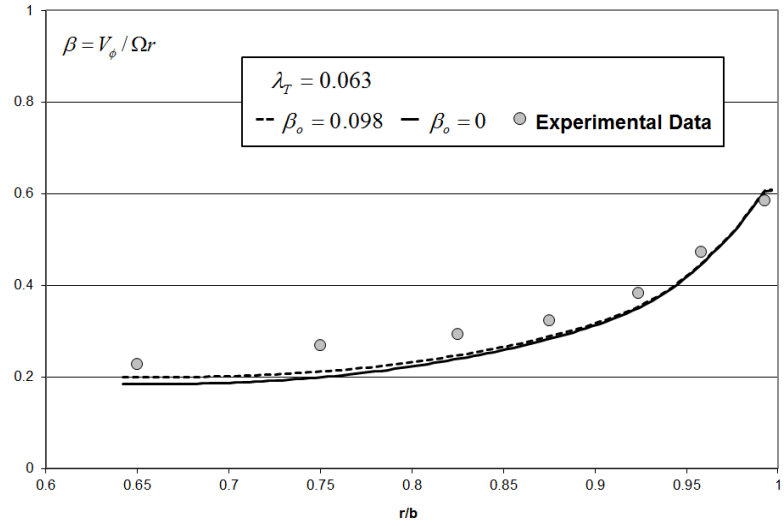

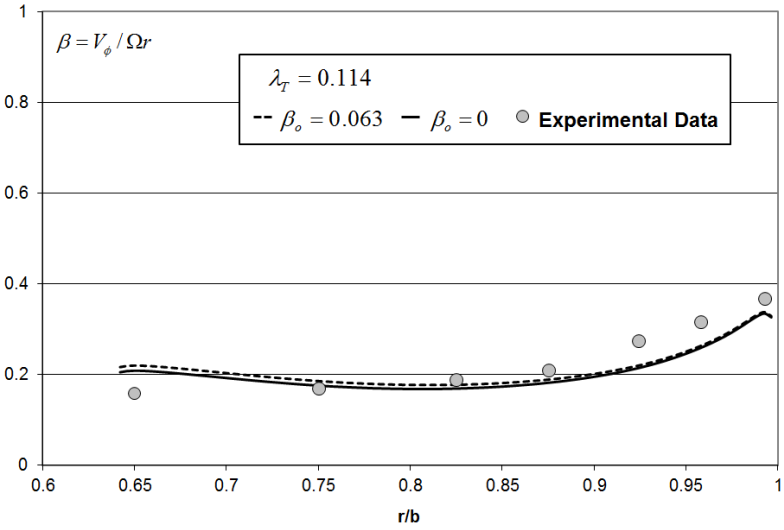

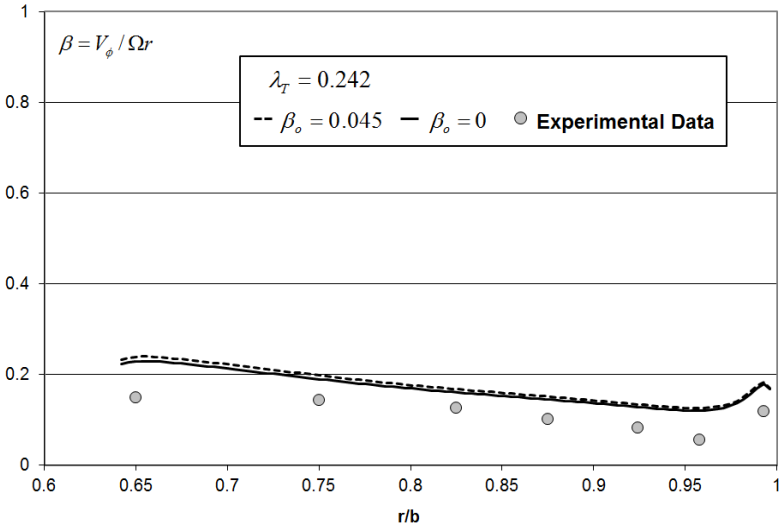

Figure 5-5 The effect of β_o on swirl ratio distribution, z/s =0.25 (symbols denote the experimental data [60])

5.2. **The effect of layout of ingress inlet and egress outlet**

Layout A	Layout B	Layout C
Ingress inlet at centre	Ingress inlet at z/s=1/3	Ingress inlet at stator wall
Egress outlet at rotor wall	Egress outlet at z/s=2/3	Egress outlet at centre

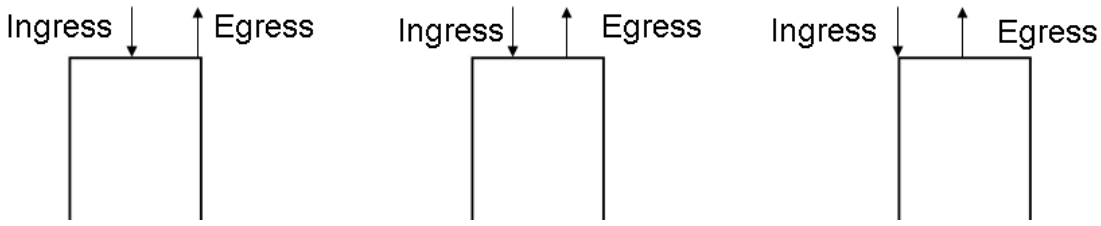

Figure 5-6 Different layouts of ingress inlet and egress outlet

In the preliminary studies of the prescribed ingestion model, the ingress inlet and egress outlet were both located about the mid-plane of the model on the outer shroud, in order to simulate this real location at the rim seal. These computations, however, resulted in the ingested flow leaving through the egress outlet directly (short-circuit flow). Hence, the inlet and outlet region were separated in order to study the influence of ingress on the flow in the wheel-space. Three different possible arrangements of the inlet and outlet are discussed here referred to as Layout A, Layout B and Layout C as illustrated in Figure 5-6. For all layouts, at the top wheel-space, half of the outer shroud is treated as stationary (z/s =0~0.5) and half is treated as rotating (z/s =0.5~1.0).

Figure 5-7 shows the computed swirl ratio distribution at z/s=0.25 for the three layouts for $\mathrm{Re}_\phi = 8.17\times10^5$. In general, there is little difference between the results for these three layouts, except at high radius. At $\lambda_T = 0.063$ (Figure 5-7 (a)), the ingested inlet for Layout B (z/s=1/3) is closest to the location z/s=0.25, where measurement are available. Layout B results in an over-prediction of the measured swirl near to r/b=1. In this diagram, the data with no ingestion from Chen *et al.* [8] at

a similar $\lambda_T (= 0.081)$ are included. Both computations and experiments give reasonable swirl ratio level compared with Chen *et al.* data although the value of λ_T is slightly different. The results from the Bath rig are higher than the Chen *et al.* data due to the lower λ_T used. For $\lambda_T = 0.114$ (Figure 5-7 (b)) both the ingested flow rate and its prescribed swirl level reduce, so that the over-prediction of measured swirl for Layout B is less severe.

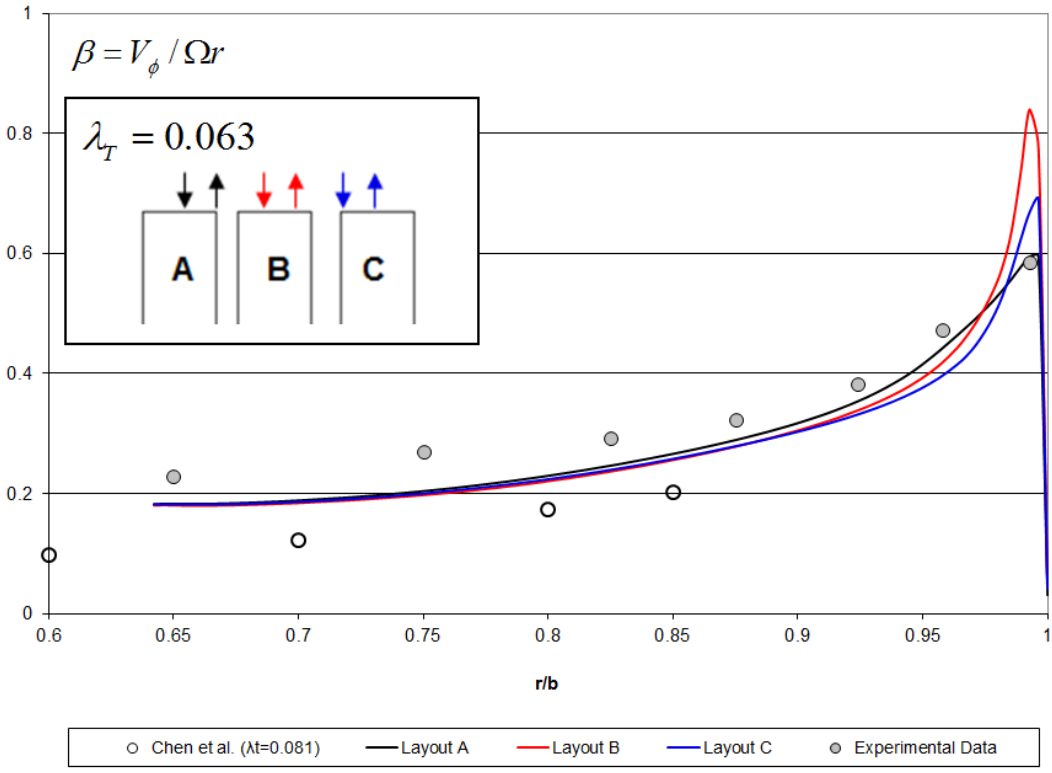

(a)

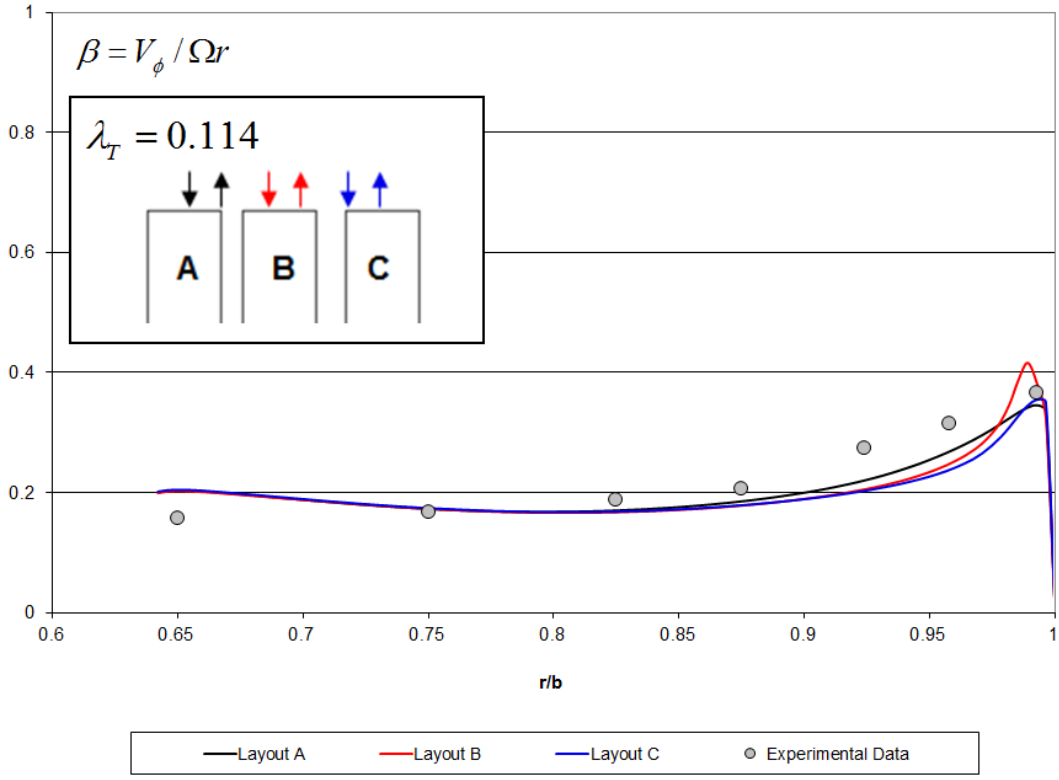

(b)

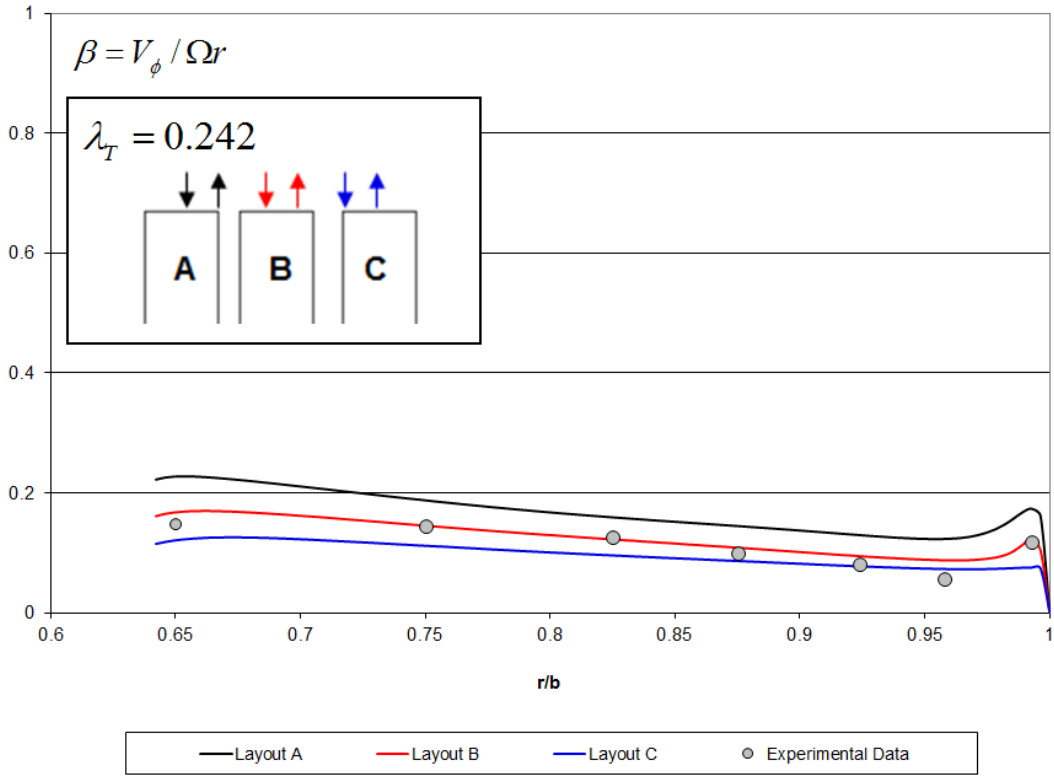

(c)

Figure 5-7 The effect of layout on swirl ratio distribution, z/s =0.25 (closed symbols denote the experimental data [60] and open symbols denote the experimental data [8])

The greatest difference between results for the three layouts occurs at the highest λ_T. In this case, the ingested flow rate and its associated swirl level is small and has little influence on the computed swirl distribution. The different location of the egress outlet becomes the main factor causing the differences between the results. Figure 5-8 shows the swirl contours for the three layouts at $\lambda_T = 0.242$. For Layout A, the outlet is on the rotor side and the rotating shroud separates the inlet and outlet. According to the contours, the rotating shroud introduces high swirl and this consequently influences the swirl ratio near the stator. In the contours for Layout C, the high swirl produced by rotating shroud does not influence the ingested flow due to the outlet at the mid-plane. This layout, therefore, gives the lowest swirl. For Layout B, there still is a part of rotating shroud between the inlet and outlet and this gives rise to an intermediate level of swirl. Layout A gives the most accurate swirl ratio for most cases compared with the measurements, although slightly over-predicting the swirl ratio at the very high λ_T case. Hence, Layout A was chosen for the prescribed ingestion model.

$\lambda_T = 0.242$

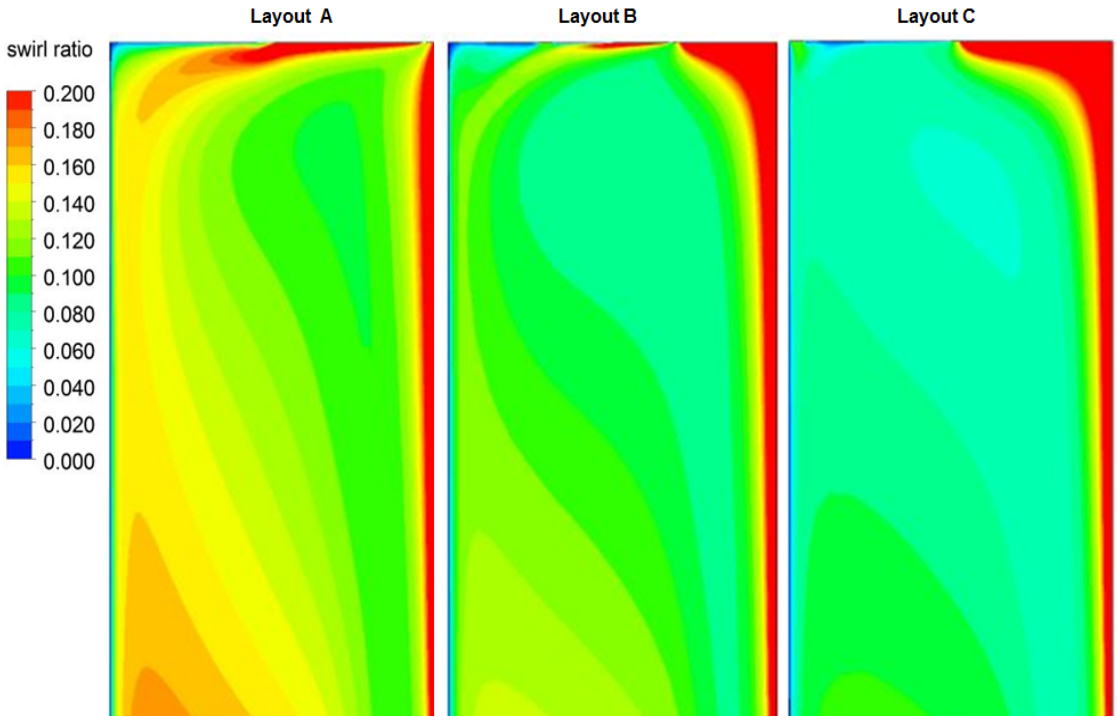

Figure 5-8 The swirl contours for three layouts at $\lambda_T = 0.242$

5.3. **Fluid dynamics in the wheel-space**

In this section, the fluid dynamics in the wheel-space for the prescribed ingestion model is discussed. Figure 5-9 shows the comparison between swirl distributions for the prescribed ingestion model and the Bath rig rotor-stator model (with no ingress) for three different values of λ_T. The open symbols represent the $\beta_{i,mass}$ at the ingress inlet for the prescribed ingestion model. The figure illustrates that the zero swirl sealing flow reduces the swirl ratio in wheel-space. At each value of λ_T, the prescribed ingestion model gives rise to higher swirl in the wheel-space, due to the swirl ratio associated with the ingested flow. The influence of ingress on swirl ratio at high values of non-dimensional radius (r/b) decreases as λ_T increases as the amount of ingestion also reduces.

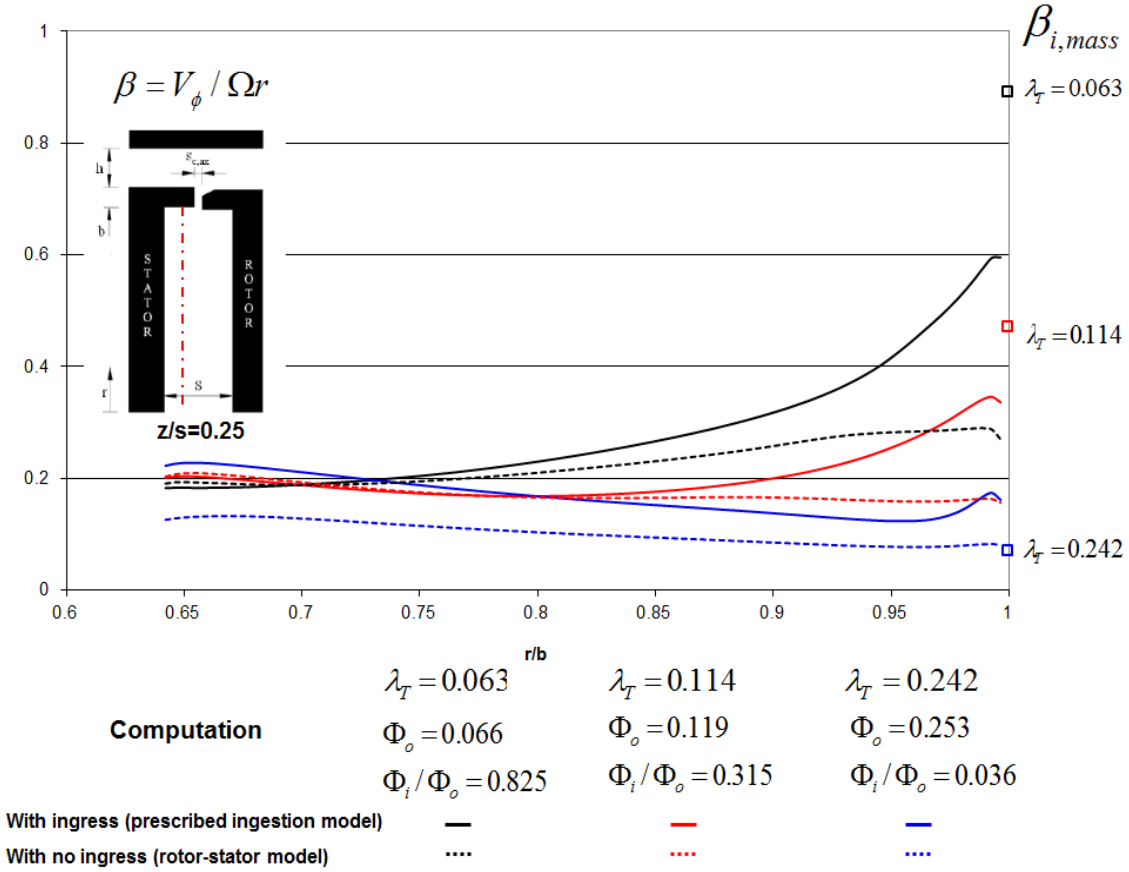

Figure 5-9 Comparison of swirl distributions for the prescribed ingestion model and the Bath rig rotor-stator model with no ingestion, z/s =0.25

Figure 5-10 shows the comparison of swirl ratio for the prescribed ingestion model and Chen *et al.* [8] at r/b=0.7. According to the value of λ_T, the Chen *et al.* data should be between the two lines predicted by the prescribed ingestion model. However, both results from the prescribed ingestion model are higher than the result from Chen *et al.* The narrow gap of the prescribed ingestion model as shown in Figure 5-1 (b) results in a high swirl ratio at the inlet of the outer wheel-space, and consequently leads to the feature shown in this figure.

Figure 5-11 shows the swirl distribution at different Re_ϕ with similar values of λ_T for the prescribed ingestion model. The two results are very close although the rotational speed is different. This illustrates that Re_ϕ has no significant effect on the distribution of swirl ratio and that λ_T is the dominant factor governing this distribution.

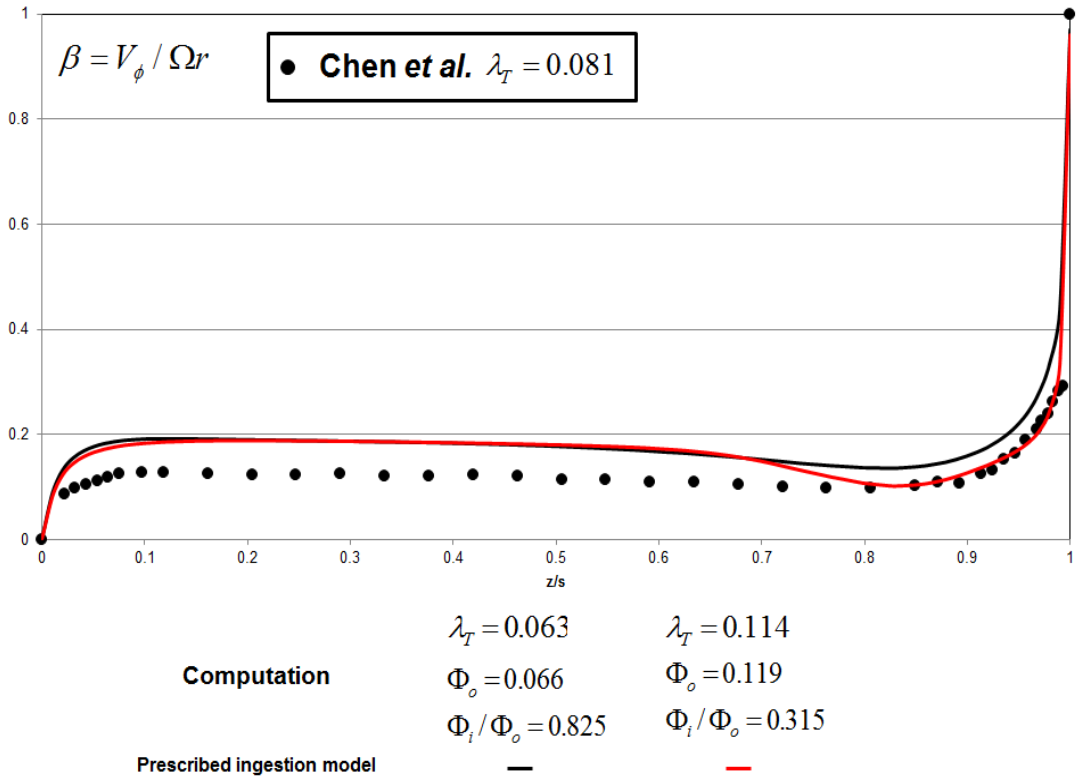

Figure 5-10 Comparison of swirl ratio for the prescribed ingestion model and Chen *et al.* [8] at r/b=0.7

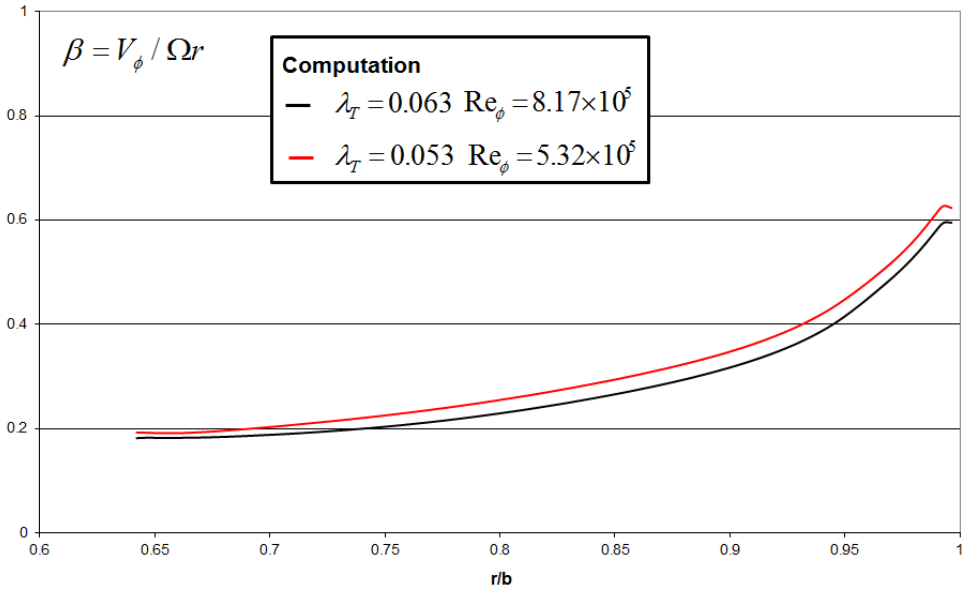

Figure 5-11 Comparison of swirl distribution for different rotational speed for the prescribed ingestion model at similar λ_T

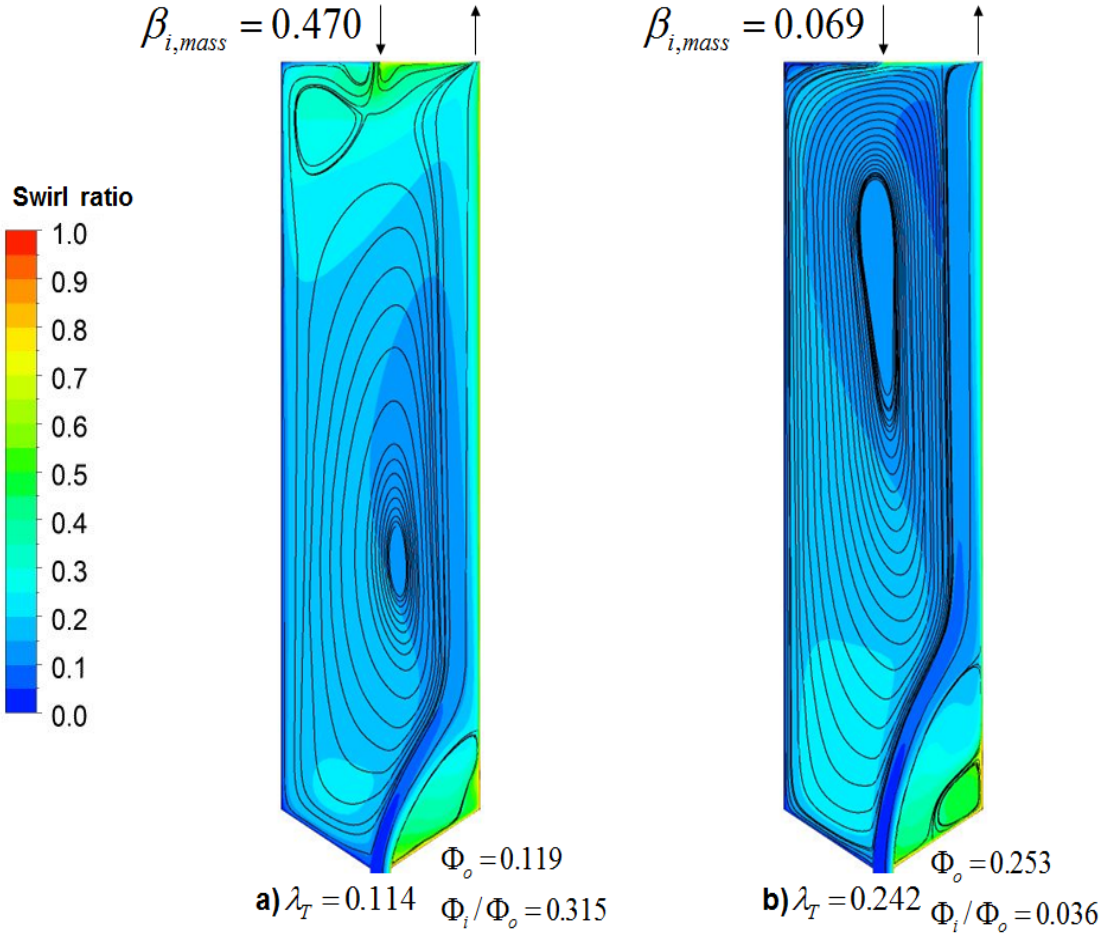

Figure 5-12 Secondary flow streamlines and swirl contours for the prescribed ingestion model with axial-clearance seal

Figure 5-12 shows secondary flow streamlines and swirl contours in the wheel-space for the prescribed ingestion model. According to the streamlines, at low radius the sealing flow enters towards the rotor. At the top of the wheel-space some of ingested flow migrates directly to the outlet and the rest is drawn towards the stator. A core of rotating fluid exists between the stator and rotor. The angled rotor surface at low radius causes a secondary flow circulation and this increases in size as the sealing flow rate (λ_T) increases.

Detailed velocity profiles for the $\lambda_T = 0.114$ case are shown in Figure 5-13. Tangential velocity is almost invariant with z in the rotating core at the three radial locations shown, and the value of the swirl ratio increases with radius. The peak value of radial velocity near the rotor decreases with radius and the radial velocity is close to zero between stator and rotor boundary layers. These features illustrate that the ingestion has only a slight effect on the rotor-stator flow structure in the wheel-space.

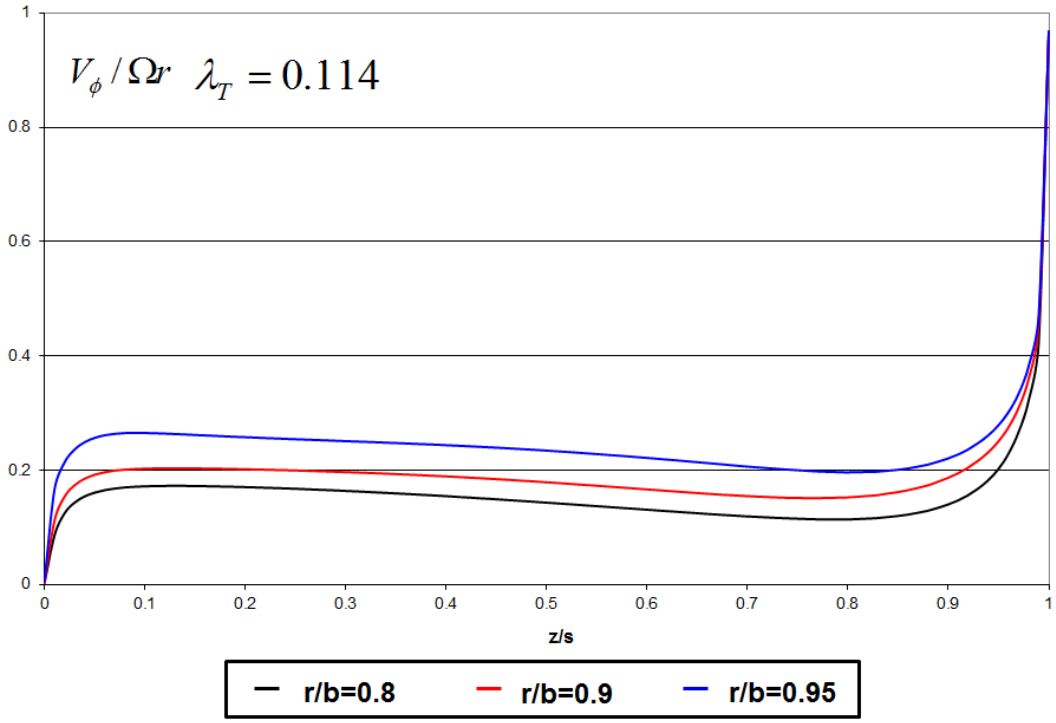

(a)

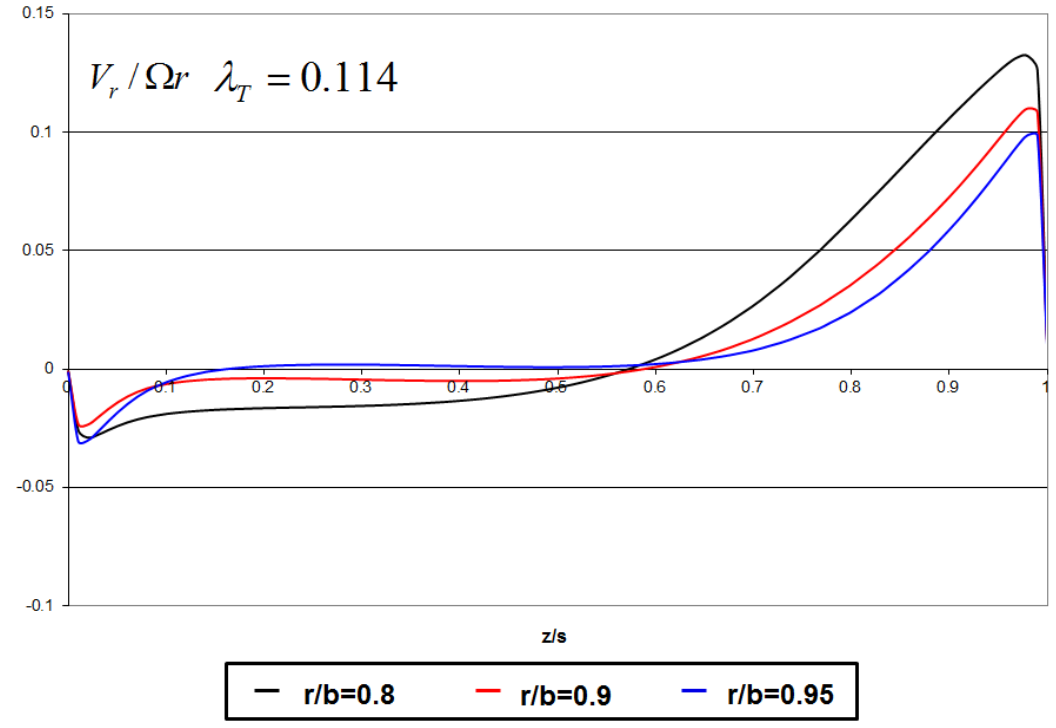

(b)

Figure 5-13 Velocity distributions for the prescribed ingestion model with axial-clearance seal

5.4. **Distribution of sealing effectiveness in the wheel-space**

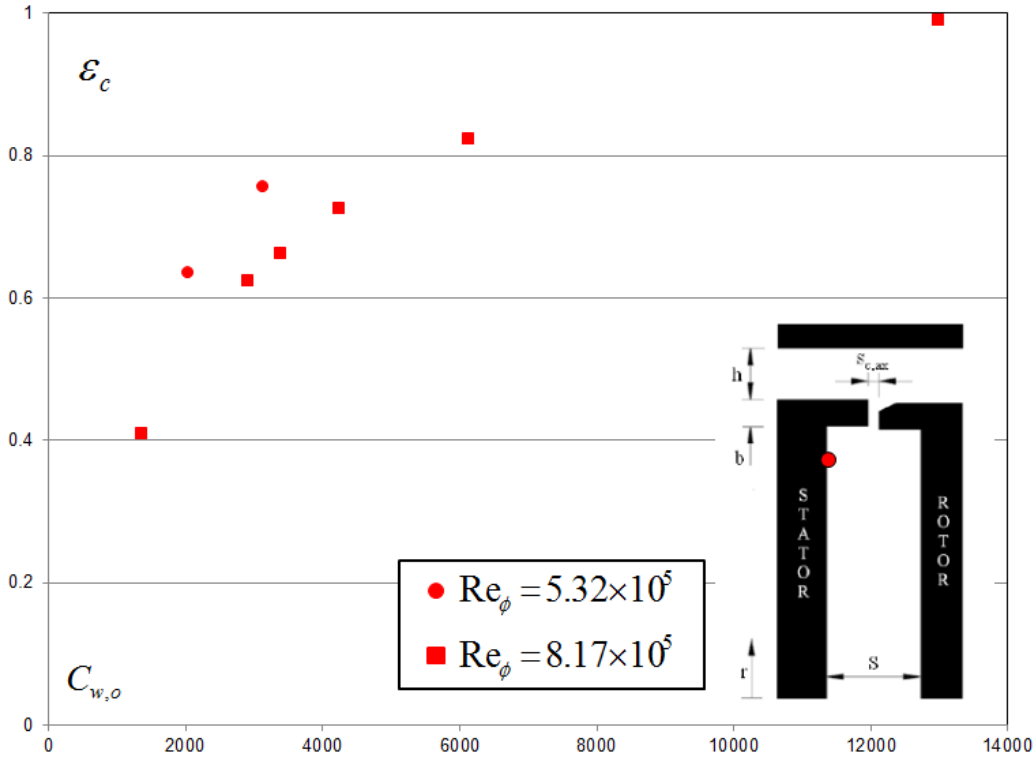

Figure 5-14 Computed variation of effectiveness with $C_{w,o}$ for axial-clearance seal

The non-dimensional sealing flow rate ($C_{w,o}$) and non-dimensional sealing parameter (Φ_o) are two common parameters used to represent the sealing flow in computations and experiments. The variation of computed sealing effectiveness (at the monitor location on the stator at r/b=0.958 as illustrated in the inset diagram) with $C_{w,o}$ at two rotational speeds is shown in Figure 5-14. The sealing effectiveness increases with increasing $C_{w,o}$, as the sealing flow reduces ingestion from the annulus. It is clear that the gradient of the ε_c curve with $C_{w,o}$ is different at the two rotational speeds. According to the figure, at the same $C_{w,o}$, higher effectiveness is obtained at the lower rotational speed. In other words, a larger $C_{w,o}$ is required to maintain the same effectiveness as Re_ϕ increases.

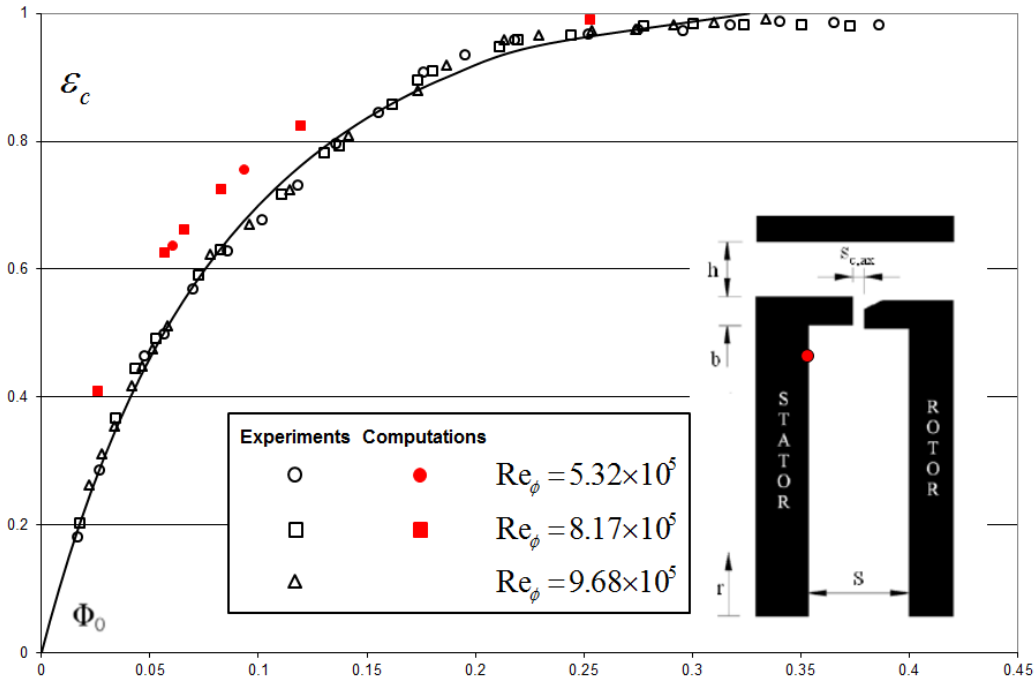

Figure 5-15 The computed variation of effectiveness with Φ_o for axial-clearance seal compared with experimental data [51]

The results in Figure 5-14 are re-plotted using the non-dimensional sealing flow parameter Φ_o in Figure 5-15. In this figure, the closed symbols denote the computed results, while experimental measurements [51] are shown as open symbols and the theoretical curve fit for the measured effectiveness is also shown. Both the experimental and computed results illustrate that the effect of Re_ϕ on sealing effectiveness vanishes when plotted in this figure. Φ_{min}, the minimum value of Φ_o required to prevent ingress, is independent of rotational speed. The computed results have the same qualitative trend as the experimental data (and theoretical fit), however the effectiveness is over-predicted. The computed value of Φ_{min}, the minimum flow rate to prevent ingress, agrees reasonably well with the experimental data.

Figure 5-16 shows the computed radial distribution of effectiveness on the stator. Experimental data [60] are included for comparison. The open symbols represent the $C_{i,mass}$ at the ingress inlet. The experimental data suggest that the ingress flow mixes fully at the rim seal region, so that consequently the concentration (representing

effectiveness) of the fluid in the boundary layer on the stator varies little with radius. The computed results have a similar trend to the experiments, and accord qualitatively with the results of 3D computations such as those of Rabs *et al.* [42]. The radial variation in the computed results is slightly greater than in the experiments, indicating some further mixing exists in the stator boundary layer for the computations. Furthermore, as in Figure 5-15, the computations over-predict the measured values of effectiveness. The migration of some of the flow from the prescribed ingestion inlet directly to the outlet at the outer radius of wheel-space (as shown in Figure 5-12) contributes to this over-prediction.

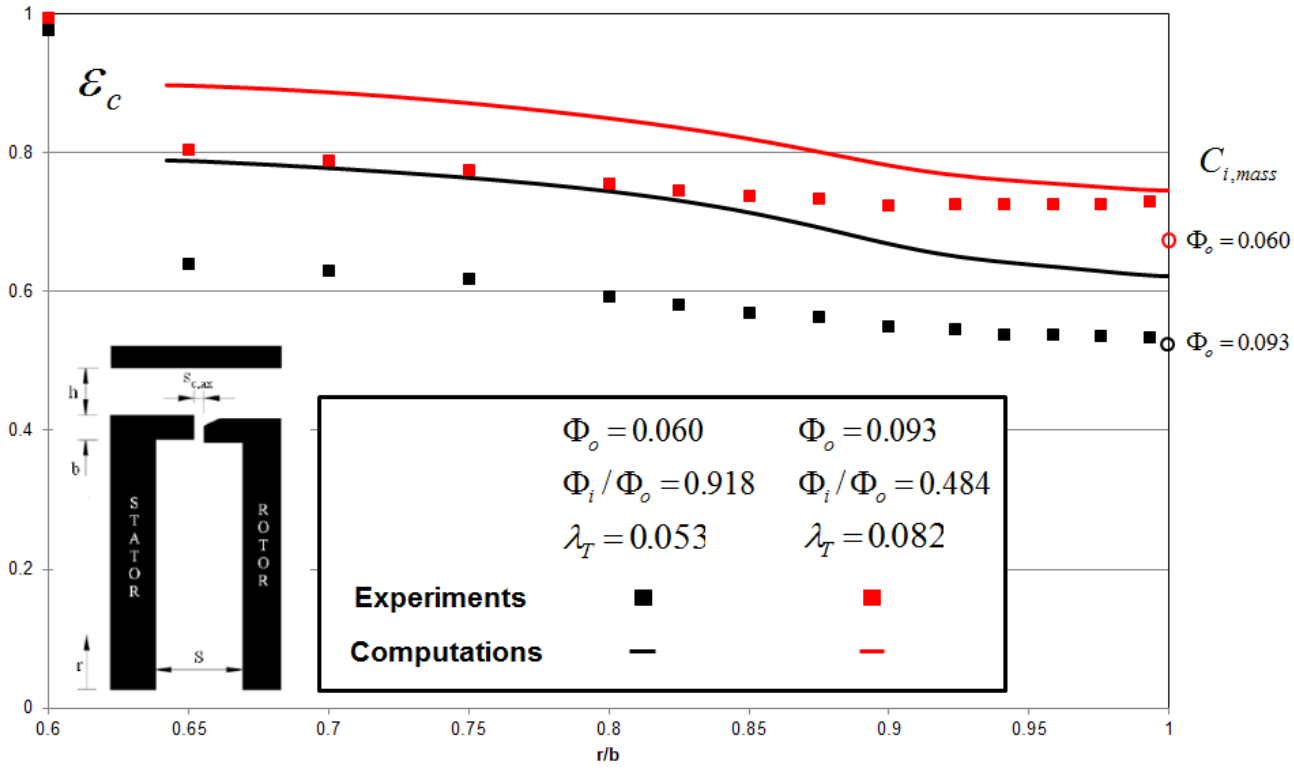

Figure 5-16 Radial distribution of effectiveness on the stator for the axial-clearance seal compared with experimental data [60]

The computed radial distribution of effectiveness on the rotor is shown in Figure 5-17 and is compared with the measured adiabatic effectiveness for the rotor [61]. Compared with the results for the stator, higher values of sealing effectiveness occur on the rotor, since the sealing flow provides thermal protection. In general, the computations qualitatively predict the trends observed in the experimental data. Furthermore, the computations over-predict the measured effectiveness on the stator

and this fluid enters the boundary layer on the rotor by entrainment through the core region. The computed result also over-predicts the effectiveness for the lower value of λ_T shown. At the higher value of λ_T, the computed rotor effectiveness agrees well with the measurements, although for this case both computations and experiments show that the rotor is well protected from the effect of ingestion.

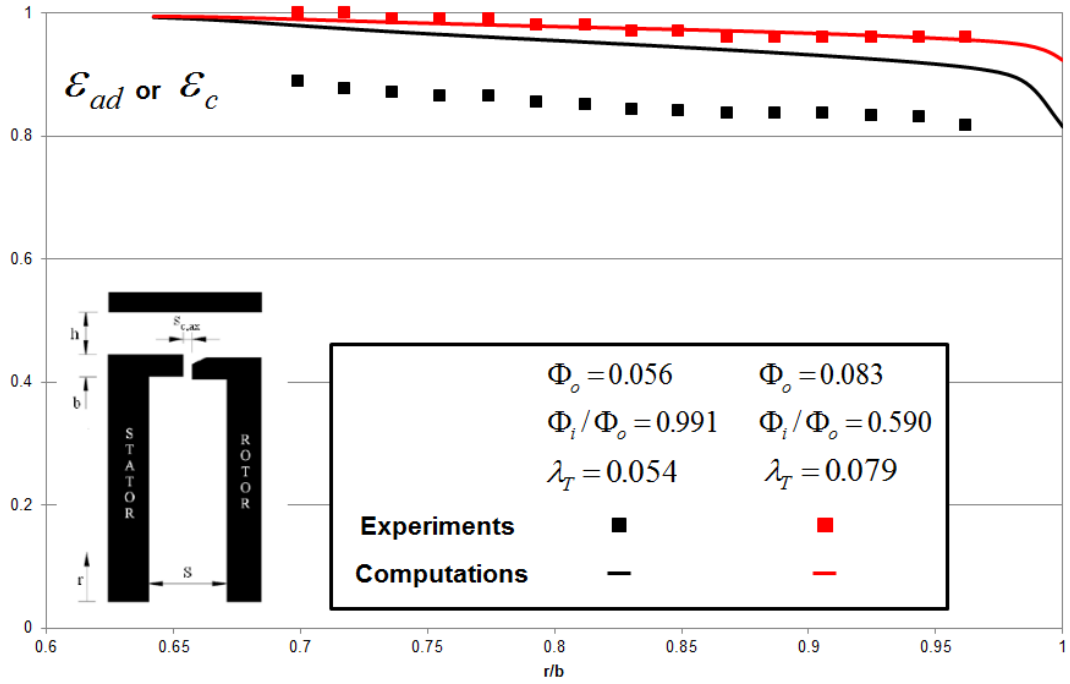

Figure 5-17 Radial distribution of effectiveness on the rotor for the axial-clearance seal compared with experimental data [61]

The adiabatic effectiveness is obtained by the heat transfer computations in the next section. The definition of the adiabatic effectiveness is given by:

$$\varepsilon_{ad} = \frac{T_{ad} - T_a}{T_{ad}^{*} - T_a} \tag{5-5}$$

Here T_{ad}^{*} is the value of T_{ad} when there is no ingress and T_a is the temperature of the air in the annulus ($14.5^{\circ}C$). Figure 5-18 compares the radial distribution of ε_c and ε_{ad} on the rotor at a similar sealing flow rate (Φ_o). The figure indicates that both definitions of effectiveness provide almost identical distributions on the rotor at similar sealing flow rates. However, the computed adiabatic effectiveness still

over-predicts the measurement.

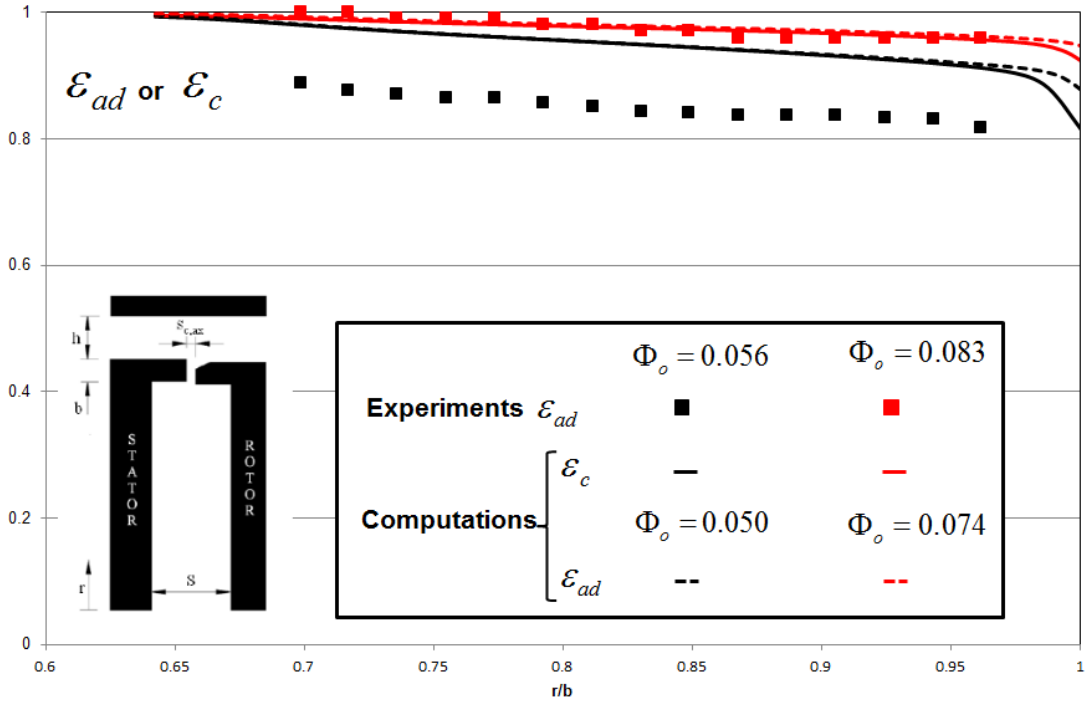

Figure 5-18 Comparison of radial distribution of ε_c and ε_{ad} on the rotor (symbols denote the experimental data [61])

5.5. **Heat transfer in the wheel-space**

Heat transfer computations also were carried out using the prescribed ingestion model for the axial-clearance seal. As discussed in the previous chapter, the temperature on the rotor surface slightly influences the Nusselt number and an accurate surface temperature distribution is difficult to obtain. Hence, for convenience, the heat transfer computations apply to a uniform surface temperature on the rotor. The temperature of the sealing flow is $57.5^{\circ}C$, which is same with the heat transfer experiments in University of Bath. In order to produce the heat flux on the rotor surface, a cool uniform surface temperature ($20^{\circ}C$) was adopted. At the same time, an adiabatic stator wall is used in these computations. The air temperature in the annulus is $14.5^{\circ}C$ for the experiments and computations. For the first computations, this temperature was used as the temperature of ingested flow. However, this

arrangement did not provide good agreement with experimental results. It is demonstrated that not only the swirl ratio but also the temperature is mixed when the ingested flow enters the wheel-space. Therefore, the mass-weighted average assumption also is adopted for the temperature:

$$T_i = \frac{\dot{m}_i T_a + \dot{m}_o T_o}{\dot{m}_i + \dot{m}_o} \tag{5-6}$$

Here T_a and T_o are the air temperature in the annulus ($14.5^\circ C$) and the temperature of the sealing flow ($57.5^\circ C$) respectively.

In Chapter 4, two different definitions of Nusselt number were used, based on two temperatures: $T_{w,ad}$ or T_{ref}. However, these definitions are deduced for the rotor-stator system without ingress and they cannot consider the influence of ingress on temperature in the wheel-space. Using these definitions unreasonable values of Nu were obtained in the computations. Therefore, the heat transfer computation in this chapter uses a simpler definition for Nusselt number:

$$Nu = \frac{qr}{k(T_s - T_{ad})} \tag{5-7}$$

Here q is the heat flux to the rotor, T_s is the surface temperature and T_{ad} is the adiabatic surface temperature. T_{ad} is gained by separate computations with an adiabatic rotor wall at the same fluid conditions (sealing flow rate and ingested flow rate). Figure 5-19 shows the computed and experimental measurements of adiabatic surface temperature. The experimental data [61] were obtained by the thermochromic liquid crystal (TLC) data based on the solution of the 1D Fourier equations for convective heat transfer. The computed adiabatic surface temperatures result directly from ANSYS CFX. The adiabatic computations provide reasonable values of T_{ad} and produce similar trends to the experiments. The computed T_{ad} is marginally higher than the experimental data.

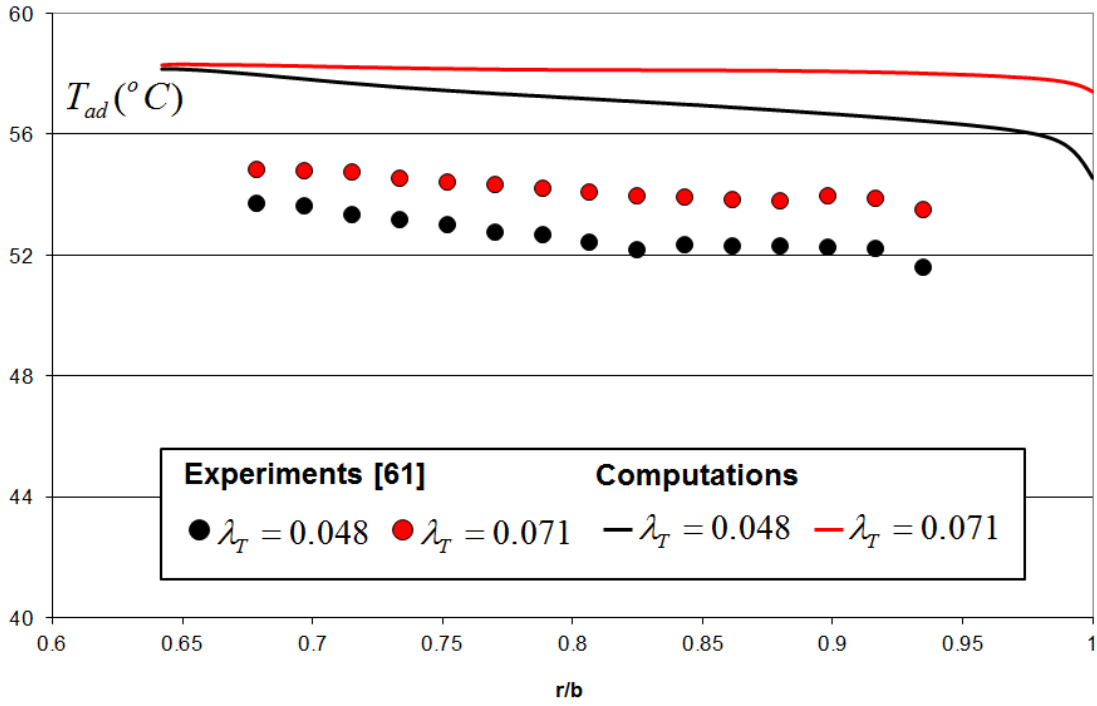

Figure 5-19 The computed T_{ad} compared with experimental data [61]

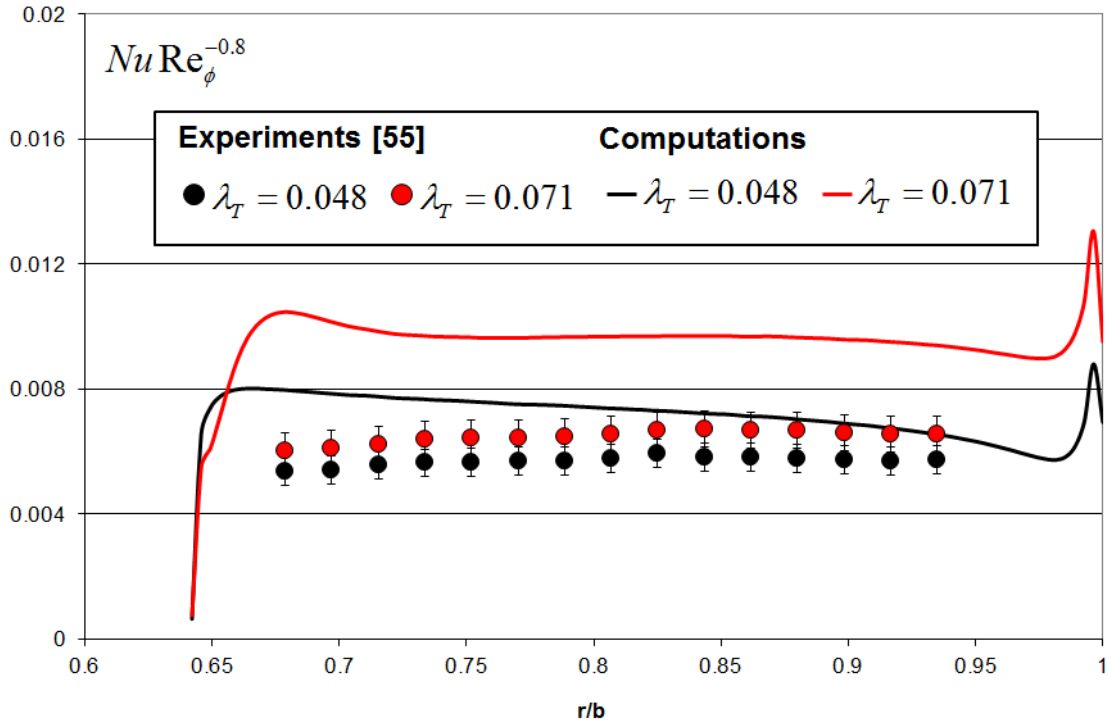

Figure 5-20 The radial variation of $Nu\,\mathrm{Re}_\phi^{-0.8}$ compared with experimental data [55]

In accordance with previous results for Nusselt number in Chapter 4, Figure 5-20 shows the computed variation of $Nu\,\mathrm{Re}_{\phi}^{-0.8}$ in comparison with the experimental data [55]. The experimental uncertainties are calculated by the method discussed in the literature [55]. Both the computations and the experimental data show that $Nu\,\mathrm{Re}_{\phi}^{-0.8}$ is almost invariant with the radius on the rotor, except in the region near the inlet and outlet. The computed results over-predict the experimental data, but capture qualitatively the main features of the experimental data. The main reason for the differences is the over-prediction of adiabatic surface temperature in Figure 5-19. As mentioned in Chapter 3, the radiation heat transfer is not included in the heat transfer model in the computations. Therefore, the effect of radiation heat transfer could be one reason of this over-prediction. Figure 5-20 also shows that Nu increases as λ_T, or sealing flow, increases and as ingested flow decreases. When ingress exists, the high swirl brought by ingested flow can increase the swirl ratio in the core and consequently reduce the Nusselt number.

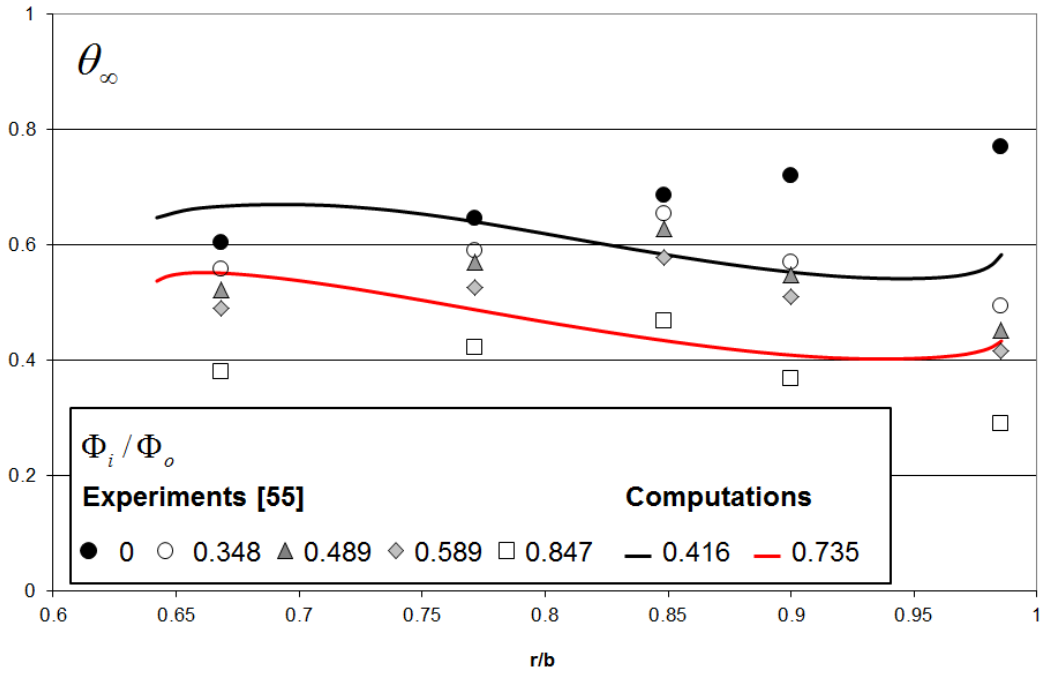

Figure 5-21 The radial variation of non-dimensional core temperature compared with experimental data [55]

The core temperature is an important feature for the heat transfer to the rotor. Figure 5-21 shows the radial variation of non-dimensional core temperature (θ_∞), which is defined by:

$$\theta_\infty = \frac{T_\infty - T_{in}}{T_o - T_{in}} \tag{5-8}$$

Here T_∞ is the air temperature at an axial distance of z/s=0.3 from the stator; this location is considered to be in the fluid core outside the boundary layer. T_{in} is the initial temperature of the air in a transient experiment. In the computation, the temperature of the rotor ($20^\circ C$) is used as T_{in}. Figure 5-21 shows that for both the computations and the experimental data [55], when ingress occurs and the cold ingested air reduced the core temperature at high radius. The computed core temperatures are higher than the experimental data. It should be noted that the core temperatures are also influenced by the heat transfer to the stator. The thermal conditions on the stator for the computations and the experiments are quite different. Despite this, θ_∞ has been reasonably predicted by the computations.

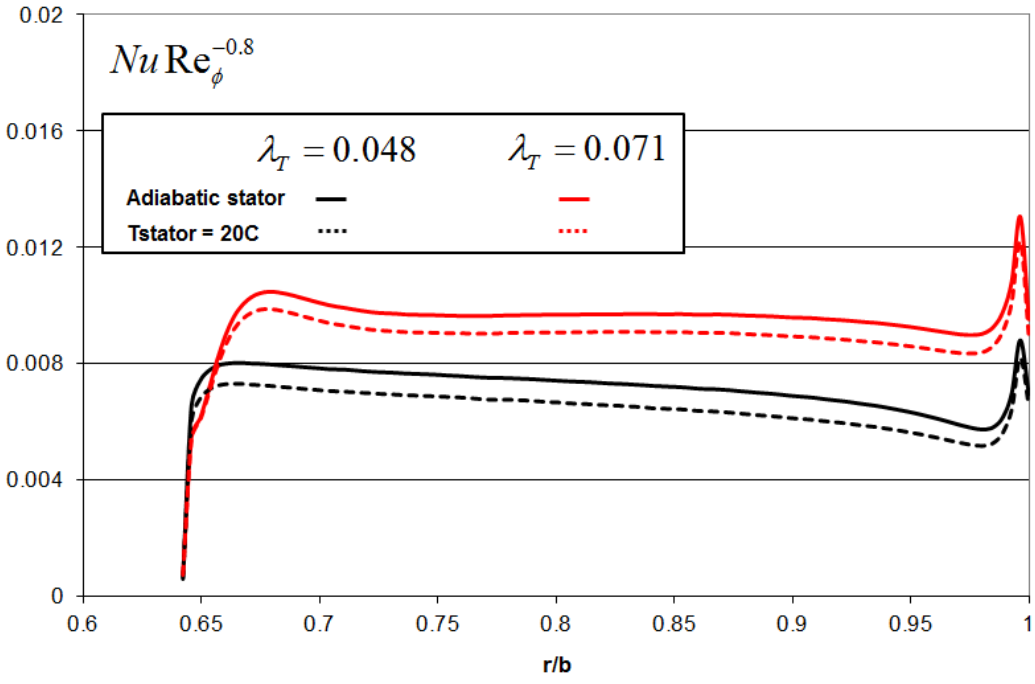

Figure 5-22 The computed radial variation of $Nu\,\mathrm{Re}_\phi^{-0.8}$ including stator heat transfer

Generally, the influence of heat transfer to the stator on the rotor Nusselt number is thought to be very small [19]. However, in order to study the effect of stator heat transfer, computations have been conducted with the stator at the same temperature as the rotor ($20^{\circ}C$). Figure 5-22 shows the effect of stator heat transfer on the radial variation of $Nu\,\mathrm{Re}_{\phi}^{-0.8}$ on the rotor. According to the figure, the stator heat transfer can reduce Nu, but the effect is minor. This is in accordance with 3D results presented by Javiya *et al.* [19].

5.6. Chapter summary

In summary, the prescribed ingestion model applied to the axial-clearance seal gives reasonable results for fluid dynamics, sealing effectiveness and heat transfer in comparison with the experimental data. The radial variation of effectiveness on the stator from this 2D model is similar to published 3D simulations [42]. The agreement between computed and measured heat transfer is fair, and these heat transfer tests have not previously been studied computationally. The 2D model has the significant advantage of reduced complexity and computational costs, with each computation approximately 10 hours. In the next chapter, this prescribed ingestion model is applied to other seal geometries.

6. Prescribed ingestion model: other seal geometries

Following development of the prescribed ingestion model for the axial-clearance seal, this chapter presents prescribed ingestion model results for three other seal geometries: a radial-clearance seal, a double axial-clearance seal and a radial-axial-clearance seal. The experimental geometries and computational models for these three seals are shown in Figure 6-1. As with the axial-clearance seal, the mass-weighted average assumption is used for ingress boundary conditions and the position of the ingress inlet and egress outlet also are as shown in the figure for the three models. The egress outlet is located at the rotor side of the axial overlap piece for the radial-clearance and radial-axial-clearance seals. These models contain around 40000 mesh cells. The fluid dynamics in the wheel-space and sealing effectiveness are studied for each seal and the seal performance of all geometries is compared. The computations were carried out at two rotational Reynolds numbers (Re_ϕ), which are 5.32×10^5 and 8.17×10^5.

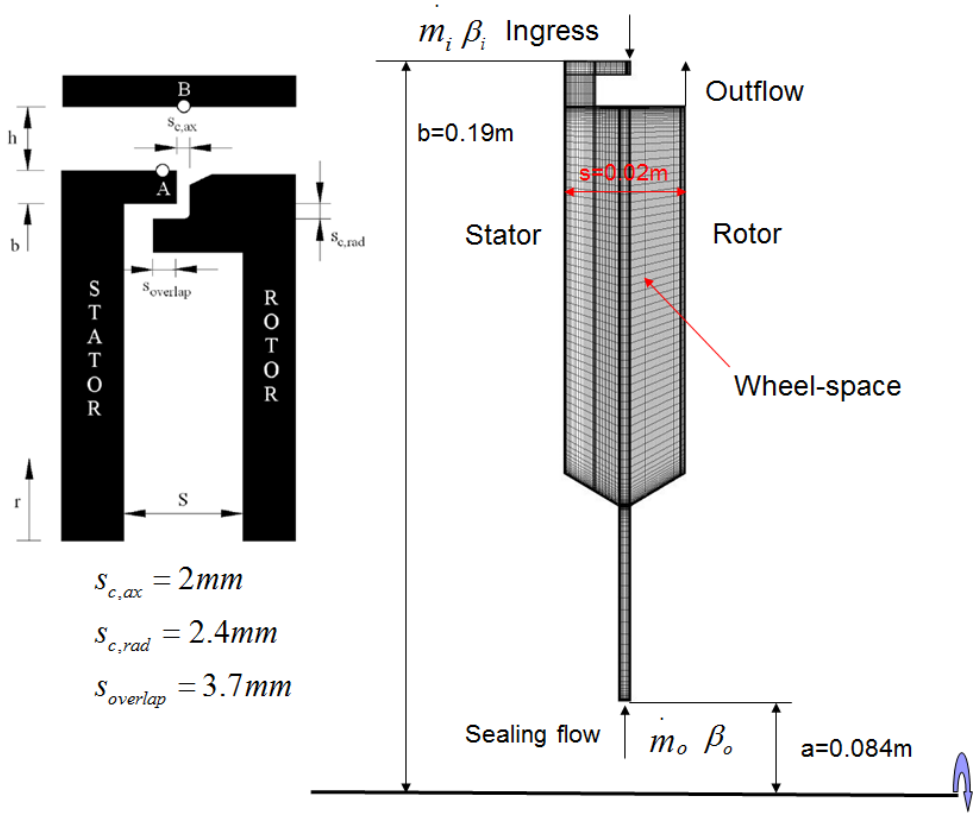

(a)

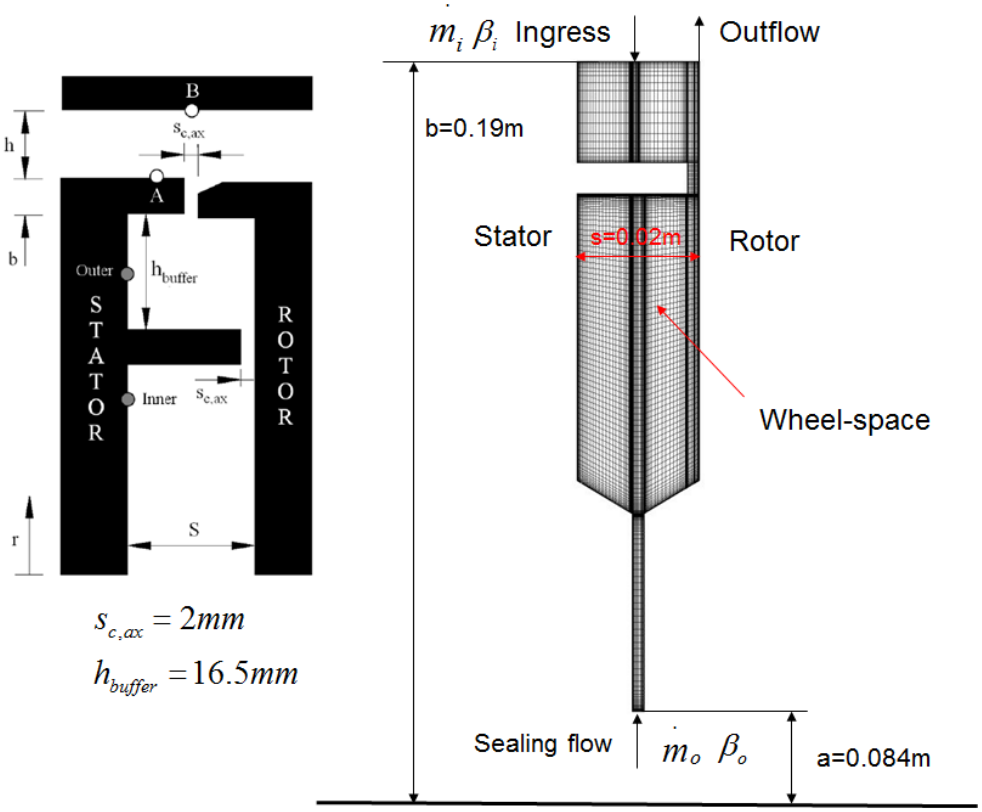

(b)

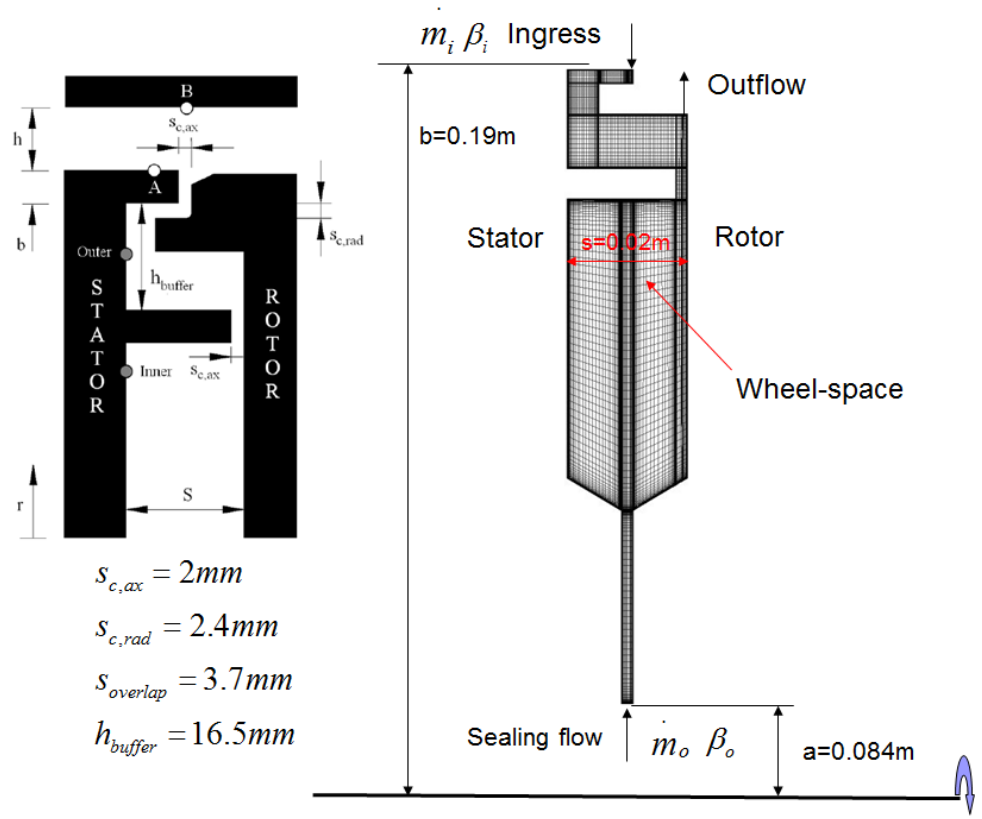

(c)

Figure 6-1 The experimental rigs [60] and computational models for (a) Radial-clearance seal (b) Double axial-clearance seal (c) Radial-axial-clearance seal

6.1. **Radial-clearance seal**

The radial-clearance seal (Figure 6-1 (a)) is a generic seal geometry, with an axial overlap piece on the rotating disc compared with the axial-clearance seal. The literature [51] shows this seal geometry has better performance than the axial clearance seal. The egress outlet is positioned at the base of the axial overlap piece at the rotor surface. The boundary surface of the axial overlap rotates with rotor. The computational parameters for the radial-clearance seal are shown in Table 6-1. The value of Φ_i is deduced using the experimental data for the radial-clearance seal [54], shown in Figure 6-2. The computations at the higher Re_ϕ were carried out for comparison with measured values of swirl ratio. The lower Re_ϕ computations were carried out to compare measured and computed distributions of sealing effectiveness.

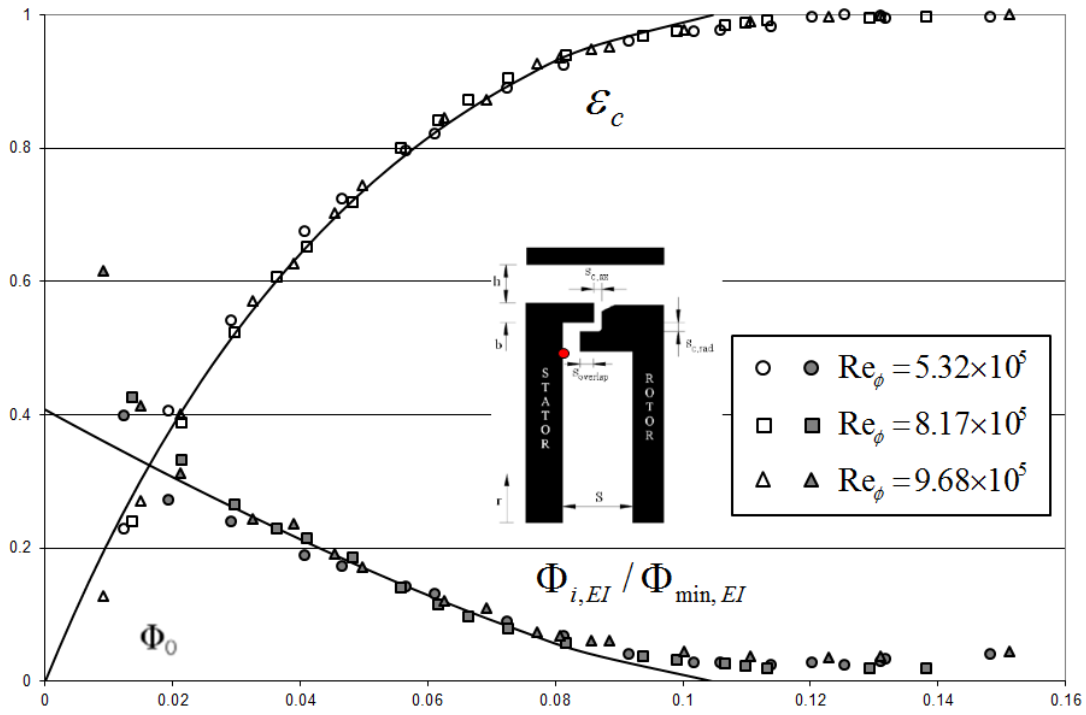

Figure 6-2 Experimental data for radial-clearance seal with EI ingress [54]

Re_ϕ	$C_{w,o}$	Φ_o	λ_T	Φ_i
8.17×10^5	966	0.0188	0.018	0.0328
	1932	0.0376	0.036	0.0233
	3918	0.0763	0.073	0.0075
5.32×10^5	1030	0.0308	0.027	0.0266
	1598	0.0478	0.042	0.0187
	2444	0.0731	0.064	0.0085

Table 6-1 Computational parameters for the radial-clearance seal

Figure 6-3 shows the swirl ratio distribution at z/s=0.25 in the wheel-space for the radial-clearance seal. Closed symbols denote the experimental data [60]. The open square symbols shown at r/b=1 denote the ingress swirl ratio ($\beta_{i,mass}$) boundary condition calculated using the mass-weighted average assumption. The computed swirl is in reasonably good agreement with the experimental data, again showing that the mass-weighted average assumption provides a reasonable estimate for the swirl ratio for the ingested flow entering the wheel-space.

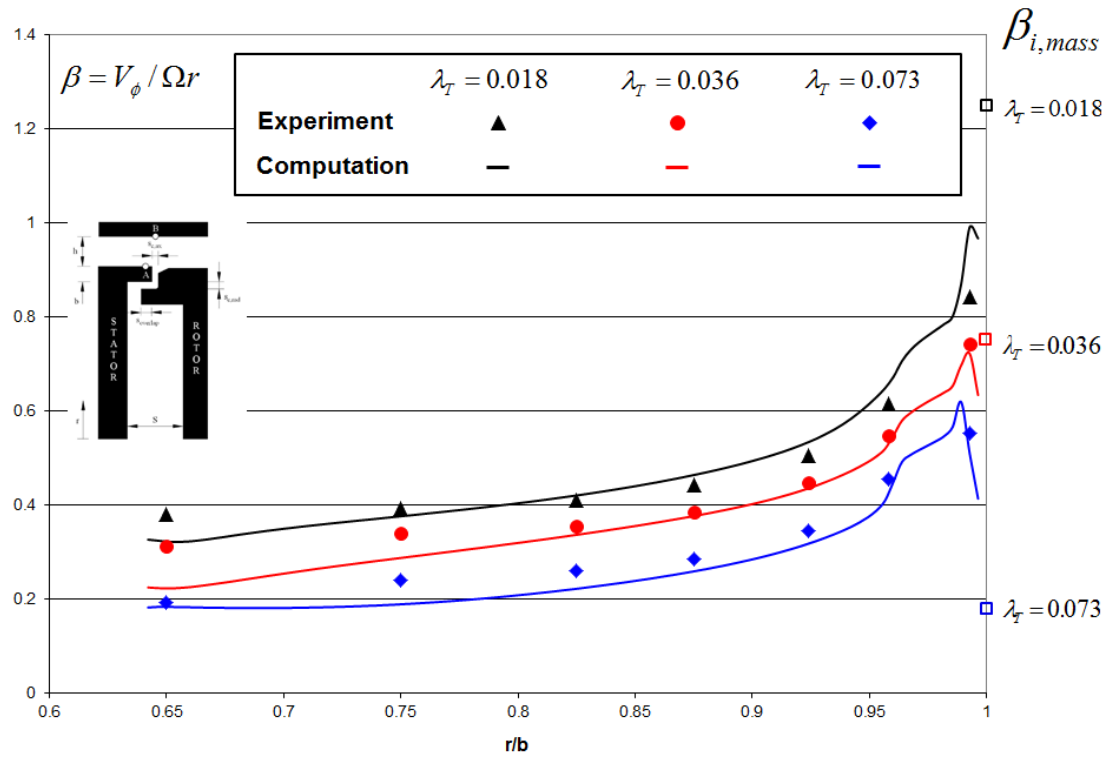

Figure 6-3 Swirl ratio distribution for radial-clearance seal, z/s=0.25 (symbols denote the experimental data [60])

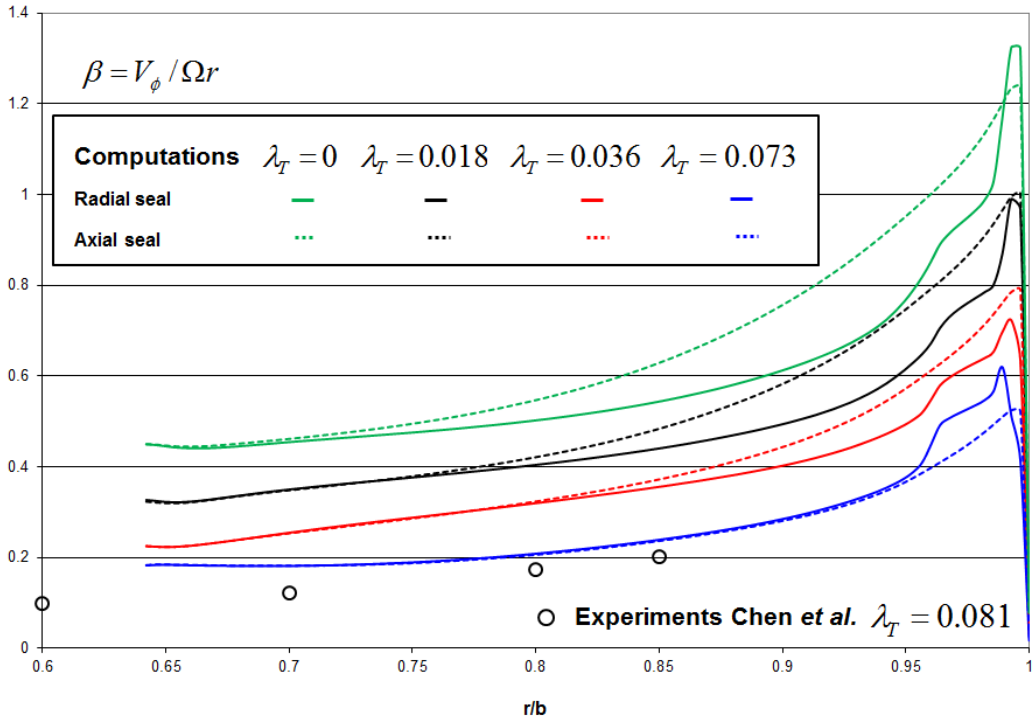

Figure 6-4 Swirl ratio distribution for radial-clearance and axial-clearance seal, z/s =0.25

Figure 6-4 shows swirl ratio distributions (at z/s =0.25) for the radial-clearance and axial-clearance seals at the three values of λ_T, together with computed results for zero sealing flow ($\lambda_T = 0$). Experimental results from Chen *et al.* [8] are shown as open symbols in this figure. Generally, at the same sealing flow rate (λ_T), the swirl ratio is higher at high radius for the axial-clearance seal than for the radial-clearance seal, since a greater amount of ingested flow with higher swirl at inlet occurs for the axial-clearance seal. The difference between the results for the two seals reduces as sealing flow rate increases and the effects of ingress weaken. For $\lambda_T = 0.073$, the swirl distribution is almost the same for the two seals and is close to the experimental results of Chen *et al.* for a similar value of λ_T (=0.081). For the radial-clearance seal, the edge of the rotating axial overlap (z/s =0.265) is close to the z/s =0.25 location and there is a rapid increase in swirl ratio at high radius near r/b =1 for each λ_T. At low radius, there is little difference between the results for the two seals. Therefore, it can be concluded that the flow structure in the wheel-space at relatively low radius is governed mainly by λ_T and the seal geometry only influences the flow in the outer

region of wheel-space.

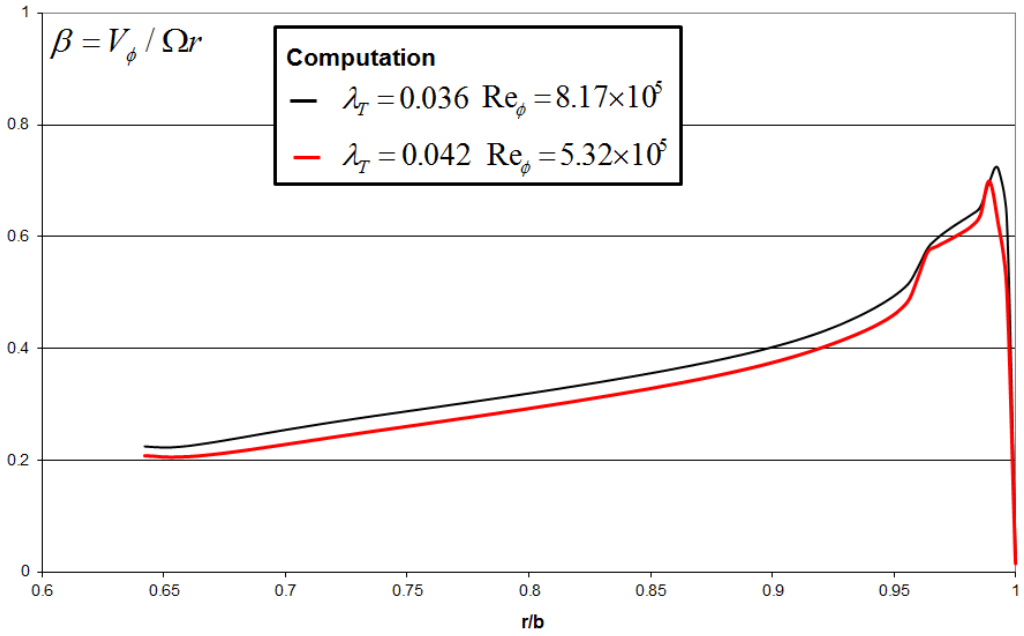

Figure 6-5 Comparison of swirl distribution for different rotational speed for the radial-clearance seal at similar λ_T

Similar to the axial-clearance seal, Figure 6-5 shows the swirl distribution at different Re_ϕ for broadly similar values of λ_T for the radial-clearance seal. This result illustrates again that Re_ϕ has no significant effect on the distribution of swirl ratio and that λ_T is the dominant factor for the flow structure in the wheel-space.

The sealing effectiveness is the main measure of the performance for each rim-seal geometry. In Chapter 5, it was shown proved that the variation of sealing effectiveness with Φ_o is independent of Re_ϕ. Hence, in this chapter, the variation of sealing effectiveness with Φ_o is investigated for other seal geometries. Figure 6-6 shows the computed and measured variation of sealing effectiveness with Φ_o for the radial-clearance seal. Computed results for the axial-clearance seal are also included. In the figure, the open symbols denote the experimental data for the radial-clearance seal [54], the closed symbols denote the computed effectiveness (black: radial-clearance seal, grey: axial-clearance seal) and the line [54] is the orifice model theoretical curve fitted to the experimental data. For the radial-clearance seal, the

computed effectiveness shows better agreement with the experimental data and the theoretical curve than that for the axial-clearance seal (in Figure 5-15), where some of the ingested flow migrated directly to the outlet in axial-clearance seal model. For the radial-clearance seal, all of the ingested flow enters the boundary layer on the stator due to the location of the outlet in the prescribed ingestion model. Hence, the ingested flow can fully influence the computed effectiveness in the boundary layer on the stator and consequently better agreement with the measurements is obtained for the radial-clearance seal. The computed secondary flow streamlines for both seal geometries at the same sealing flow rate are show in Figure 6-7. It is clear that almost no difference exists at low radius and differences only emerge at high radius (near the seal region). The different flow paths of the ingested fluid are also shown by the streamlines. At the same sealing flow rate (Φ_o), the boundary condition setting of the ingress inlet for the radial-clearance seal gives higher sealing effectiveness than that for the axial-clearance seal due to the better performance of the radial-clearance seal. This leads to the higher effectiveness for the radial-clearance seal in Figure 6-6 at the same value of Φ_o.

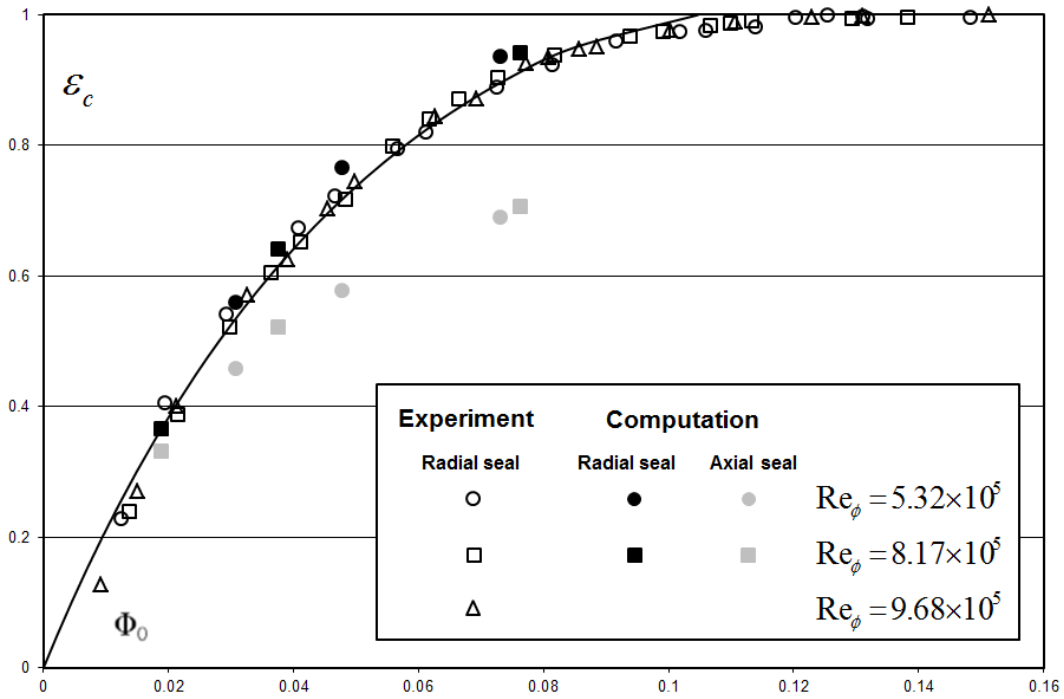

Figure 6-6 The computed variation of effectiveness with Φ_o for radial-clearance seal compare with axial-clearance seal (open symbols denote the experimental data [54])

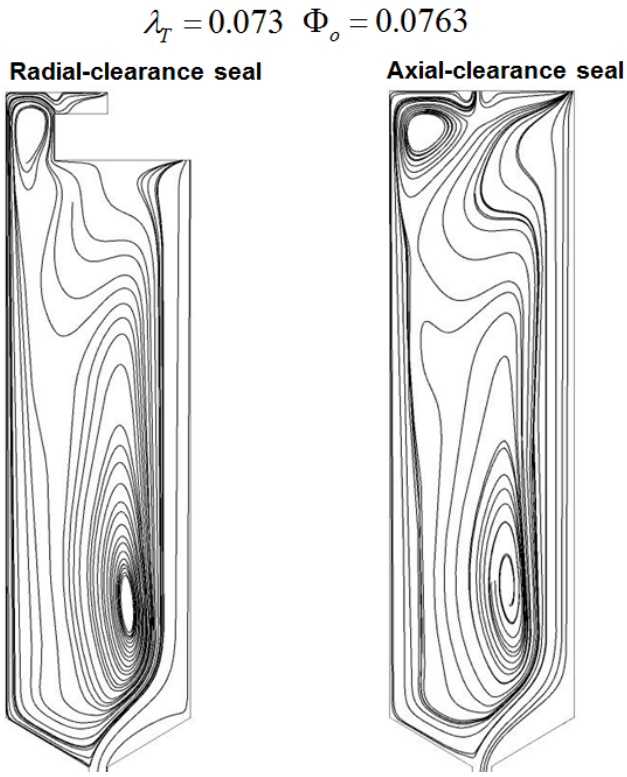

Figure 6-7 The computed streamlines for both seal geometries, $\lambda_T = 0.073$

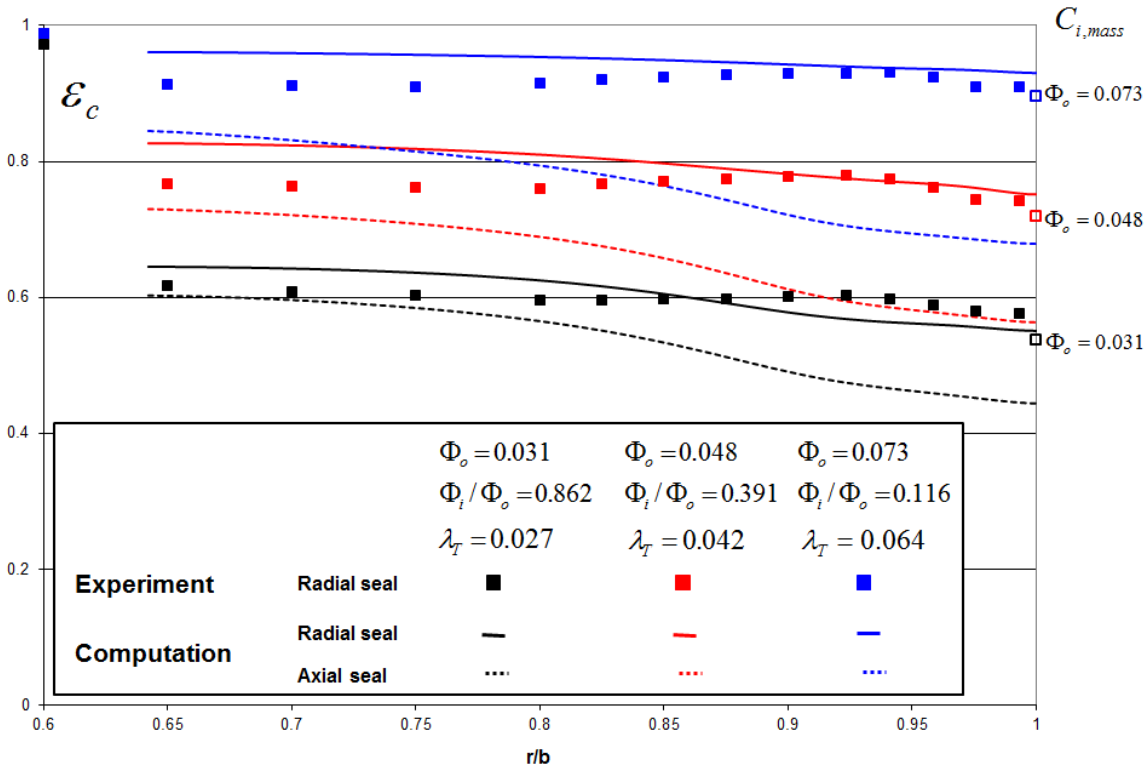

Figure 6-8 The radial distribution of effectiveness on the stator for the radial-clearance and axial-clearance seals (symbols denote the experimental data [60])

Figure 6-8 shows the radial distribution of sealing effectiveness on the stator for both radial- and axial-clearance seal geometries at the same value of λ_T, together with the experimental data for the radial-clearance seal [60]. The open square symbols shown at r/b=1 denote the ingress concentration ($C_{i,mass}$) boundary condition calculated using the mass-weighted average assumption for the radial-clearance seal. Similar to the variation of sealing effectiveness with Φ_o, the computed results for the radial-clearance seal show reasonably good agreement with the experimental data. The computed results also show that the effectiveness is almost invariant with radius. For the corresponding axial-clearance seal results, there is lower sealing effectiveness as noted previously and the variation with radius is greater than for the radial-clearance seal. For the radial-clearance seal, mixing is confined to a region very close to the inlet, as illustrated in the streamlines (Figure 6-7).

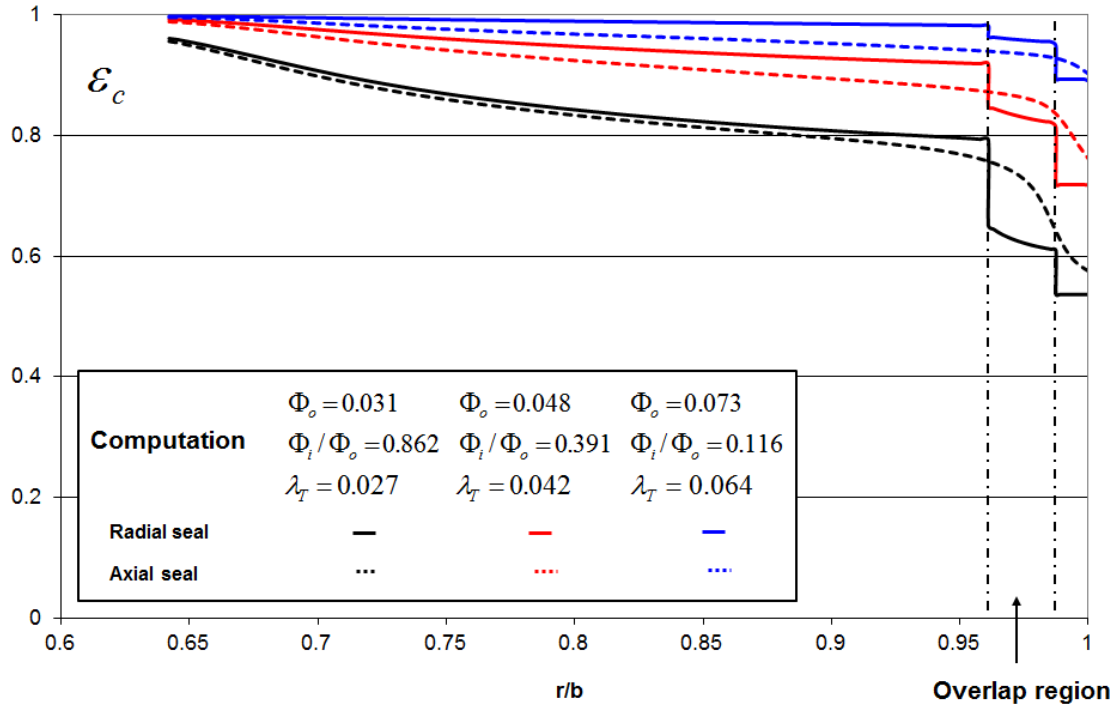

Figure 6-9 The radial distribution of effectiveness on the rotor surface for the radial-clearance and axial-clearance seals

Due to absence of experimental data for the rotor, Figure 6-9 shows only the computed radial distribution of sealing effectiveness on the rotor for both radial- and

axial-clearance seal geometries at the same value of λ_T. The vertical dashed lines illustrate the overlap region for the radial-clearance seal. Compared with the effectiveness on the stator, smaller differences exist on rotor between the two seal geometries. For the radial-clearance seal, the step change in effectiveness values shown at high radius are due to the axial overlap surfaces of the seal.

6.2. **Double axial-clearance seal**

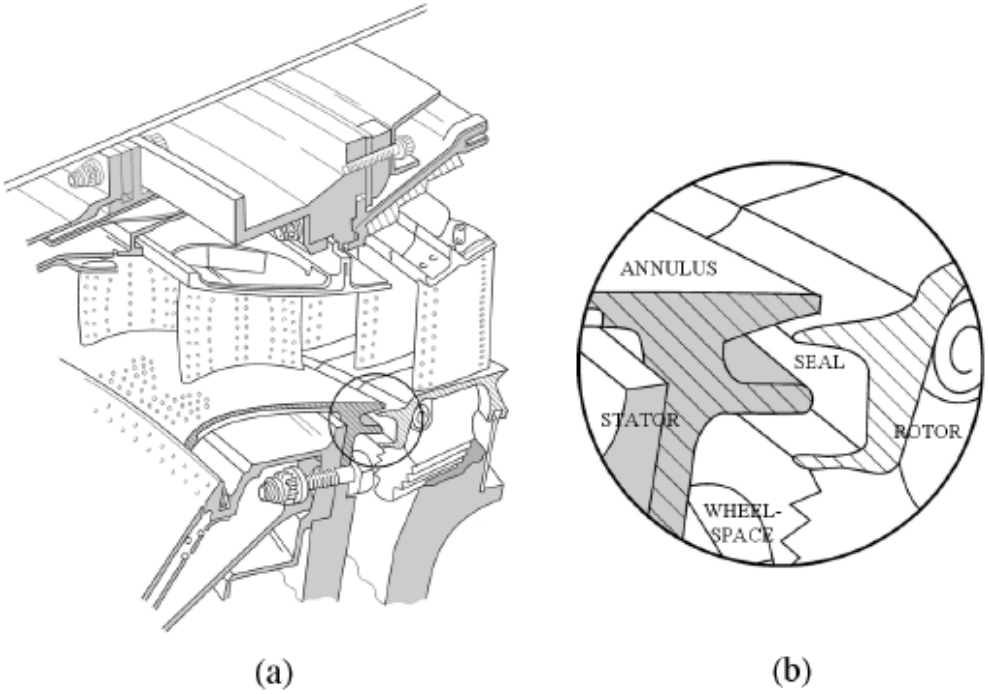

Figure 6-10 (a) Typical high-pressure gas turbine stage of a Rolls-Royce jet engine; (b) detail of rim seal [6]

Double-clearance rim-seals are used in typical turbine stages of engines, as illustrated in Figure 6-10. This section and the next section evaluate the prescribed ingestion method for double-clearance seal geometries. The double axial-clearance, which features axial-clearances for both outer and inner seals (Figure 6-1 (b)), is presented in this section. The wheel-space is separated into an outer and an inner wheel-space by the inner axial-clearance seal. The mass-weighted average assumption is applied for boundary conditions as before and the location of the egress outlet is the same as for

the single axial-clearance seal, shown in Figure 6-1 (b). The computed results for the double axial-clearance are compared with those for the single axial-clearance seal. The computational parameters for this seal geometry are shown in Table 6-2. The value of Φ_i is deduced from the experimental data for the double axial-clearance seal [54], shown in Figure 6-11. The computations at the higher rotational speed are carried out for compare with measurements of swirl ratio and the lower rotational speed for comparison with measured radial variations of sealing effectiveness.

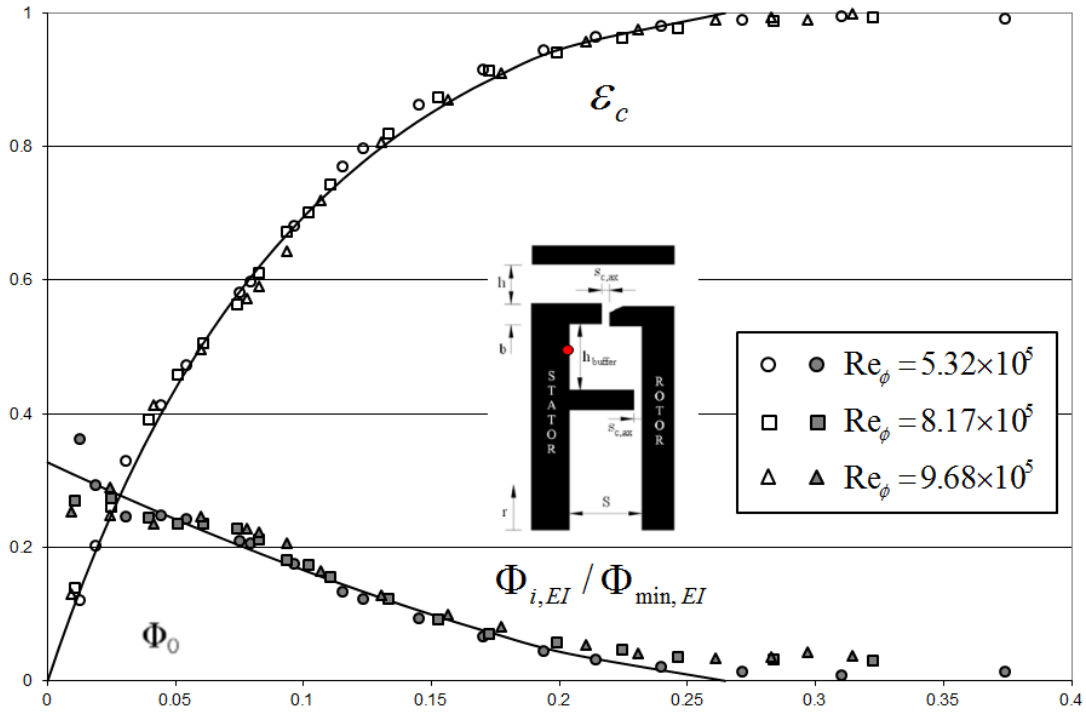

Figure 6-11 Experimental data for double axial-clearance seal with EI ingress [54]

Re_ϕ	$C_{w,o}$	Φ_o	λ_T	Φ_i
8.17×10^5	3060	0.0596	0.057	0.0606
	5934	0.1156	0.111	0.0375
	11969	0.2332	0.223	0.0048
5.32×10^5	737	0.0221	0.019	0.0779
	2018	0.0604	0.053	0.0597
	2993	0.0895	0.079	0.0481

Table 6-2 Computational parameters for the double axial-clearance seal

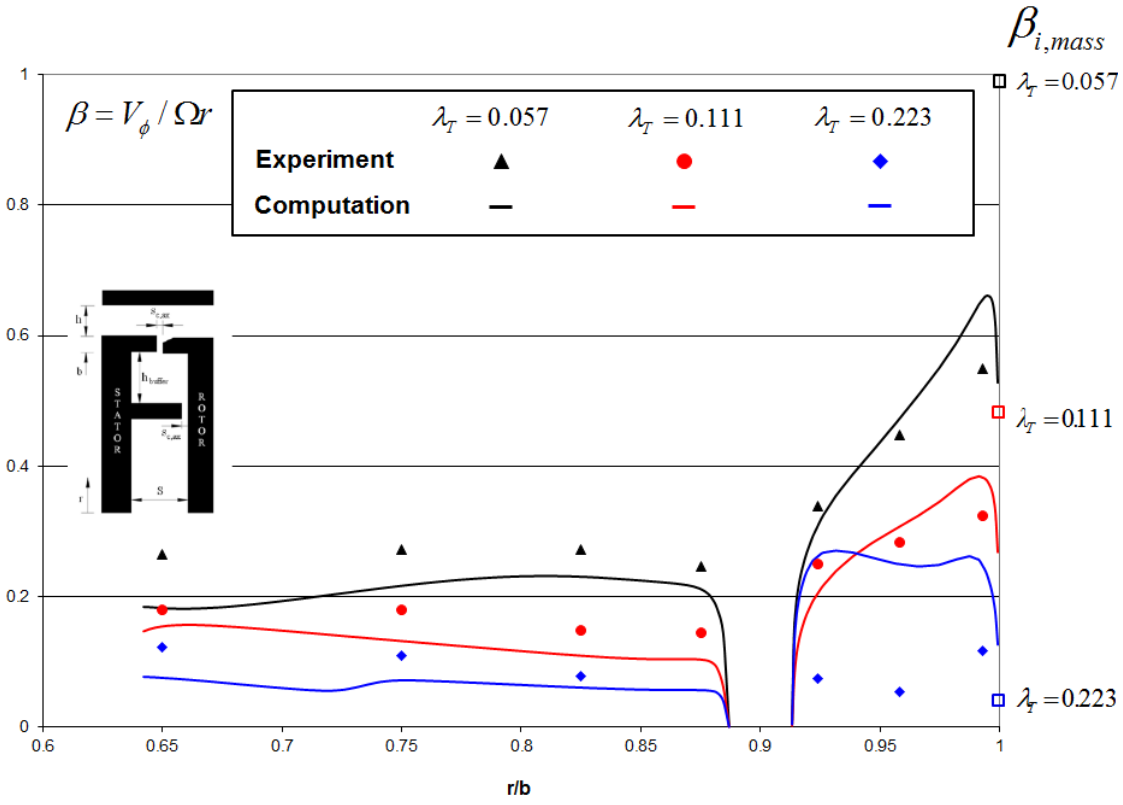

Figure 6-12 Swirl ratio distribution for double axial-clearance seal, z/s =0.25 (symbols denote the experimental data [60])

Figure 6-12 shows the swirl ratio distribution at z/s =0.25 in the wheel-space for the double axial-clearance seal. The closed symbols denote the experimental data [60]. The open square symbols at r/b =1 denote the ingress swirl ratio ($\beta_{i,mass}$) used as the boundary condition calculated with the mass-weighted average assumption. Generally, the computed results have reasonable agreement with the experimental data in both the outer and inner wheel-space. At the highest value of λ_T (=0.223), the computed swirl ratio is higher than the measurements in the outer wheel-space. This was also true for the single axial-clearance seal (Figure 5-7 (c)), and the reason for the over-prediction is the same. The rotating boundary between the ingress inlet and egress outlet influences the swirl ratio of the ingested flow around the ingress inlet region, and this influence continues for the ingested flow in the wheel-space. The swirl ratio contours and secondary flow streamlines for the outer wheel-space for $\lambda_T = 0.223$ are shown in Figure 6-13 with a fine scale. The figure illustrates the effect of the rotating shroud on the swirl ratio in the outer wheel-space. For the single

seal, the effect is extended over the full wheel-space, but the effect is greater in the confined outer wheel-space for the double axial-clearance seal.

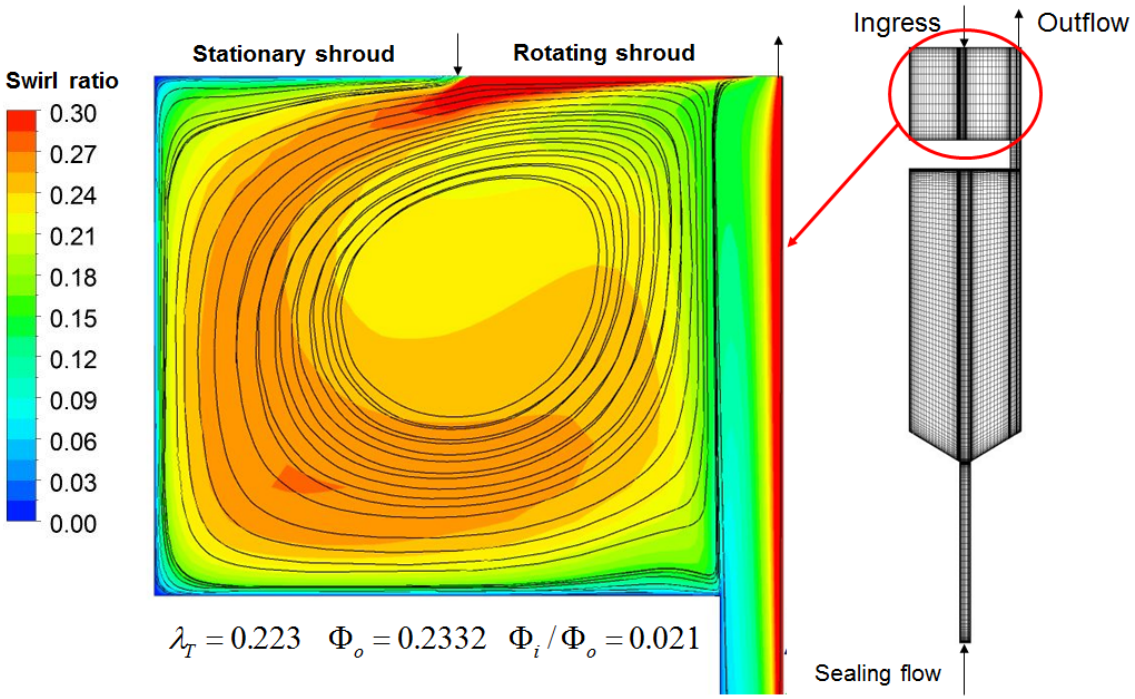

Figure 6-13 Swirl contour and flow streamlines in outer wheel-space for the double axial-clearance, $\lambda_T = 0.223$

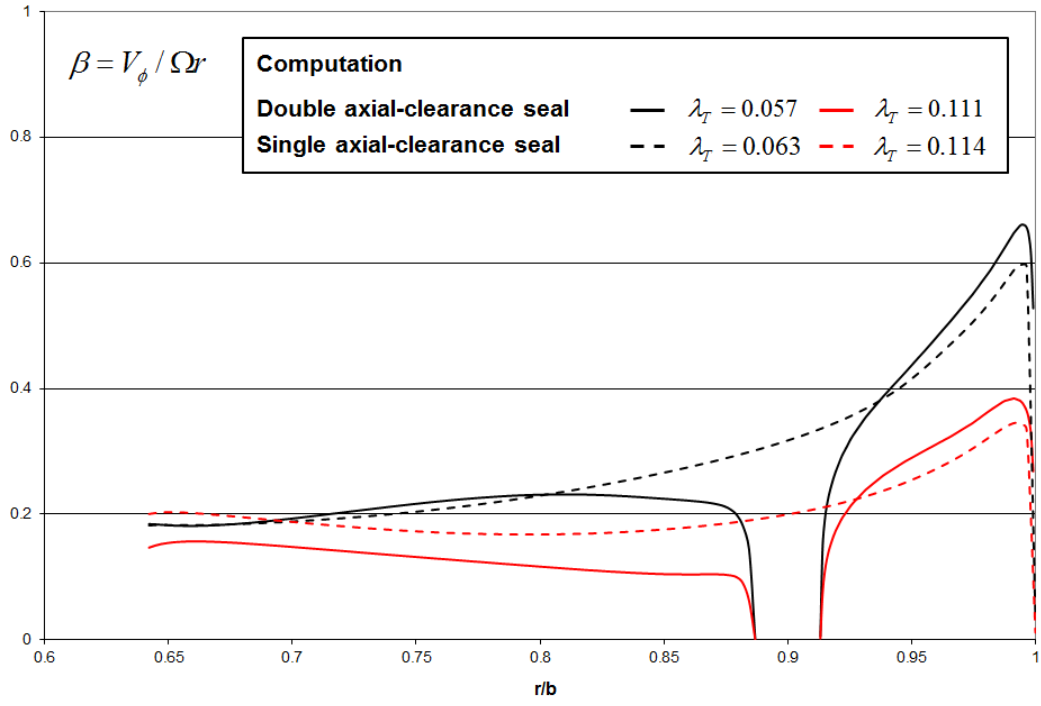

Figure 6-14 Swirl ratio distribution for double and single axial-clearance seal, z/s =0.25

Figure 6-14 shows a comparison of the distribution of swirl ratio for the single axial-seal and the double axial-clearance seal at a similar sealing flow rate. Generally, the difference between the seal geometries is small at low and high radius. A reduction in swirl ratio occurs for the double axial-clearance seal due to the inner seal insert. The flow structure is mainly controlled by λ_T .

Two sampling points for sealing effectiveness are used for the double axial-clearance seal. One is in the outer wheel-space at r/b=0.958 and the second is in the inner wheel-space at r/b=0.85. The definitions of sealing effectiveness at the two sampling points are same as that for single seals, as shown in Chapter 3.

$$\varepsilon_c = \frac{c - c_a}{c_o - c_a} \tag{6-1}$$

The effectiveness is collected at r/b=0.958 for single seals. For consistency, the outer sampling point (r/b=0.958) is used for the comparison of the outer seal with that of the single seals and the inner sampling point (r/b=0.85) is used for comparison between different double seals.

Figure 6-15 (a) and (b) show the computed and measured variation of sealing effectiveness with Φ_o for the outer and inner sampling points for the double axial-clearance seal. In the figures, the open symbols denote the experimental data [54]; the closed symbols denote the computed effectiveness and the lines are the theoretical curves [54] for this seal geometry. For the outer sampling point, the computed sealing effectiveness has good agreement with the experimental data and the theoretical curve. There is a slight over-prediction of effectiveness at lower sealing flow rates for the computations. However, for the inner sampling point, the computations over-predict the effectiveness. Both computations and measurements show that the effectiveness is higher at the inner than at the outer sampling point at same value of Φ_o .

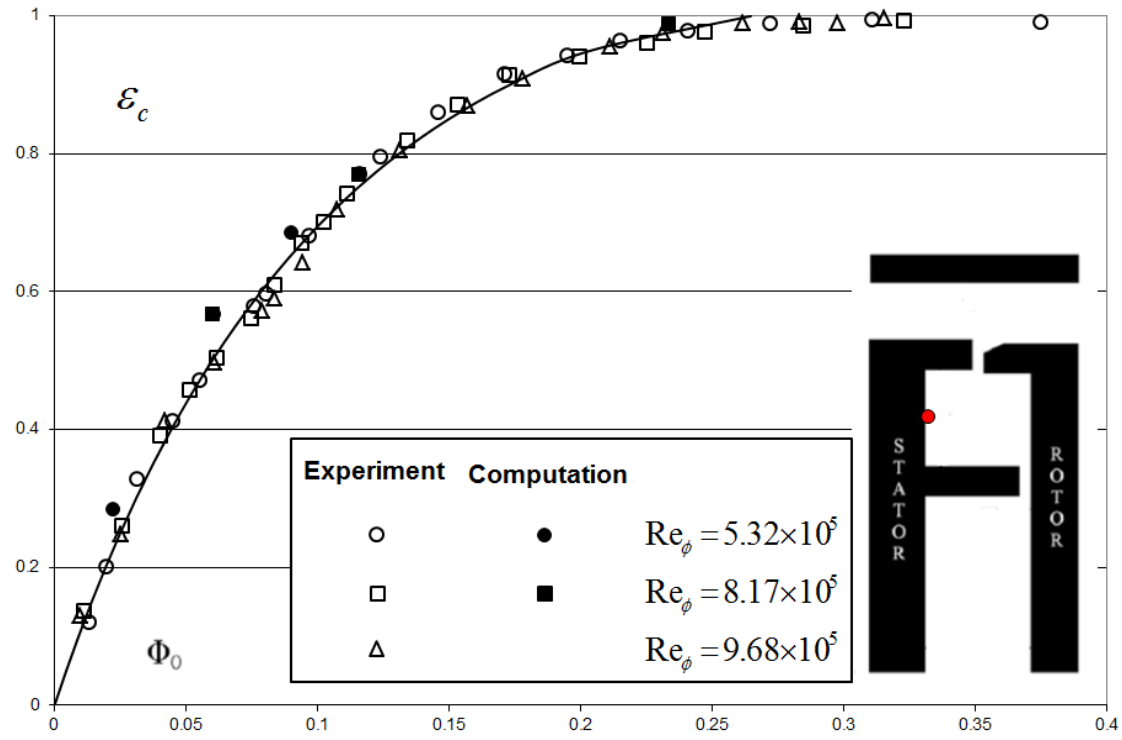

(a)

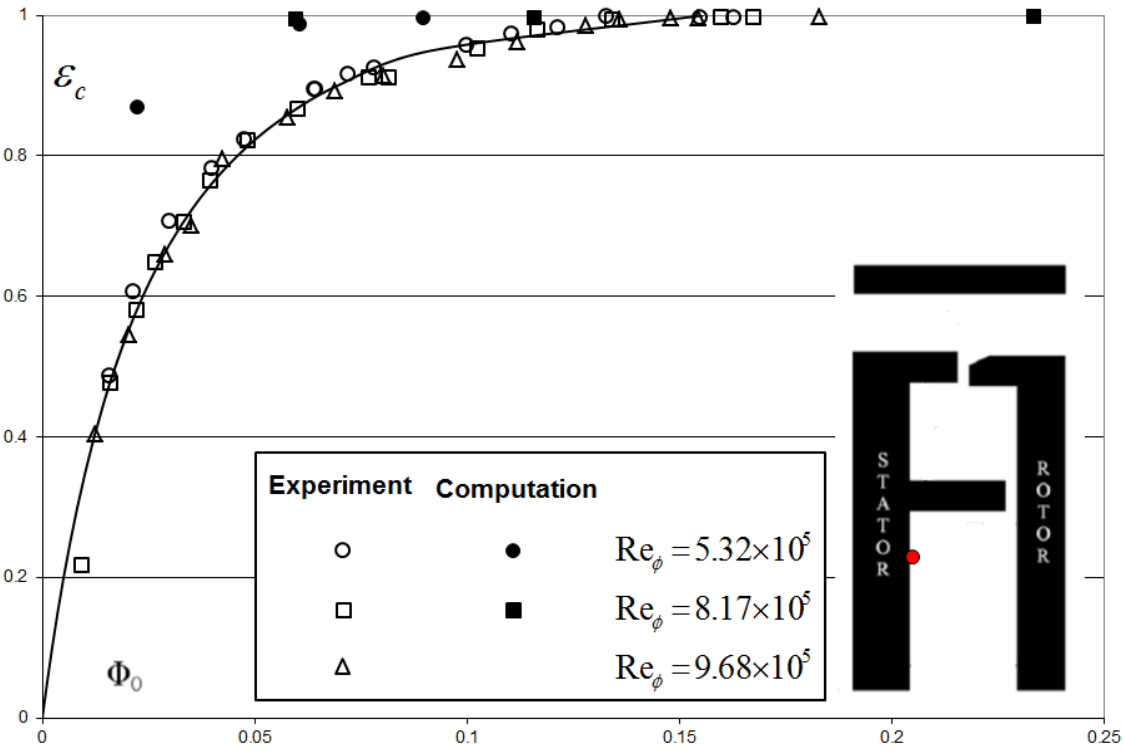

(b)

Figure 6-15 The computed variation of effectiveness with Φ_o for the double axial-clearance seal for (a) the outer sampling point and (b) the inner sampling point (symbols denote the experimental data [54])

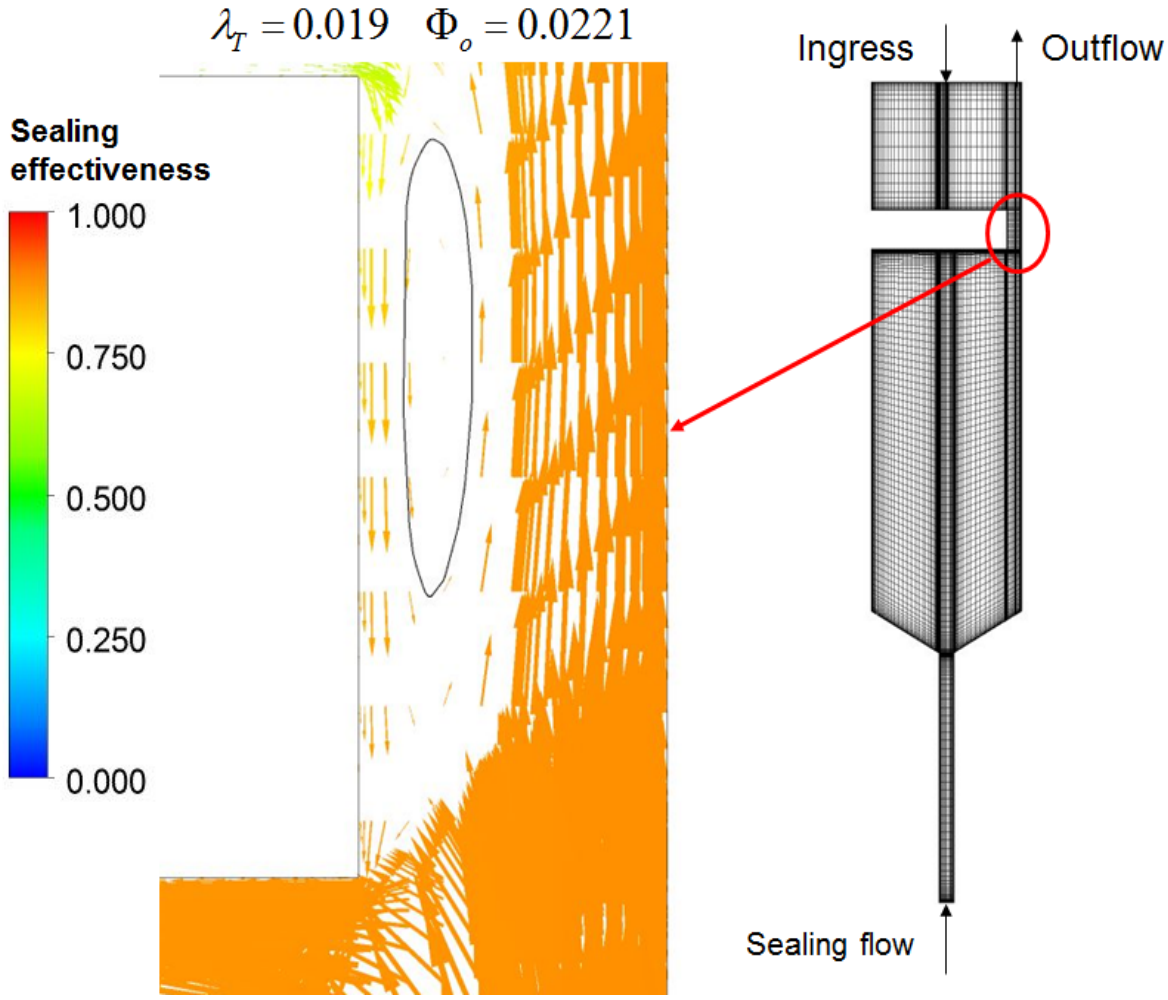

Figure 6-16 Velocity vectors and sealing effectiveness around the inner seal region for the double axial-clearance seal, $\lambda_T = 0.019$

The over-prediction of effectiveness at the inner sampling point is due to blocking of the flow at the inner seal region. Velocity vectors around the inner seal region for the double axial-clearance seal, shown in Figure 6-16, illustrate the secondary flow structure. At the base of the inner seal clearance, most of the inward flow is prevented from entering the inner wheel-space by the strong sealing flow and a recirculation in the seal clearance (the black line in Figure 6-16). Although ingestion in the inner wheel-space is under-predicted, the outer wheel-space is the more important region of interest for engine designers, and, the prescribed ingestion model for the double-clearance seal gives reasonable prediction of effectiveness in the outer wheel-space.

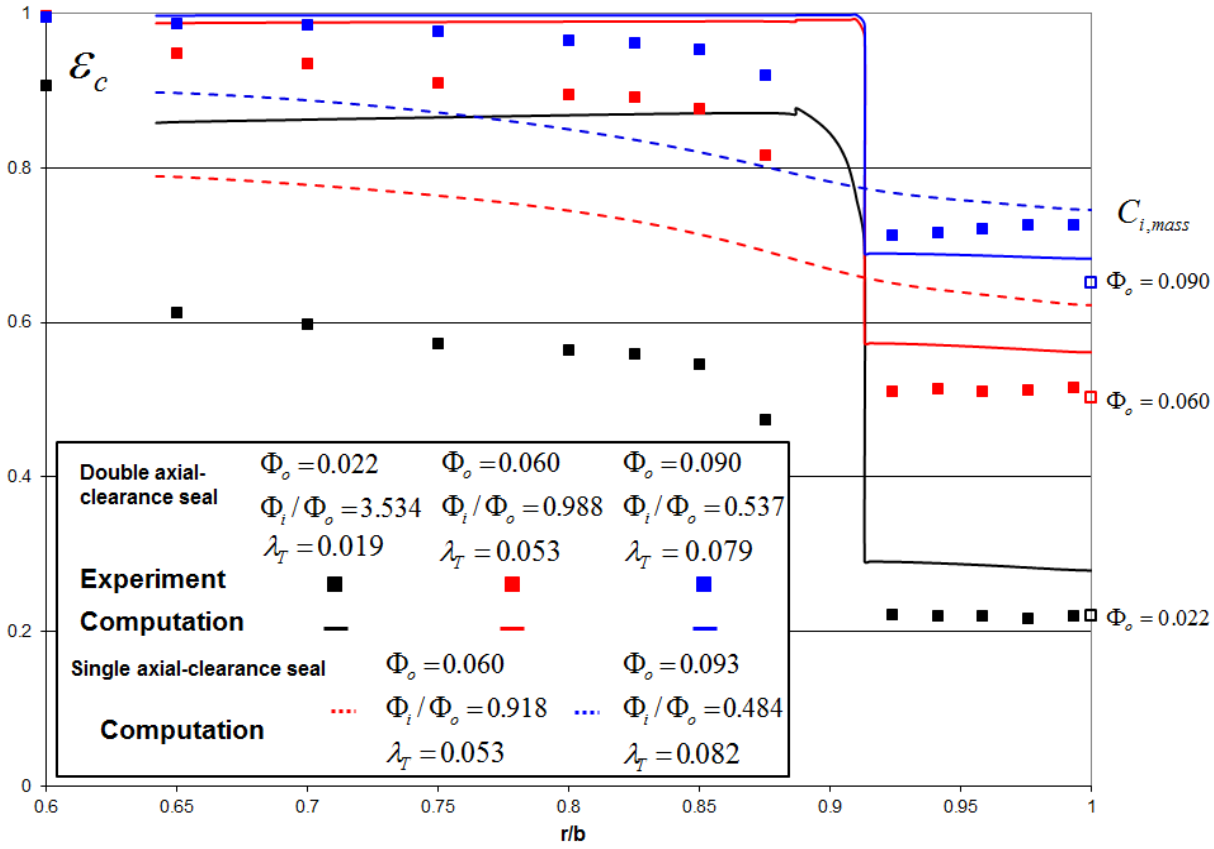

Figure 6-17 The radial distribution of effectiveness on stator for the double axial-clearance and single axial-clearance seals (symbols denote the experimental data [60])

Figure 6-17 shows the radial distribution of sealing effectiveness on the stator for the double and single axial-clearance seals at similar conditions. The experimental data for the double axial-clearance seal [60] are also shown. The open square symbols shown at $r/b=1$ denote the ingress concentration ($C_{i,mass}$) boundary condition calculated using the mass-weighted average assumption for the double axial-clearance seal. For the double axial-clearance seal, both computations and experiment show a significant increase in sealing effectiveness across the inner seal clearance. The computations again over-predict the effectiveness. In the outer wheel-space ($r/b>0.9$), the computed effectiveness has a reasonable level compared with the experimental data. For similar conditions, both seal geometries give the similar effectiveness level in outer wheel-space, which means that the performance of the outer seal for the double axial-clearance seal is close to that of the single axial-clearance seal. These results suggest that a better estimate of $C_{i,mass}$ may be needed for the prediction of effectiveness in the outer seal region for this

configuration.

6.3. **Radial-axial-clearance seal**

The radial-axial-clearance seal has a radial-clearance outer seal and an axial-clearance inner seal (Figure 6-1 (c)). The mass-weighted average assumption is used and the location of egress outlet is same as for the single radial-clearance seal, see Figure 6-1 (c). The computational parameters for this seal geometry are shown in Table 6-3. The value of Φ_i is deduced from experimental data for the radial-axial-clearance seal [60], shown in Figure 6-18. The computations at the higher value of Re_ϕ are carried out for comparison with measured swirl ratios. The computations at the lower values of Re_ϕ are carried out for comparison with measured radial variations of sealing effectiveness.

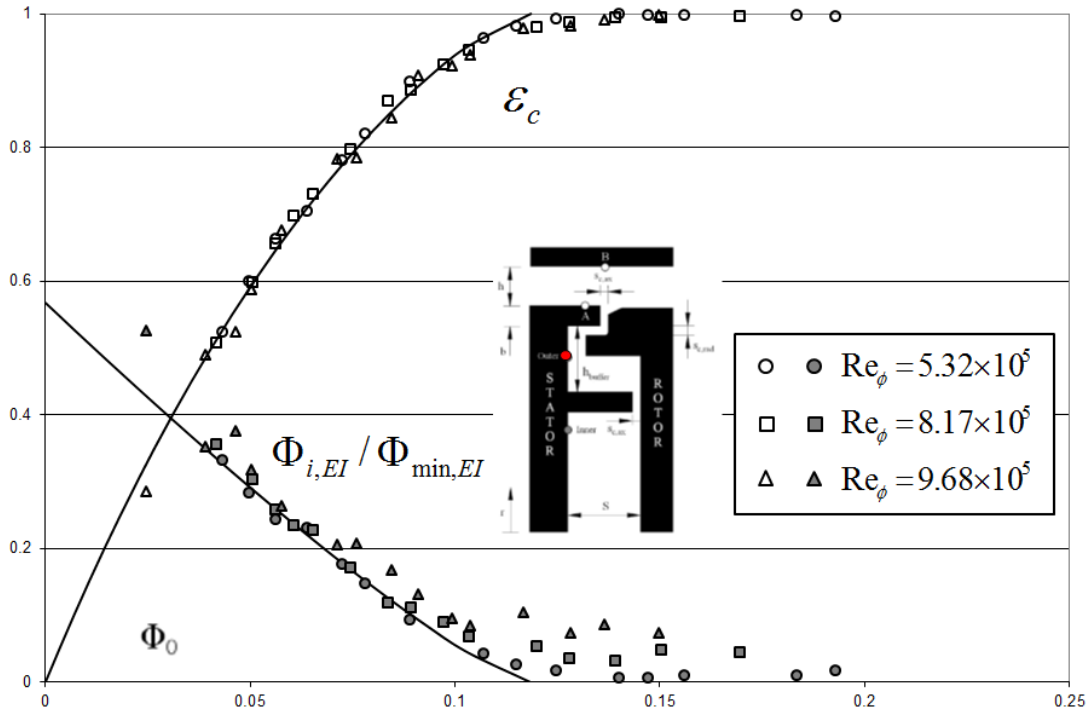

Figure 6-18 Experimental data for double radial-axial-clearance seal with EI ingress [60]

Re_ϕ	$C_{w,o}$	Φ_o	λ_T	Φ_i
8.17×10^5	2147	0.0418	0.04	0.0394
	3435	0.0669	0.064	0.0244
	4294	0.0836	0.08	0.015
5.32×10^5	1011	0.0303	0.028	0.0481
	1602	0.0479	0.042	0.0369
	2480	0.0742	0.065	0.02

Table 6-3 Computational parameters for the radial-axial-clearance seal

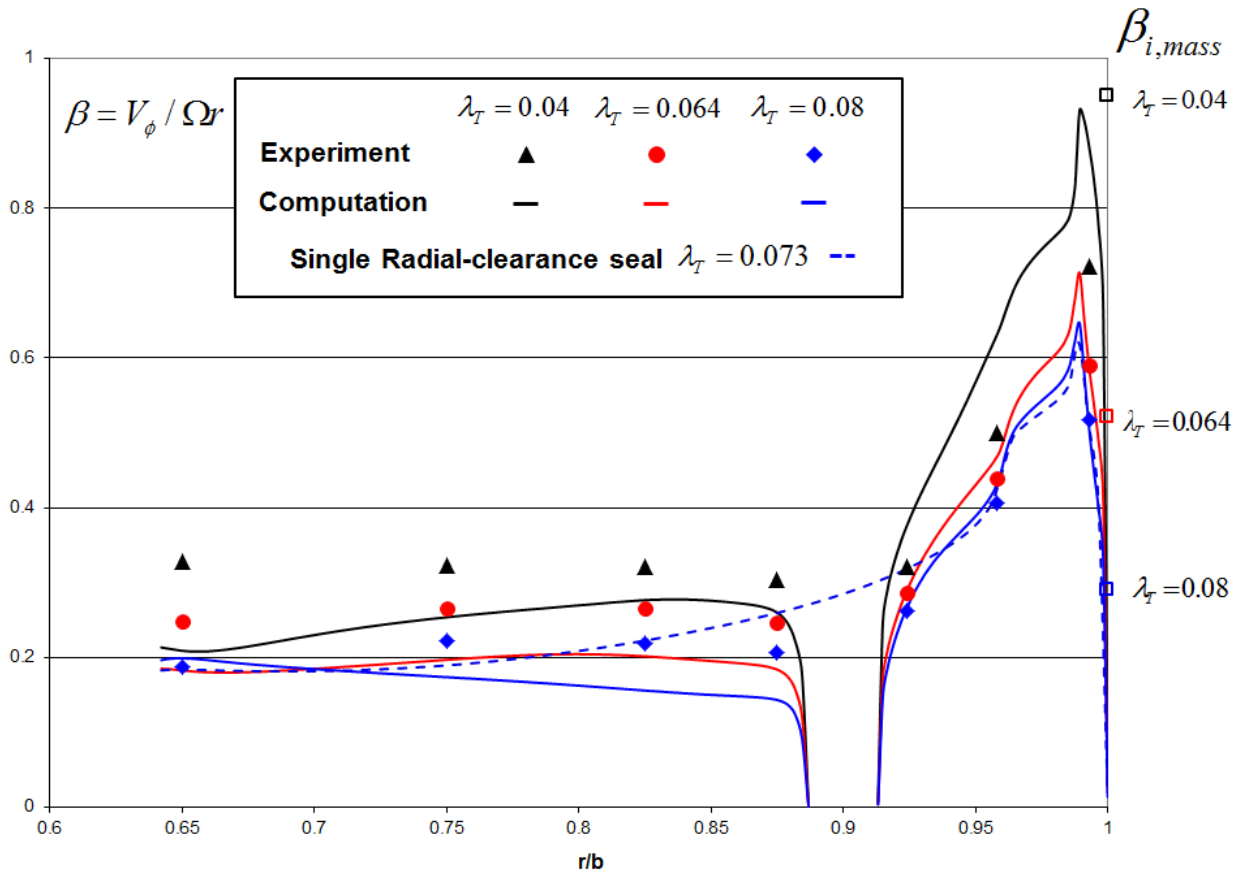

Figure 6-19 Swirl ratio distribution for the radial-axial-clearance seal, z/s =0.25 (symbols denote the experimental data [60])

Figure 6-19 shows the swirl ratio distribution at z/s =0.25 in wheel-space for the radial-axial-clearance seal. The closed symbols denote the experimental data [60] and the open square symbols at r/b =1 denote the mass-weighted average ingress swirl

ratio ($\beta_{i,mass}$) boundary condition. One computed result for the single radial-clearance seal at similar λ_T is also shown for comparison. In the inner wheel-space, the computations under-predict the swirl ratio. In the outer wheel-space, the computations mostly agree well with the measurements although there is over-prediction at the lowest value of λ_T. Similar to the comparison between double and single axial-clearance seals, there is little difference between the results for the radial-axial-clearance seal and the single radial-clearance seal, except in the region of the inner seal. In this region the radial-axial-clearance seal gives rise to a lower swirl ratio due to the additional sealing effect of the stationary inner seal insert.

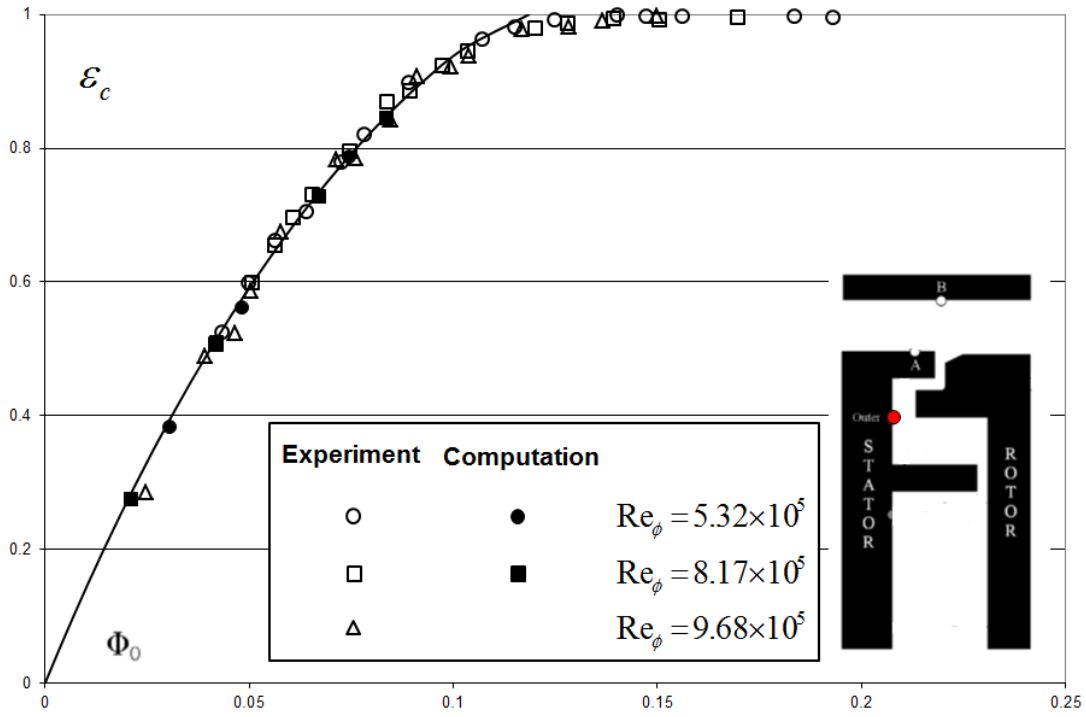

Figure 6-20 The computed variation of effectiveness with Φ_o for the radial-axial-clearance seal for outer sampling point (symbols denote the experimental data [60])

Figure 6-20 shows the computed and experimental variation of sealing effectiveness with Φ_o for the outer sampling points for radial-axial-clearance seal. The open symbols denote the experimental data [60], the closed symbols denote the computed effectiveness and the line is theoretical fit [60] for this seal geometry. The computations show very good agreement with the trend of the experimental results

and the theoretical fit. For the inner sampling point, the computations over-predict sealing effectiveness for the reasons discussed previously for other double-clearance seals. The results from inner sampling point for this seal geometry are therefore not shown here.

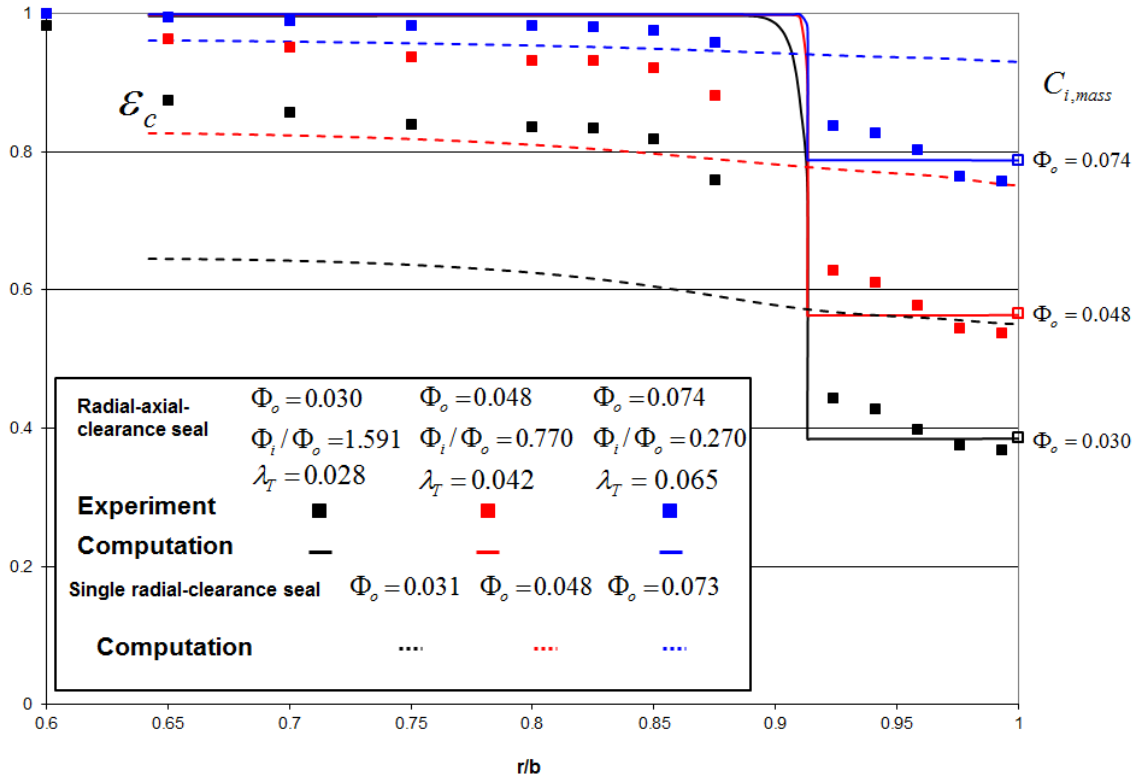

Figure 6-21 The radial distribution of effectiveness on stator for the radial-axial-clearance seal and the single radial-clearance seal (symbols denote the experimental data [60])

Figure 6-21 shows the radial distribution of sealing effectiveness on the stator for the radial-axial-clearance seal, and also the single radial-clearance seal for similar conditions. The experimental data for the radial-axial-clearance seal [60] are also shown. The open square symbols shown at $r/b=1$ denote the ingress concentration ($C_{i,mass}$) boundary condition calculated using the mass-weighted average assumption for the radial-axial-clearance seal. For the radial-axial-clearance seal, the computations again over-predict effectiveness in the inner wheel-space but are in reasonable agreement with the experimental data in the outer wheel-space. The measured sealing effectiveness decreases with increasing radius in the outer wheel-space, suggesting that the flow is not fully mixed in this region. Due to the

location of the outlet near the rotor in the prescribed ingestion model, mixing is inhibited and the computed effectiveness distribution is more flat. Compared with the single radial-clearance seal at similar conditions, there is a reduction in effectiveness in the outer wheel-space for the radial-axial-clearance seal. For this geometry, most of the ingested flow is contained in the outer wheel-space with the inner wheel-space being well-sealed.

6.4. **Sealing performance of all rim seal geometries**

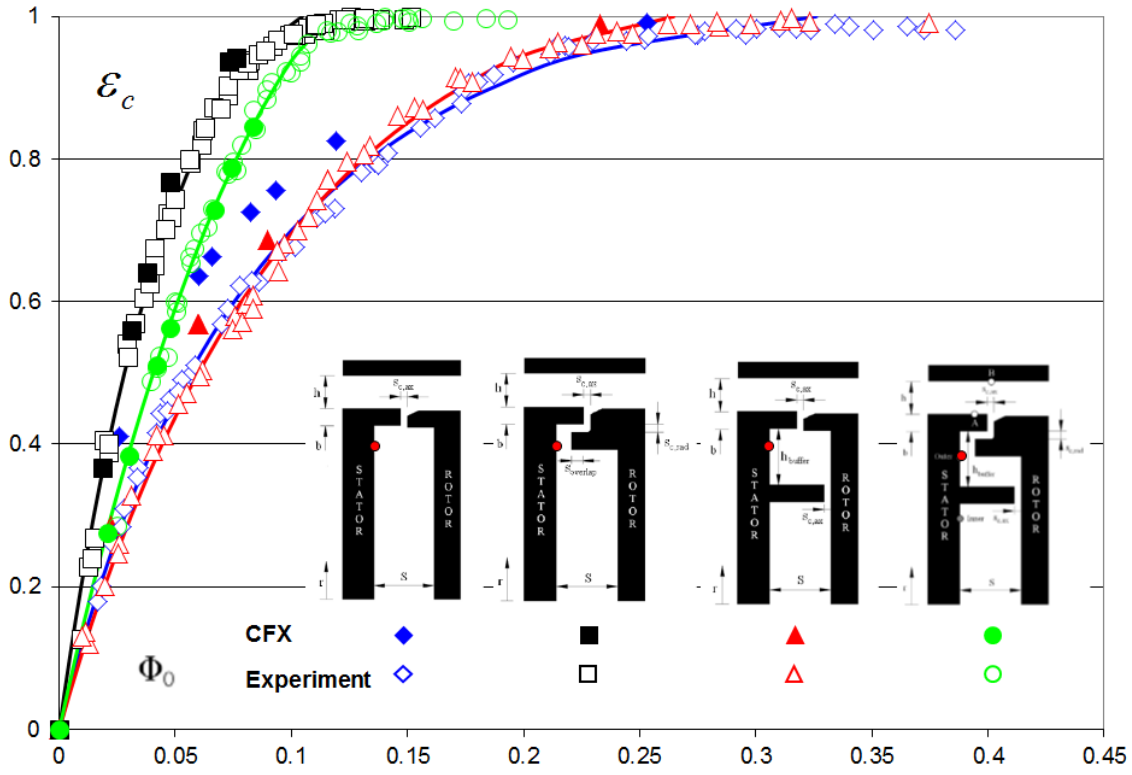

Figure 6-22 The computed variation of effectiveness with Φ_o for all rim seal geometries (The open symbols denote the experimental data [60], the closed symbols denote the computed effectiveness and the line is theoretical curves [60])

In the previous and current chapters, four rim seal geometries have been studied using prescribed ingestion models. In this section, the sealing performance of these geometries is compared. Figure 6-22 shows the computed and measured variation of sealing effectiveness with Φ_o for all of the rim seal geometries. For the two

double-clearance rim-seals, the sealing effectiveness at the outer sampling point is used for comparison. The computations for the single axial-clearance seal over-predict the effectiveness, whereas the other three geometries have reasonable agreement with the experimental data (and theoretical curve fits). Generally, the two radial-clearance seals show better sealing performance than the two axial-clearance seals at the same sealing flow rate. The single radial-clearance has better performance than the radial-axial-clearance seal, and the two axial-clearance seals have almost the same sealing performance. Although the computations over-predict sealing effectiveness in the inner wheel-space for the two double clearance seals, the improvement in effectiveness at low radius, due to the inner seal, is still distinct. In other words, the inner seal acts to protect the inner wheel-space.

6.5. **Chapter summary**

The axisymmetric model has limitation in terms of predicting ingress for double clearance rim seal. However the prescribed ingestion model with all seal geometries provides reasonable results for fluid dynamics and sealing effectiveness in comparison with the experimental results. Much less computing time is needed for the prescribed ingestion model compared with the 3D model. Hence, the model may be regarded as a simple, quick and convenient computational tool for the engine designer. When experimental information is not available, the distribution and effect on flow and heat transfer of ingestion in the wheel-space could be investigated by imposing hypothetical ingress conditions for a model involving any seal geometry.

7. Conclusions and future work

A new axisymmetric model for ingress research, the prescribed ingestion model, is presented in this thesis. This model includes only the wheel-space between the stator and the rotor and deduces the flow rate of ingestion from experimental data and theoretical curves [51, 54 and 60]. The model is a fast computational tool compared with more complex 3D models. The main conclusions will be summarized here and some possible future work also proposed.

7.1. The axisymmetric rotor-stator models

Before the prescribed ingestion model, two traditional axisymmetric rotor-stator models are studied for fluid dynamics and heat transfer in the wheel-space without ingress. Thereby, the axisymmetric model with ANSYS CFX was validated. The two axisymmetric rotor-stator models are the Bath Rig Model and Chen Rig Model respectively, as discussed in Chapter 4.

In terms of fluid dynamics, the differences between the Bath and Chen Rig Models influence the axial distribution of radial velocity at inlet to the wheel-space. Both geometries illustrate typical rotor-stator flow behaviour, with flow radially outward on the rotor, radially inward on the stator, and almost no radial flow in the middle of wheel-space. The magnitude of the outward radial velocity near the rotor increases and the inward radial velocity near the stator decreases with λ_T. The swirl ratio (non-dimensional circumferential velocity) in the core region between the rotor and stator is invariant with z but increases as radius increases. At a constant radius, the swirl reduces with increasing λ_T. This illustrates that the sealing flow can reduce the swirl ratio in the wheel-space. It is also shown that the thermal condition on the wall (rotor) has almost no influence on the velocity distribution in the wheel-space; even with the ideal gas law is used in these computations.

For heat transfer, the two geometries also have no distinct differences in terms of the distribution of Nusselt number, except near the inlet region. The computations indicate that $Nu\,\mathrm{Re}_\phi^{-0.8}$ increases as λ_T increases. Furthermore, the temperature distribution at the rotor surface slightly affects the value of $Nu\,\mathrm{Re}_\phi^{-0.8}$, but does not affect the distribution. The SST $k-\omega$ turbulence model provides more reasonable heat transfer results at high λ_T compared with the $k-\varepsilon$ model. However, the computations under-predict the Nusselt number at low λ_T, which is mainly due to the low levels of computed turbulence in the selected turbulence model and moderately fine meshes.

7.2. **The prescribed ingestion models**

The prescribed ingestion model, using four rim seal geometries, is presented in Chapters 5 and 6. The four geometries are the axial-clearance seal, radial-clearance seal, double axial-clearance seal and radial-axial-clearance seal respectively. At first, the mass-weighted average assumption was tested for the axial-clearance seal and it provided results which compared favourably with the experimental data [51, 60]. Three different layouts of ingress inlet and egress outlet were used. The best results were obtained with the ingress inlet positioned at the centre of shroud for all geometries. The outlet was positioned at rotor side of shroud for two the axial-clearance seals. For the radial ones, the outlet is at the rotor wall and the bottom of the axial overlap.

The computations for all rim seal geometries show that the ingested flow increases the swirl ratio in the wheel-space and the magnitude of increase is weakened as the sealing flow increases. At the same λ_T, the geometry only influences the distribution of swirl ratio at high radius (near rim seal region) and the fluid structure at low radius is dominated by λ_T. Due to the inserted inner seal, the double clearance seals have a lower swirl ratio than the single clearance seals near the inner seal region with same λ_T condition. The computed streamlines show the basic fluid structure in the

wheel-space with the sealing flow entering the boundary layer on the rotor at low radius; a part of ingested flow flows through the outlet directly and the remainder enters the stator boundary layer at the periphery of the wheel-space. A core of inviscid rotating fluid exists between the stator and rotor.

The variation of sealing effectiveness with Φ_o at r/b=0.958 and the radial distribution of sealing effectiveness on the stator are presented for all rim seal geometries. Presenting the variation of sealing effectiveness with Φ_o eliminates the effect of Re_ϕ. For all geometries, the sealing effectiveness increases as Φ_o increases, though the sealing performance of each seal is unlike. The two radial-clearance seals have a higher effectiveness, and consequently better sealing performance, than the two axial-clearance seals at the same Φ_o. The single radial-clearance has the best performance among all geometries at this radius. However, the double clearance seals provide an improvement in terms of effectiveness at low radius. The radial distributions on the stator show that if the fluid is fully mixed near the rim seal region, the effectiveness of the fluid in the boundary layer on the stator is almost invariant with radius. The small radial variation in the computations at high radius indicates that the flow is not fully mixed near rim seal region in the computations.

Heat transfer computations were only carried out for the axial-clearance seal. The values of $Nu\,\mathrm{Re}_\phi^{-0.8}$ are shown to be almost invariant with radius on rotor, except in the regions near the inlet and outlet. The Nusselt number increases as λ_T increases and as ingested flow decreases. The ingested flow increases the swirl ratio in the wheel-space and consequently reduces the Nusselt number. The computed Nu are in fair agreement with measurements, and these heat transfer experiments have not previously been studied computationally.

The prescribed ingestion model is potentially a useful tool to the engine designer. When experimental information is not available, the distribution and effect on flow and heat transfer of ingestion in the wheel-space could be investigated by imposing hypothetical ingress conditions for a model involving any seal geometry.

7.3. **Future work**

Although the prescribed ingestion model has provided reasonable results, it still has limitations and can be improved. Firstly, this prescribed ingestion model could combine with a theoretical study in order to determine more accurate boundary conditions for the ingested flow. As discussed above, the axisymmetric model blocks the ingested flow entering the inner wheel-space for double clearance seals. A separate prescribed ingestion models for the inner wheel-space might solve this problem. Furthermore, finer meshes could be applied for heat transfer computation in order to improve the results at low λ_T and heat transfer computations could be expanded to all rim seal geometries. The effect of radiation heat transfer can be considered for heat transfer computation in order to get better agreement with experimental data. The prescribed ingestion model could apply to engine geometries and engine conditions, and could be translated into a practical engine tool by engineers at Gas Turbine companies.

Work discussed in Chapters 4 and 5 were published (see Appendix). Further papers based on the prescribed ingestion model for other seal geometries (Chapter 6) are to be published.

References

1. Lock, G. D., 2007, Aircraft Propulsion - Lecture Notes, University of Bath.
2. Rolls-Royce, 1986, The Jet Engine, 5th edition, Rolls-Royce plc.
3. Meher-Homji, C. B. and Prisell, E., 2000, "Pioneering Turbojet Developments of Dr. Hans Von Ohain---From the HeS 1 to the HeS 011." J. Eng. Gas Turb. Power 122(2): pp. 191-201.
4. Cohen, H., Rogers, G. F. C., and Saravanamutto, H. I. H., 1996, Gas Turbine Theory, 4th edition, Longman.
5. Saravanamuttoo, H. I. H., Rodgers, G. F. C., Cohen, H. and Straznicky, P. V., 2009, Gas Turbine Theory, 7th edition, Pearson Prentice Hall, London.
6. Owen, J.M., 2009, “Prediction of Ingestion through Turbine Rim Seals Part 1: Rotationally-Induced Ingress”; Proceedings of ASME turbo Expo 2009: Power for Land, Sea and Air, June 8-12, 2009, Orlando, USA.
7. Owen, J.M., 2009, “Prediction of Ingestion through Turbine Rim Seals Part 2: Rxternally-Induced Ingress and Combined Ingress”; Proceedings of ASME turbo Expo 2009: Power for Land, Sea and Air, June 8-12, 2009, Orlando, USA.
8. Chen, J.-X., Gan, X. and Owen, J. M., 1996, “Heat Transfer in an Air-Cooled Rotor-Stator System”; ASME Journal of Turbomachinery, Vol. 118, pp. 444-451.
9. Batchelor, G. K., 1951, "Note on a Class of Solutions of the Navier-Stokes Equations Representing Steady Rotationally-Symmentric Flow." Quart. J. Mech Appl. Math. **4**: pp. 29-41.
10. Owen, J. M. and Rogers, R. H., 1989, Flow and Heat Transfer in Rotating-Disc Systems, Volume 1 - Rotor Stator Systems. Research Studies Press, UK; John Wiley, N.Y.
11. Daily, J. W. and Nece, R. E., 1960, "Chamber Dimension Effects on Induced Flow and Frictional Resistance of Enclosed Disks." ASME J. Basic Eng. **82**: pp. 217-232.
12. Wilson, M., Chen, J. X. and Owen, J. M., 1996, “Computation of Flow and Heat Transfer in Rotating−Disc Systems”, Computers in Reciprocating Engines and Gas Turbines, IMechE HQ, 9−10 January 1996, London, UK.
13. Da Soghe, R., Facchini, B., Innocenti, L. and Micio, M., 2011, “Analysis of Gas

Turbine Rotating Cavities: Estimation of Rotor Disk Pumped Mass Flow Rate", Proceedings of ASME Turbo Expo 2011, June 6-10, 2011, Vancouver, British Columbia, Canada.

14. Da Soghe, R., Innocenti, L., Micio, M., and Facchini, B., 2011. "Analysis of Gas Turbine Rotating Cavities by an One-dimensional Model: Definition of a New Discs Friction Coefficients Correlation Set". ASME Journal of Turbomachinery, April (2011), Volume 133, Issue 2, 021020.
15. Pelle, J. and Harmand, S., 2006, "Heat Transfer Measurements in an Opened Rotor–stator System Air-gap"; Experimental Thermal and Fluid Science 31 (2007) 165–180.
16. Pelle, J. and Harmand, S., 2009, "Heat Transfer Study in a Rotor–Stator System Air-gap with an Axial Inflow"; Applied Thermal Engineering Vol. 29 (2009) 1532–1543.
17. Lewis, P., Wilson, M., Lock, G. and Owen, J. M., 2007, "Physical Interpretation of Flow and Heat Transfer in Preswirl Systems"; ASME Journal of Engineering for Gas Turbines and Power, Vol. 129, pp. 769-777.
18. Poncet, S. and Schiestel, R., 2007, "Numerical Modeling of Heat Transfer and Fluid Flow in Rotor–Stator Cavities with Throughflow"; International Journal of Heat and Mass Transfer 50 1528–1544.
19. Javiya, U., Chew, J. Hills, N. Zhou, L., Wilson, M. and Lock, G., 2010, "CFD Analysis of Flow and Heat Transfer in a Direct Transfer Pre-Swirl System"; ASME Turbo Expo 2010: Power for Land, Sea and Air, June 14-18, 2010, Glasgow, UK.
20. Evans, J., Stevens, L. M., Bodily, C. and Kang, M. B., 2004, "Prediction of Velocities and Heat Transfer Coefficients in a Rotor-Stator Cavity"; ASME Turbo Expo 2004: Power for Land, Sea and Air, June 14-17, 2004, Vienna, Austria.
21. Bayley, F. J. and Owen, J. M., 1970, "The Fluid Dynamics of a Shrouded Disk System with a Radial Outflow of Coolant"; ASME J Eng Power, 92, pp. 335-341.
22. Phadke, U.P. and Owen, J.M., 1983, "An Investigation of Ingress for an 'Air Cooled' Shrouded Rotating Disk System with Radial Clearance Seals"; ASME J Eng Gas Turbines & Power, 105, pp 178-183.
23. Graber, D.J., Daniels, W.A. and Johnson, B.V., 1987, "Disk Pumping Test, Final Report"; Air Force Wright Aeronautical Laboratories, Report No. AFWAL-TR-87-2050.

24. Abe, T., Kikuchi, J. and Takeuchi, H., 1979, “An Investigation of Turbine Disk Cooling: Experimental Investigation and Observation of Hot Gas Flow into a Wheel Space”; 13th CIMAC Cong., Vienna, Paper No.GT30.
25. Phadke, U.P. and Owen, J.M., 1988, “Aerodynamic Aspects of the Sealing of Gas-Turbine Rotor-Stator Systems, Part 1: The Behaviour of Simple Shrouded Rotating-disc Systems in a Quiescent Environment”; Int J Heat Fluid Flow, 9, pp 106-112.
26. Phadke, U.P. and Owen, J.M., 1988, “Aerodynamic Aspects of the Sealing of Gas-Turbine Rotor-Stator Systems, Part 2: The Performance of Simple Seals in a Quasi-Axisymmetric External Flow”; Int J Heat Fluid Flow, 9, pp 106-112.
27. Phadke, U.P. and Owen, J. M., 1988, “Aerodynamic Aspects of the Sealing of Gas-Turbine Rotor-Stator Systems, Part 3: The Effect of Non-axisymmetric External Flow on Seal Performance”; Int J Heat Fluid Flow, 9, pp 106-112.
28. Hamabe, K., and Ishida, K., 1992, "Rim Seal Experiments and Analysis of a Rotor-Stator System with Nonaxisymmetric Main Flow"; ASME Paper 92-GT-160.
29. Chew, J. W., Green, T., and Turner, A. B., 1994, "Rim Sealing of Rotor-Stator Wheelspaces in the Presence of External Flow"; ASME Paper 94-GT-126.
30. Bohn, D. and Wolf, M., 2003, “Improved Formulation to Determine Minimum Sealing Flow $C_{w,\min}$ for Different Sealing Configuration”; ASME Paper GT2003- 38465.
31. Roy, R. P., Feng, J., Narzary, D., Saurabh, P. and Paolillo, R. E., 2004, “Experiments on Gas Ingestion through Axial-flow Turbine Rim Seals” ; ASME Turbo Expo 2004: Power for Land, Sea and Air, June 14-17, 2004, Vienna, Austria.
32. Roy, R. P., Zhou, D.W., Ganesan, S., Wang, C.Z., Paolillo, R. E. and Johnson, B.V., 2007, “The Flow Field and Main Gas Ingestion in a Rotor-Stator Cavity”; ASME Turbo Expo 2007: Power for Land, Sea and Air, May 14-17, 2007, Montreal, Canada.
33. Zhou, D. W., Roy, R. P., Wang, C.-Z. and Glahn, J. A., 2009, “Main Gas Ingestion in a Turbine Stage for Three Rim Cavity Configurations”; ASME Turbo Expo 2009: Power for Land, Sea and Air, June 8-12, 2009, Orlando, Florida, USA.
34. Dunn, D.M., Zhou, D.W., Saha, K., Squires, K.D., Roy, R.P., Kim Y.W. and Moon,

H.K., 2010, “Flow Field in a Single-Stage Model Air Turbine Rotor-Stator Cavity with Pre-Swirled Purge Flow”; ASME Turbo Expo 2010: Power for Land, Sea and Air, June 14-18, 2010, Glasgow, UK.

35. Gentilhomme, O., Hills, N. J., Turner, A. B. and Chew, J. W., 2002, “Measurement and Analysis of Ingestion through a Turbine Rim Seal”; ASME Turbo Expo 2002, June 3-6, 2002, Amsterdam, The Netherlands.
36. Lewis, P. and Wilson, M., 2007, “Three-Dimensional Computations of Ingress in Gas Turbine Cooling Systems”; Proceedings of the International Gas Turbine Congress 2007, December 3-7, 2007, Tokyo.
37. Mirzamoghadam, A.V., Heitland, G., Morris, M.C., Smoke, J., Malak, M. and Howe, J., 2008, “3D CFD Ingestion Evaluation of a High Pressure Turbine Rim Seal Disk Cavity”; Proceedings of ASME Turbo Expo 2008: Power for Land, Sea and Air, June 9-13, 2008, Berlin, Germany.
38. Mirzamoghadam, A.V., Heitland, G. and Hosseini, K. M., 2009, “The Effect of Annulus Performance Parameters on Rotor-Stator Cavity Sealing Flow”; ASME Turbo Expo 2009: Power for Land, Sea and Air, June 8-12, 2009, Orlando, Florida, USA.
39. Mirzamoghadam, A.V., and Xiao, Z. 2002, “Flow and Heat Transfer in an Industrial Rotor- Stator Rim Sealing Cavity”; Journal of Engineering for Gas Turbines and Power, Vol. 124, pp. 125-132.
40. Cao, C., Chew, J. W., Millington, P.R. and Hogg, S.I., 2003, “Interaction of Rim Seal and Annulus Flows in an Axial Flow Turbine”; ASME Turbo Expo 2003: Power for Land, Sea and Air, June 16–19, 2003, Atlanta, Georgia, USA.
41. Jakoby, R., Zierer, T., Lindblad, K., Larsson, J., Devito, L., Bohn, D. E., Funcke, J. and Decker, A., 2004, “Numerical Simulation of the Unsteady Flow Field in an Axial Gas Turbine Rim Seal Configuration”; ASME Turbo Expo 2004: Power for Land, Sea and Air, June 14-17, 2004, Vienna, Austria.
42. Rabs, M., Benra, F. –K., Dohmen, H. J., Lock, G. D. and Schneider, O., 2012, “Model Simplifications for Numerical Simulation of Ingestion through Gas Turbine Rim Seals”, 14th International Symposium on Transport Phenomena and Dynamics of Rotating Machinery, ISROMAC-14, February 27-March 2, 2012, Honolulu, HI, USA.
43. Wang, C.-Z., Johnson, B. V., Jong, F. D. and Vashist, T. K., 2007, “Comparison of Flow Characteristics in Axial-Gap Seals for Close- and Wide-Spaced Turbine

Stages”; ASME Turbo Expo 2007: Power for Land, Sea and Air, May 14-17, 2007, Montreal, Canada.

44. Laskowski, G. M., Bunker, R. S., Bailey, J.C., Ledezma, G., Kapetanovic, S., Itzel, G.M., Sullivan, M.A. and Farrell, T.R., 2009, “An Investigation of Turbine Wheelspcea Cooling Flow Interactions with a Transonic Hot Gas Path – Part 2: CFD Simulations”; ASME Turbo Expo 2009: Power for Land, Sea and Air, June 8-12, 2009, Orlando, Florida, USA.
45. Rabs, M., Benra, F.-K., Dohmen, H.J. and Schneider, O., 2009, “Investigation of Flow Instabilities near the Rim Cavity of a 1.5 Stage Gas Turbine”; ASME Turbo Expo 2009: Power for Land, Sea and Air, June 8-12, 2009, Orlando, Florida, USA.
46. O’Mahoney, T. S. D., Hills, N. J., Chew, J. W. and Scanlon, T., 2010, “Large-Eddy Simulation of Rim Seal Ingestion”; ASME Turbo Expo 2010: Power for Land, Sea and Air, June 14-18, 2010, Glasgow, UK.
47. Julien, S., Lefrancois, J., Dumas, G., Boutet-Blais, G., Lapointe, S., Caron, J. F. and Marini, R., 2010, “Simulations of Flow Ingestion and Related Structures in a Turbine Disk Cavity”; ASME Turbo Expo 2010: Power for Land, Sea and Air, June 14-18, 2010, Glasgow, UK.
48. Teuber, R., Li, Y. S., Maltson, J., Wilson, M., Lock, G. D. and Owen, J. M., 2012, “Computational Extrapolation of Turbine Sealing Effectiveness from Test Rig to Engine Conditions”, Proceedings of ASME Turbo Expo 2012, June 11-15, 2012, Copenhagen, Denmark.
49. Owen, J. M., Pountney, O. J., Zhou, K., Wilson, M. and Lock, G. D., 2010, “Prediction of Ingress Through Turbine Rim Seals. Part 1: Externally-Induced Ingress”, ASME Turbo Expo 2010: Power for Land, Sea, and Air, June 14-18, Glasgow, UK.
50. Owen, J. M., Pountney, O. J. and Lock, G. D., 2010, “Prediction of Ingress Through Turbine Rim Seals. Part 2: Combined Ingress”, ASME Turbo Expo 2010: Power for Land, Sea, and Air, June 14-18, Glasgow, UK.
51. Sangan, C. M., Pountney, O. J., Zhou, K., Wilson, M., Owen, J. M. and Lock, G. D., 2013, “Experimental Measurements of Ingestion through Turbine Rim Seals. Part 1: Externally-Induced Ingress”, ASME Journal of Turbomachinery. March (2013), Volume 135, Issue 2, 021038.
52. Sangan, C. M., Pountney, O. J., Zhou, K., Wilson, M., Owen, J. M. and Lock, G.

D. 2011. “Experimental Measurements of Ingestion through Turbine Rim Seals. Part 2: Rotationally-Induced Ingress”, ASME 2011 Turbo Expo: Turbine Technical Conference and Exposition, June 6–10, Vancouver, Canada.

53. Zhou, K., Wood, S. N. and Owen, J. M., 2011, “Analysis of Data for Ingestion through Turbine Rim Seals”, ASME 2011 Turbo Expo: Turbine Technical Conference and Exposition, June 6–10, Vancouver, Canada.
54. Sangan, C. M., Pountney, O. J., Scobie, J. A., Wilson, M., Owen, J. M. and Lock, G. D., 2012, “Experimental Measurements of Ingestion through Turbine Rim Seals. Part 3: Single and Double Seals”, Proceedings of ASME Turbo Expo 2012, June 11-15, 2012, Copenhagen, Denmark.
55. Pountney, O. J., Sangan, C. M., Lock, G. D. and Owen, J. M., 2012, “Effect of Ingestion on Temperature of Turbine Discs”, Proceedings of ASME Turbo Expo 2012, June 11-15, 2012, Copenhagen, Denmark.
56. Zhou, K., Wilson, M., Lock, G. D. and Owen, J. M., 2011, “Computation of Ingestion through Gas Turbine Rim Seals”, ASME 2011 Turbo Expo: Turbine Technical Conference and Exposition, June 6–10, Vancouver, Canada.
57. Wilcox, D.C., 1986, “Multiscale Model for Turbulent Flows”, AIAA 24th Aerospace Sciences Meeting, American Institute of Aeronautics and Astronautics, 1986.
58. Menter, F. R., 1993, "Zonal Two-Equation $k-\omega$ Turbulence Models for Aerodynamic Flows", AIAA Paper 93-2906.
59. Kader, B.A., 1981, “Temperature and Concentration Profiles in Fully Turbulent Boundary Layers”, International Journal of Heat and Mass Transfer, 24(9):1541-1544.
60. Sangan, C. M., 2011, “Measurement of Ingress through Gas Turbine Rim Seals”, University of Bath, PhD Thesis.
61. Pountney, O. J., 2012, “Heat Transfer in Turbomachinery”, University of Bath, PhD Thesis.

Appendix

International Journal of Gas Turbine, Propulsion and Power Systems

Computations of Flow and Heat Transfer in a Rotor-Stator System with Externally-Induced Ingestion